SEISMICITY, SEAWATER AND SEASONALITY:
NEW INSIGHTS INTO ICEBERG CALVING FROM YAHTSE GLACIER, ALASKA

By

Timothy Chester Bartholomaus

RECOMMENDED:

Dr. Shad O'Neel

Dr. Erin C. Pettit

Dr. Martin Truffer

Dr. Michael E. West

Dr. Christopher F. Larsen
Advisory Committee Chair

Dr. Paul J. McCarthy
Chair, Department of Geology and Geophysics

APPROVED:

Dr. Paul W. Layer
Dean, College of Natural Science and Mathematics

Dr. John C. Eichelberger
Dean of the Graduate School

Date

SEISMICITY, SEAWATER AND SEASONALITY:
NEW INSIGHTS INTO ICEBERG CALVING FROM YAHTSE GLACIER, ALASKA

A

DISSERTATION

Presented to the Faculty

of the University of Alaska Fairbanks

in Partial Fulfillment of the Requirements

for the Degree of

DOCTOR OF PHILOSOPHY

By

Timothy Chester Bartholomaus, A.B., M.Sc.

Fairbanks, Alaska

December 2013

Abstract

At many of the largest glaciers and ice sheets on Earth, more than half of the annual ice loss occurs through iceberg calving into the ocean. Calving is also responsible for the most rapid ice mass changes, both directly (through the mechanical loss of ice at the terminus) and indirectly (through dynamic thinning of upstream ice initiated by terminus retreat). Yet, the mechanisms and factors that control calving are poorly understood. Recordings of glaciogenic seismic waves, known as "icequakes," produced during iceberg calving offer opportunities for insight that cannot be gleaned through other methods.

In order to better understand iceberg calving and its links to calving icequakes, we conducted a 2-yr study of rapidly advancing Yahtse Glacier, site of one of the densest clusters of calving icequakes in southern Alaska. By synchronizing video of iceberg calving events with locally-recorded seismograms, we found that most icequake energy is produced after subaerial iceberg detachment from the glacier terminus, while the iceberg impacts and descends below the sea surface. Cavitation beneath the water surface generates the largest amplitude portions of icequakes–those that are detectable over several hundred km distances. Numerical simulations of these iceberg-sea surface interactions predict sources with durations that are consistent with the 1-5 Hz frequency content of calving icequakes.

Oceanographic measurements in Icy Bay, where Yahtse Glacier terminates, reveal that warm water may melt most of the ice reaching the submarine terminus. During the summer, water with temperature > 10 °C flows from the Gulf of Alaska coast to within 2 km of Yahtse Glacier's terminus. We find that heat transport between 5 and 40×10^9 W can readily melt the submarine glacier terminus at a rate that matches the speed with which ice flows towards the glacier terminus (17 m d^{-1}). Subaerial iceberg calving rates may be paced by submarine melt rates.

To place our calving and submarine melt observations in a broader temporal context, we construct an empirical model of iceberg size using icequake properties and tune the model with over 800 visually-observed iceberg calving events. We find that iceberg calving is at its minimum during the winter, when seawater is cool and mixing of proglacial seawater by subglacial discharge is weak. Overlaying this long period cycle, we find significant daily to inter-annual variability and sensitivity of calving to tidal stage. These observations expand our appreciation for the ocean's important role in iceberg calving: at time scales ranging from the sub-second generation of icequakes, to the annual undercutting of the glacier terminus.

Table of Contents

Page

Page

List of Figures

Page

List of Tables

List of Supplementary Files

List of Appendices

Acknowledgements

Many people have enriched my time at the University of Alaska Fairbanks (UAF) and contributed to my scientific development. To all of you: thank you. Thank you. Thank you.

It has been my pleasure to work with my advisor, Chris Larsen, during these last four and a half years. I thank Chris for enabling most of my achievements during my Ph.D. He has helped me understand both the intricate mechanisms and broader patterns at work in Alaska's glaciers. Chris encouraged me to keep my analyses rooted in our data and observations. He helped me to work efficiently and learn as much as I could about tidewater glaciers during these years. He brought me to see the glaciers of Southeast Alaska, supported conference travel, and encouraged me to teach within the Department of Geology and Geophysics. Throughout our relationship, he has been unfailingly kind, exemplified by his inviting Sophie and I for dinner while our frozen, unresponsive car warmed in his heated garage, and flying down to McCarthy to be a part of Sophie's and my Alaskan commitment celebration. Thank you, Chris.

I also thank Mike West and Shad O'Neel for the tremendous impacts they have had on my work at UAF and on the Yahtse Glacier Project. Shad's expertise in calving seismicity was exceptionally valuable and much of the work within this dissertation directly builds on his. His suggestion to record video of the terminus and maintain an observer record of iceberg calving events provided the foundation of the 2nd and 4th chapters of this dissertation. His enthusiasm for our work was clear in our conversations and in his prompt edits to drafts. I also thank Shad for opening the door to fruitful collaborations, and to Ethan Welty, Tad Pfeffer and Jan Åström for including me in their publications.

Mike West welcomed me into his research group as soon as I arrived at the Geophysical Institute, and gave me a second home within the Seismology Lab. I've been glad to be a part of Tea and TTODAYs since my start here. He generously taught me how to work with and think about seismic waveforms, guided my development as a seismologist, and supported and assisted with my mentoring of a visiting undergraduate researcher, Ayla Heinze Fry. (Thanks to Ayla for her hard work and for helping me grow as a teacher.) Mike helped me keep the bigger picture of our work in mind, and encouraged me to not get too mired in minutiae. I profoundly enjoyed my time in glorious Icy Bay, working with and learning from Chris, Mike and Shad.

My committee members Martin Truffer and Erin Pettit always took the time to discuss my research with me and treated me as a colleague. I've valued Erin's respect ever since our initial meeting at my first glaciology conference, Northwest Glaciologists, in 2004. Thanks to Martin for his understated leadership within the UAF glaciology group. Roman Motyka was as generous and committed to my professional growth as any committee member. He donated his time, resources, and equipment during oceanography fieldwork in Icy Bay. The next year, he invited me to join his fieldwork in LeConte Bay and loaned me another of his instruments, even after the first was lost to drifting Yahtse Glacier icebergs. Much of my oceanography work (3rd chapter) follows in his footsteps.

A number of other people have made important contributions to the success of our Icy Bay field work. Tony Oney and Paul Claus piloted us expertly through the spectacular St. Elias Range. Their enthusiasm, dedication and professionalism contributed immeasurably to the success of our work. I am grateful to Michelle Kissling (U.S. Fish and Wildlife Service), who entrusted me with her skiff in Icy Bay. With her generosity, I achieved far more than I would have been able to without her help. Barbara Trüssel, Megan O'Sadnick, Joel Brann, Paul Aguilar (Univ. of Wash.), Eric Boget (Univ. of Wash.), Evan Burgess and Sophie Gilbert all enthusiastically and ably assisted with field work. It was great fun being out with all of them.

I thank Regine Hock for her confidence in me, for her persistent encouragement as I worked to publish the last of my master's thesis shortly after arriving at UAF, and for her role as a community-minded dynamo within our group. And for asking, "But what has glacier seismology shown us that we didn't already know?" I've valued conversations, glaciological, seismological, and otherwise, with Anthony Arendt, Will Harrison, Mark Fahnestock, Andy Aschwanden, Glenn Thompson, Doug Christensen, and Silvio DeAngelis.

The Geophysical Institute (GI) is an outstanding place to be a graduate student, and the expertise of its researchers has allowed me to accomplish far more, far faster and with far more enjoyment than I otherwise might have. A major part of this research community are the GI's students. I have learned a great deal from and enjoyed spending time in the office and the field with Joanna Young, Bob McNabb, Marijke Habermann, Barbara Trüssel, Dave Podrasky, Joe Kennedy, Jason Amundson, Christian Keinholtz, Lee Peterson, Jenny Davis, Cody Beedlow, Christina Carr, Summer Miller, Ronni Grapenthin, Julie Elliott, Helena Buurman, Chris Bruton, Laura Keyson, and Taryn Lopez.

Thanks to Taryn Lopez for working with me during the first year of the GI Graduate Student Association, and to all the GIGSA members for their ongoing contributions to our organization. Their volunteerism makes the GI a stronger community and an even better place to work and study as a graduate student. Thanks also to my fellow 2011-2013 members of the Graduate Academic and Advisory Committee of the UAF Faculty Senate for welcoming my participation. I valued the opportunity to teach my first college class, made possible by Sarah Fowell.

This dissertation was supported by the National Science Foundation, through grant EAR-0810313 to Chris Larsen and Mike West, and through a student research grant to myself from the UAF Center for Global Change with funds from the Cooperative Institute for Alaska Research.

My parents, Kathy and Gary Bartholomaus, have cheered ceaselessly for me throughout my life. I am profoundly lucky to have their love and support. All that I have been able to achieve in my life is because they so firmly set me on a fruitful path.

During my time in Fairbanks and during the years ahead of us, I cannot imagine a companion I am better suited for than my wife, Sophie Gilbert. I thank her for her love, her energy, her curiosity, and her support throughout my work on this dissertation. Beyond the love she has supported me with, Sophie's creativity and intelligence shine in the pages of this dissertation through the ideas I pursued, the figures, the editing and even the statistical techniques. Fairbanks and Alaska have been wonderful for us and I am very much looking forward to our next adventures together.

Chapter 1
Introduction

1.1 On the beach

Brilliant, violet spikes of lupine flowers carpeted the fine sand around us. Beyond the lupines, alders trembled in the steady, katabatic wind flowing off the terminus of nearby Yahtse Glacier. Yahtse Glacier (60.2° N, 141.4° W) is a 1000 km^2 tidewater glacier and Icy Bay, in which it terminates, was packed with meter-size bits of gleaming ice, shining beneath the pure blue sky. The fjord surface heaved and hissed before us as waves washed onto shore, grinding the dense pack of small icebergs and tossing them onto the beach. The wave was the product of the last major iceberg calving event at the glacier's terminus, just one minute prior. My friend and I sat side by side in matching nylon camp chairs, scrutinizing the craggy face of the glacier. In my left hand I held a wrist watch; in my right, a pencil. A notebook lay open on my lap.

"Oh! There it goes! It's starting!" As my friend exclaimed, truck-size blocks began to topple from the shear ice cliff we had referred to as "the Citadel." A kilometer and a half distant, the blocks fell as though in slow motion, taking several seconds before they impacted the icy fjord. Moments later, the entire glacier prow gave way and began to collapse. I jotted the time in my notebook as the deep, thunderous rumble reached us, then we both watched rapt as a mass of ice that dwarfed the 7-story UAF Geophysical Institute's Elvey Building crumbled into the icy ocean. In my field notes, this is a "size 4" calving event.

We were there to study iceberg calving at Yahtse Glacier, and we were not disappointed. Little by little, the glacier presses out into the ocean, driven by its tremendous mass of accumulated ice. Yet every minute, every hour, and every day, it calves back, creating a dynamic equilibrium at the terminus. While this give and take at the terminus is typical for tidewater glaciers, Yahtse Glacier calves far more frequently than most. Even amongst its neighbors in the staggeringly icy St. Elias range, Yahtse is a regional hot-spot for iceberg calving (*O'Neel et al.*, 2010). My friend and I were part of a team trying to find out why.

Interest in Yahtse's high calving rate began in 2010, when Shad O'Neel and others demonstrated that iceberg calving was the true source of many of the "earthquakes" recorded in Alaska, a pattern that had long been recognized by analysts at the Alaska Earthquake Information Center (AEIC) (*O'Neel et al.*, 2010). Seismic events with signa-

tures quite different than those of southern Alaska's typical, tectonic earthquakes were frequently triggering the automatic detection programs operated by the AEIC. These events, long-tagged by the AEIC as "glacial," had their origins near the termini of Alaska's tidewater glaciers, on the Gulf of Alaska, but were detected hundreds of kilometers from the coast. O'Neel and his coauthors delved into this rich data set, and found that when they looked across the entirety of the St. Elias Range, the majority of these "icequakes" were produced by iceberg calving at the terminus of Yahtse Glacier. They cited previous work that had conjectured how one *part* of the iceberg calving process could produce these powerful icequakes (*O'Neel and Pfeffer*, 2007), but other source mechanisms could not be ruled out. Furthermore, why so many icequakes originated at Yahtse Glacier remained a mystery.

Back on the beach, we were recording the data that would prove crucial to understanding Yahtse's calving productivity. Over 12 days, on average 7 hrs per day, we noted the time, size, location, duration and different styles of each calving event that we witnessed. These notes, combined with simultaneous video and seismic recordings, would enable us to dissect differences between the diverse avalanching, dropping and toppling calving events, and identify exactly which parts of the calving process were generating the regionally-detected icequakes. But it turns out that the dramatic calving events at Yahtse's terminus were only part of the story. We would later learn that another, less obvious process going on below the ocean's surface was removing at least as much ice as calving. Warm ocean water in the fjord quietly melts the terminus from below.

1.2 Motivation

This dissertation is motivated by the importance of mass loss from glacier termini in dictating rates of glacier mass change and contributions to sea level rise, as well as by the ubiquity of calving icequakes. The world's largest glaciers end in the ocean, and in many cases, changes in their mass balance appear to be driven by changes in the rate of mass loss from the glacier front, a term sometimes referred to as frontal ablation (*Rignot*, 2008; *Nick et al.*, 2009). Alaska's glaciers are no exception to this rule. One of the most staggering mass losses in history occurred at Glacier Bay during the 19th and 20th centuries because the glaciers there end in the ocean (*Larsen et al.*, 2005) . Presently, Columbia Glacier, in the Chugach Mountains, is the poster-child for tidewater glacier change. It has retreated 20 km in 30 years, in some places, a vertical kilometer of ice has been lost in the same time

period (*McNabb et al.*, 2012). Perhaps the worst fear of glaciologists (and coastal managers worldwide) is that the enormous marine-terminating glaciers in Greenland or Antarctica will execute a Glacier Bay or Columbia Glacier-style retreat. Some fear that such retreats might already be under way, for example at Pine Island Glacier in Antarctica (*Rignot*, 2008; *Stanton et al.*, 2013). Uncertainty associated with the rates at which tidewater glaciers can melt and calve into the ocean remains one of the biggest questions for scientists attempting to predict rates of sea level rise.

The ubiquity of calving icequakes has inspired an emerging approach for studying the processes and rates of iceberg calving. Everywhere that glaciologists and seismologists have deployed seismometers at or near the termini of calving glaciers, the unique icequake signatures of ice falling into the ocean have been found (e.g., *Wolf and Davies*, 1986; *Qamar*, 1988; *O'Neel et al.*, 2010; *Walter et al.*, 2012). Glacier seismology also allows for the precise timing of calving events to be identified, even for relatively small icebergs. Knowledge of the timing of iceberg calving at daily, or even sub-daily, resolution enables researchers to more accurately gauge the sensitivity of glaciers to environmental forcings and identify the key processes determining the rate at which glaciers calve. Non-seismic methods, such as satellite remote sensing, lack this temporal resolution, and are often blind to the smaller calving events that can collectively make up a significant portion of the iceberg calving flux.

1.3 Approach

In order to build our understanding of iceberg calving, I have participated in a large-scale research project at Yahtse Glacier, based from the University of Alaska Fairbanks' Geophysical Institute. This project collected field data from June 2009 to September 2011, and was led by Chris Larsen, Mike West and Shad O'Neel with major funding from the National Science Foundation and the U.S. Geological Survey. In addition to producing disproportionate numbers of icequakes, Yahtse Glacier is advancing, increasing its length by over 2 km since its most retracted position in the early 1990s. While approximately 10 (out of 50) Alaskan tidewater glaciers are presently advancing, Yahtse Glacier's sustained advance rate of 100 m a^{-1} is significantly faster than the next fastest advance ($\sim$ 20 m a^{-1} at Hubbard Glacier) (*McNabb*, 2013). The terminus is relatively thin. At the terminus, the ice stands approximately 60 m above sea level and the fjord is no deeper than 110 m. Thus,

the glacier is sufficiently thick, relative to the fjord depth, to prevent it from floating at the terminus.

More broadly, the behavior of tidewater glaciers span a wide spectrum within which Yahtse Glacier is fairly extreme (Fig.1.1). Calving style, submarine melt and oceanographic conditions, and glacier dynamics all can vary among tidewater glaciers. In Fig. 1.1, we place the behavior of Yahtse Glacier into context by qualitatively comparing it on each of these fronts with Jakobshavn Isbræ in Greenland (*Amundson et al.*, 2010; *Podrasky et al.*, 2012), and in Alaska, with Columbia Glacier during the late 2000's (mid retreat: *O'Neel et al.*, 2005; *Walter et al.*, 2010) and with Hubbard Glacier (*Trabant et al.*, 2003; *Ritchie et al.*, 2008). In light of these contrasts, each chapter of this dissertation contains discussion of how our findings are generalizable to other tidewater glaciers, and how they may be unique to circumstances such as those found at Yahtse Glacier.

To study the behavior of Yahtse Glacier, my collaborators and I established 10 seismic stations around the margin of the lower glacier. We located an additional 10 seismometers on the glacier surface, 8 GPS receivers on the glacier surface, 3 timelapse cameras focused on the glacier terminus and adjacent fjord, and a weather station adjacent to the terminus. Further data collection included oceanographic surveys within Icy Bay during three consecutive Julys, approximately weeklong ground-based surveys of the ice flow speed near the terminus during two different summers, video of calving events, and the observer record of iceberg calving. This dissertation draws most heavily on the ice-marginal seismic stations, particularly those near the terminus, on the oceanographic data, and on the video and observer record; however, our interpretations and hypotheses rely on the full suite of data collected.

The topics discussed in this dissertation address a number of specific questions pertaining to calving and submarine melt of the glacier terminus. These include:

- What part or parts of the iceberg calving process (e.g., vibrating serac blocks, ice fracturing, iceberg impact on the water) generate the iceberg calving signals detected over 100s of km from the glacier front?
- What information about a particular calving event is contained within the icequake signal it produces?
  - Can we predict the mass or volume of an iceberg by examining its icequakes?
- What role does the ocean play in iceberg calving?

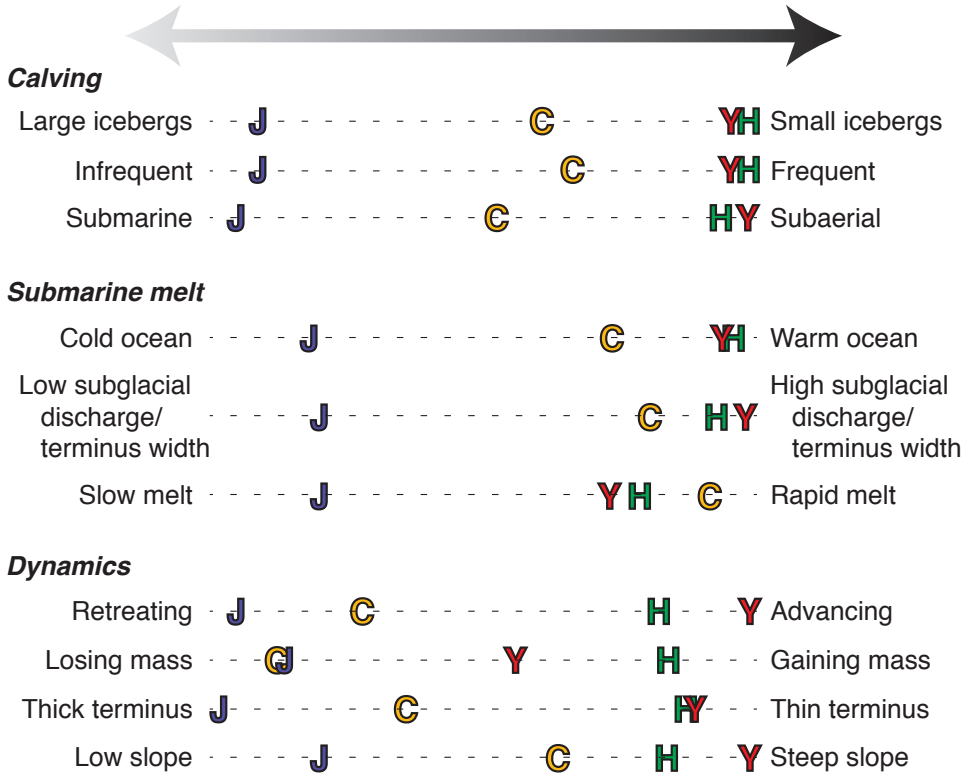

Figure 1.1. Spectrum of tidewater glaciers, qualitatively compared according to calving, submarine melt, and glacier dynamics. 'J' represents Jakobshavn Isbræ in Greenland, in Alaska, 'C' represents Columbia Glacier during the late 2000's, 'H' represents Hubbard Glacier, and 'Y' represents Yahtse Glacier. Many of these quantities are poorly known; for some instances, the location of each glacier within the spectrum is subject to interpretation.

- How much of the ice that reaches the terminus melts vs. breaks off and floats away as icebergs?
- To what extent is water from the Gulf of Alaska exchanged with the water at the distal, glacierized heads of fjords?
- Do tidal variations in sea level affect rates of iceberg calving?

I address these questions in three complementary chapters, each published or soon to be published as independent, peer-reviewed manuscripts. For each of these journal articles, I formulated and conducted the analyses, created the figures, and wrote the text with editorial guidance from co-authors. Throughout this dissertation, I have sought to generalize our findings to other glaciers and regions while acknowledging the characteristics that make Yahtse Glacier unusual (e.g., rate of calving occurrence, thin and advancing terminus).

In Chapter 2, published in the *Journal of Geophysical Research: Earth Surface*, my co-authors and I study the generation of calving icequakes by taking advantage of our ability to *see* the seismic source, an extremely rare occurrence among almost all other seismic studies. We combine seismic data recorded adjacent to the glacier terminus with high-resolution, accurately-timed video and the observer record of calving to find which parts of the calving process are the most powerfully seismogenic. As with the calving icequakes of other glaciers, the frequencies of icequake waveforms at Yahtse Glacier are quite narrowband, with peak power between 1 and 5 Hz. We model the force budget on a falling, impacting iceberg to identify whether our proposed mechanisms are responsible for the observed peak frequencies, and conclude that indeed they are.

We use measurements of water properties within Icy Bay to "un-mix" the quantities of glacier meltwater, subglacial discharge, and ambient seawater near the terminus of Yahtse Glacier in Chapter 3, published in *Earth and Planetary Science Letters*. Using estimates of the current in the near-surface water layers, we calculate plausible bounds on the rate of submarine ice melt. Regional mooring data and calculations of freshwater delivery to the Gulf of Alaska allow us to place these summer-time calculations within a broader annual and inter-annual context.

In Chapter 4, we develop and validate an approach to automatically detect calving icequakes in 18 months of seismic data recorded by our local seismic network. From these icequakes, we derive a number of quantitative icequake properties and use them, with the

observer record, to develop a statistical model for predicting iceberg sizes from seismic variables. We then use this modeled relationship to derive a time series of calving fluxes at Yahtse Glacier and interpret it in light of the conclusions drawn from Chapters 2 and 3.

Finally, in Chapter 5, we summarize some of the more significant findings regarding iceberg calving, the generation of icequakes, and the importance of submarine glacier melt. We suggest a number of future directions for research into iceberg calving and calving seismicity.

References

Amundson, J. M., M. Fahnestock, M. Truffer, J. Brown, M. P. Lüthi, and R. J. Motyka (2010), Ice mélange dynamics and implications for terminus stability, Jakobshavn Isbræ, Greenland, *J. Geophys. Res.*, *115*(F1), 1–12, doi: 10.1029/2009JF001405.

Larsen, C. F., R. J. Motyka, J. T. Freymueller, K. A. Echelmeyer, and E. R. Ivins (2005), Rapid viscoelastic uplift in southeast Alaska caused by post-Little Ice Age glacial retreat, *Earth Planet. Sci. Lett.*, *237*(3-4), 548–560, doi: 10.1016/j.epsl.2005.06.032.

McNabb, R. (2013), On the frontal ablation of Alaska tidewater glaciers, Ph.D. Dissertation, University of Alaska Fairbanks.

McNabb, R., et al. (2012), Using surface velocities to calculate ice thickness and bed topography: a case study at Columbia Glacier, Alaska, USA, *J. Glaciol.*, *58*(212), 1151–1164, doi: 10.3189/2012JoG11J249.

Nick, F. M., A. Vieli, I. M. Howat, and I. Joughin (2009), Large-scale changes in Greenland outlet glacier dynamics triggered at the terminus, *Nat. Geosci.*, *2*(2), 110–114, doi: 10.1038/NGEO394.

O'Neel, S., and W. T. Pfeffer (2007), Source mechanics for monochromatic icequakes produced during iceberg calving at Columbia Glacier, AK, *Geophys. Res. Lett.*, *34*(22), 1–5, doi: 10.1029/2007GL031370.

O'Neel, S., W. T. Pfeffer, R. Krimmel, and M. Meier (2005), Evolving force balance at Columbia Glacier, Alaska, during its rapid retreat, *Journal of Geophysical Research*, *110*(F3), 1–18, doi: 10.1029/2005JF000292.

O'Neel, S., C. F. Larsen, N. Rupert, and R. Hansen (2010), Iceberg calving as a primary source of regional-scale glacier-generated seismicity in the St. Elias Mountains, Alaska, *J. Geophys. Res.*, *115*(F4), 1–12, doi: 10.1029/2009JF001598.

Podrasky, D., M. Truffer, M. Fahnestock, J. Amundson, R. Cassotto, and I. Joughin (2012), Outlet glacier response to forcing over hourly to interannual timescales, Jakobshavn Isbræ, Greenland, *Journal of Glaciology*, *58*(212), 1212–1226, doi: 10.3189/2012JoG12J065.

Qamar, A. (1988), Calving icebergs: a source of low-frequency seismic signals from Columbia Glacier, Alaska, *J. Geophys. Res.*, *93*(B6), 6615–6623.

Rignot, E. (2008), Changes in West Antarctic ice stream dynamics observed with ALOS PALSAR data, *Geophys. Res. Lett.*, *35*(January), 1–5, doi: 10.1029/2008GL033365.

Ritchie, J. B., C. S. Lingle, R. J. Motyka, and M. Truffer (2008), Seasonal fluctuations in the advance of a tidewater glacier and potential causes: Hubbard Glacier, Alaska, USA, *J. Glaciol.*, *54*(186), 401–411.

Stanton, T., W. Shaw, M. Truffer, H. Corr, L.E.Peters, K. Riverman, R. Bindschadler, D. Holland, and S. Anandakrishnan (2013), Channelized ice melting in the ocean boundary layer beneath Pine Island Glacier, Antarctica, *Science*, *341*, 1236–1239.

Trabant, D. C., R. M. Krimmel, K. a. Echelmeyer, S. L. Zirnheld, and D. H. Elsberg (2003), The slow advance of a calving glacier: Hubbard Glacier, Alaska, U.S.A., *Annals of Glaciology*, *36*(1), 45–50, doi: 10.3189/172756403781816400.

Walter, F., S. O'Neel, D. McNamara, W. T. Pfeffer, J. Bassis, and H. Fricker (2010), Iceberg calving during transition from grounded to floating ice: Columbia Glacier, Alaska, *Geophys. Res. Lett.*, *37*(15), 1–5, doi: 10.1029/2010GL043201.

Walter, F., J. M. Amundson, S. O'Neel, M. Truffer, M. Fahnestock, and H. a. Fricker (2012), Analysis of low-frequency seismic signals generated during a multiple-iceberg calving event at Jakobshavn Isbræ, Greenland, *J. Geophys. Res.*, *117*(F1), 1–11, doi: 10.1029/2011JF002132.

Wolf, L. W., and J. N. Davies (1986), Glacier-generated earthquakes from Prince William Sound, Alaska, *Bull. Seismol. Soc. Am.*, *76*(2), 367–379.

Chapter 2

Calving seismicity from iceberg–sea surface interactions[1]

2.1 Abstract

Iceberg calving is known to release substantial seismic energy, but little is known about the specific mechanisms that produce calving icequakes. At Yahtse Glacier, a tidewater glacier on the Gulf of Alaska, we draw upon a local network of seismometers and focus on 80 hours of concurrent, direct observation of the terminus to show that calving is the dominant source of seismicity. To elucidate seismogenic mechanisms, we synchronized video and seismograms to reveal that the majority of seismic energy is produced during iceberg interactions with the sea surface. Icequake peak amplitudes coincide with the emergence of high velocity jets of water and ice from the fjord after the complete submergence of falling icebergs below sea level. These icequakes have dominant frequencies between 1 and 3 Hz. Detachment of an iceberg from the terminus produces comparatively weak seismic waves at frequencies between 5 and 20 Hz. Our observations allow us to suggest that the most powerful sources of calving icequakes at Yahtse Glacier include iceberg-sea surface impact, deceleration under the influence of drag and buoyancy, and cavitation. Numerical simulations of seismogenesis during iceberg-sea surface interactions support our observational evidence. Our new understanding of iceberg-sea surface interactions allows us to reattribute the sources of calving seismicity identified in earlier studies and offer guidance for the future use of seismology in monitoring iceberg calving.

2.2 Introduction

Iceberg calving may take many forms, ranging from the slow rifting of tabular icebergs with decadal recurrence times (e.g. *Bassis et al.*, 2005), to the failure of relatively intact, kilometer-scale, full-glacier-thickness icebergs with week to month recurrence times (e.g. *Amundson et al.*, 2008; *Joughin et al.*, 2008), to the crumbling release of smaller seracs with minute to hour recurrence times (e.g. *O'Neel et al.*, 2003). Individual calving events often include elements of each of these. For example, *Walter et al.* (2012) describe a sequence of calving events in which two full-glacier-thickness icebergs rotate out from the terminus accompanied by innumerable smaller serac failures over a period of 12 minutes.

[1]Published as Bartholomaus, T. C., C. F. Larsen, S. O'Neel, and M. E. West (2012), Calving seismicity from iceberg-sea surface interactions, *J. Geophys. Res.*, *117*(F4), 1–16, doi: 10.1029/2012JF002513

Across this continuum of events at glacier termini, iceberg calving is a source of seismic energy (e.g., *Qamar*, 1988; *O'Neel et al.*, 2007; *Amundson et al.*, 2008; *Joughin et al.*, 2008; *Tsai et al.*, 2008). Previously reported seismic events have been recorded on networks that span a broad range of scales, from relatively small (earthquake magnitude 1-2) events recorded at kilometer-scales (*Qamar*, 1988; *O'Neel et al.*, 2007), up to magnitude 5 events recorded globally (*Ekström et al.*, 2003; *Tsai and Ekström*, 2007; *Nettles and Ekström*, 2010). Calving seismicity is distinct from tectonic earthquakes in both their proposed sources and the appearance of their waveforms. Typically, these calving-generated seismic events lack clear *P*- and *S*-wave arrivals, have emergent onsets and, when observed at regional scales (<100 km) in both Alaska and Greenland, have maximum power spectral densities between 1 and 5 Hz (e.g., *Wolf and Davies*, 1986; *Qamar*, 1988; *Amundson et al.*, 2008; *O'Neel et al.*, 2010; *Walter et al.*, 2012). However, despite widespread observation of calving seismicity, it remains unclear as to what part or parts of the iceberg calving process create these seismic signals.

Various mechanisms related to iceberg calving have been proposed as sources for calving seismicity. For example, glacial earthquakes most frequently associated with outlets of the Greenland Ice Sheet (summarized by *Nettles and Ekström*, 2010) have been ascribed to the rotation of buoyantly unstable icebergs following detachment (*Tsai et al.*, 2008; *Amundson et al.*, 2010). These icebergs scrape against the seafloor or the terminal cliff as they rotate, exerting a horizontally directed force. However, large, full thickness iceberg calving is absent at most glaciers in Alaska and Greenland (e.g., *Walter et al.*, 2010). Even where full thickness calving occurs, not every calving event involves this rotation mechanism. Thus, other potential seismogenic mechanisms must be active. Mechanisms reported in existing literature include ice fracture (*Neave and Savage*, 1970; *Deichmann et al.*, 2000; *Walter et al.*, 2009; *West et al.*, 2010), pressure fluctuations in subglacial conduits (*St. Lawrence and Qamar*, 1979; *Winberry et al.*, 2009; *West et al.*, 2010; *Carmichael et al.*, 2012), resonating water-filled cracks and hydro-fracture (*O'Neel et al.*, 2007), basal slip (*Wiens et al.*, 2008; *Winberry et al.*, 2011), and grinding and fracturing within an ice mélange (*Amundson et al.*, 2010). However, in many cases, no consensus exists on which mechanism or mechanisms are dominant.

Iceberg interactions with the sea surface represent another suite of potential seismogenic mechanisms. *Qamar* (1988) demonstrated that the change in gravitational potential energy associated with a moderately sized calving event may easily generate seismic waves with energies comparable to the icequakes reported by *Wolf and Davies* (1986). Ice-

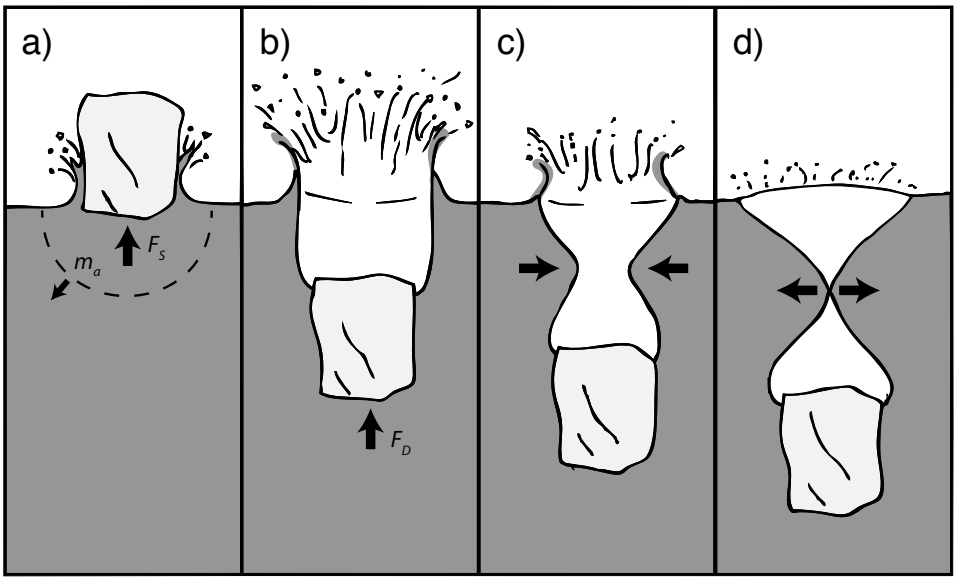

Figure 2.1. Cartoon representing four seismogenic mechanisms involving iceberg/fjord interaction: (a) slamming, i.e., momentum transfer to sea water, (b) iceberg deceleration, (c), cavity collapse, and (d) cavity pinch off. Arrows represent forces and accelerations. Illustration after *Gekle and Gordillo* (2010).

bergs that forcefully impact the water surface from above rapidly transfer momentum to the sea water, then more gradually continue to lose momentum through drag exerted against the surface of the iceberg. These momentum changes are associated with water accelerations that could be transmitted as compressional seismic waves. If an iceberg descends below the sea surface, then a submarine air cavity can form in the lee of the iceberg. The extremely high pressures developed during cavitation are known to be important in other geophysical disciplines (e.g., *Whipple et al.*, 2000; *Spray*, 1999) and the seismic signature of cavitation has been detected within volcanic magma conduits (e.g., *Chouet et al.*, 1997). In the case of calving, cavitation may also be seismically detectable. High-speed, "Worthington" jets that emerge from the sea surface following complete submergence of an iceberg are perhaps the most easily observed evidence of calving cavitation. Worthington jets occur when the walls of a collapsing cavity meet to fully enclose the cavity (*Gekle and Gordillo*, 2010). From the pinch-off point, jets of water emerge with velocities far in excess of the initial crown splash velocity. These iceberg/fjord interactions are schematically illustrated in Fig. 2.1. In this study, we explore the potential for iceberg-sea surface interactions to generate icequakes.

Before seismicity can be quantitatively tied to iceberg volume, glaciologists and seismologists must first be able to identify what mechanisms are releasing the observed seismic energy. The source of seismic energy, generated either by ice fracture, ice crumbling along the terminal cliff, rotating icebergs scraping the ocean bottom, or through iceberg interactions with the sea surface has major implications for how calving seismicity can be used in future glaciological investigations. To address the question of icequake seismogenesis, we return to the terminus of Yahtse Glacier, where *O'Neel et al.* (2010) identified a dense cluster of icequake epicenters.

2.3 Setting

Yahtse Glacier is an advancing, grounded, tidewater glacier and the largest of four glaciers that terminate in Icy Bay, Alaska (Fig. 2.2). It is 63 km long with a surface area of 1018 km^2 and consists of a broad, low-gradient upper basin between 900 and 1400 m elevation. This upper basin drains through an icefall (1% of glacier area) that falls from 700 m elevation to sea level over a distance of 5 km (this lowest reach is depicted in Fig. 2.2). Laser altimetry of the glacier's longitudinal profile and water depth soundings extrapolated from as close as 1.5 km from the terminus indicate that the glacier is approximately 170 m thick at its centerline, in water approximately 110 m deep. Thus, the terminus is grounded, as this height is well above the level at which it would float.

The terminus of Yahtse Glacier is composed of relatively fracture free seracs bounded by deep (> 30 m), transverse crevasses and highly fractured interstitial ice. The terminus-parallel dimension of the seracs is greater than the terminus-perpendicular dimension–likely a result of the principal tensile stress being oriented with the glacier flow direction. In timelapse photography looking across the direction of flow (introduced in the next section), ice motion within the last few hundred meters of the terminus sometimes appears to have a significant vertical component superimposed on its mean down-fjord motion. We interpret this vertical component as the glacier moving up and over a submarine terminal moraine.

Yahtse and its three tidewater neighbors in Icy Bay had completely filled Icy Bay in the late 19th century, extending 40 km beyond its present terminus to the Gulf of Alaska (*Porter*, 1989; *Barclay et al.*, 2006). At the conclusion of the Little Ice Age, the Icy Bay glaciers began retreating at an average rate of 400 m/yr. Simultaneous with this terminus retreat, the glacier above 700 m thinned insignificantly (*Muskett et al.*, 2008). In approximately

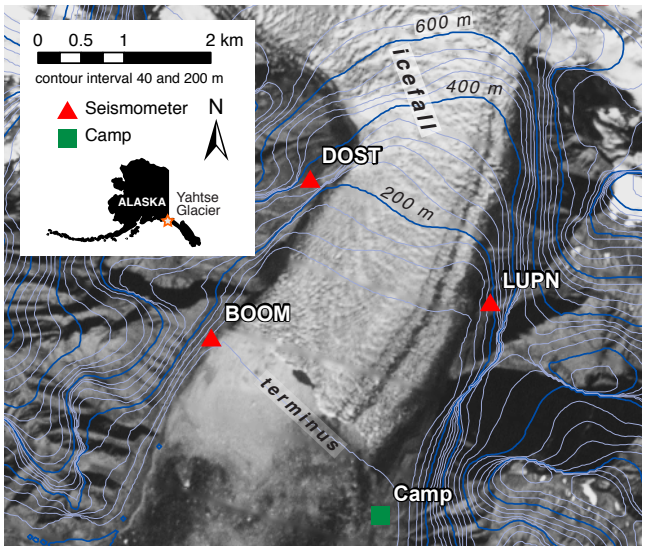

Figure 2.2. Map of lowest 5 km of 60 km-long Yahtse Glacier, including the icefall above the terminus. The locations of 3 out of 10 seismometers installed at the glacier margin are shown. Additional bedrock and in-ice seismometers, as well as on-ice GPS receivers, are off the map to the north, south, and west. Timelapse cameras taking photographs of the terminus every 20 min between June 2009 and September 2011 were at the locations of BOOM, DOST, and Camp. Background image is from the panchromatic band of Landsat 7 on 12 Sept. 2010, approximately 5 days after the video used in this study was recorded. Topography is from 2000, Shuttle Radar Topography Mission.

1990, Yahtse Glacier concluded the retreat phase of the tidewater glacier cycle and began advancing (*Meier and Post*, 1987); as of September 2011, the terminus of Yahtse Glacier is 2.0 km beyond this minimum position.

Icy Bay is also a known center of icequake activity. The Alaska Earthquake Information Center, as part of its long-term monitoring of earthquakes, has long recognized and cataloged seismicity associated with glacier activity as distinct from tectonic or volcanic sources (*Alaska Earthquake Information Center*, 2012). Many of these icequakes originate in the St. Elias Range, an approximately 80 km by 220 km glacierized region of southcentral and southeast Alaska, where Yahtse Glacier is located. In October 2006, 1016 icequakes were identified within the St. Elias range with a median local magnitude of 1.08 (*O'Neel et al.*, 2010). Of these, 51% of epicenters located within 15 km of the terminus of Yahtse Glacier; typical location errors were on the order of 5–10 km. An additional 37% of the icequakes located within 15 km of the tidewater termini of nearby Guyot and Tyndall glaciers. *O'Neel et al.* (2010) attributed this concentration of icequakes to calving and suggested that icequake detection algorithms could be used as calving counters in regions with tidewater glaciers.

2.4 Methods

Our analysis relies on three independent but complementary methods: seismic recordings, in-person observation of terminus calving events, and video recordings and time-lapse photography of the terminus. The data for this analysis were collected at Yahtse Glacier during 1 - 14 June and 7 - 8 September, 2010. These data represent a small portion of a much larger and more diverse dataset collected between June 2009 and September 2011.

2.4.1 Seismic recordings

During 2010, the seismic network at Yahtse Glacier consisted of sensors deployed on ice and on solid earth around the glacier. The seismic data discussed in this paper comes from the station closest to the glacier terminus, BOOM, installed on a $\sim$30 m high ledge, 400 m from the western edge of the 2010 terminus of Yahtse Glacier (Fig. 2.2). BOOM was one of ten broadband, 3-component seismometers installed on bedrock and in shallow sediment; the seismic signals recorded by the other stations are not markedly different than those from BOOM. The locations of three sensors are shown in Figure 2.2. Almost

all of these sensors, including BOOM, were Guralp 3Ts, with a flat response between 120 s and 50 Hz. We converted the seismic data from raw counts to velocity but did not correct for instrument frequency response. Because of the flat response and no gain within the frequency range of interest, instrument response deconvolution was unnecessary. All data were recorded by Quanterra 330 digitizers and balers sampling at 200 Hz.

2.4.2 Observer record

During June 2010, focused observation of the Yahtse Glacier terminus was maintained for 81 hrs over 13 days, in a manner similar to that used in *O'Neel et al.* (2007). Observation was carried out from camp at the eastern edge of the terminus. The field of view included approximately 60% of the glacier's terminal cliff. Observers recorded every visible or audible event, with a descriptor for the style or type of event, a qualitiative iceberg size, the event time, the event duration, and the event location on the terminus. Equally important, the timing of quiet periods without events was also recorded. Thus, variations in the rate of iceberg calving are documented. Calving style was recorded with one or several of the following identifiers:

1. submarine: iceberg rises buoyantly from below the waterline, rather than falling from above,
2. subaerial topple: intact serac or large serac pieces rotating out from the terminus, generally pivoting near the water line, prior to impact with the fjord,
3. subaerial drop: intact serac or large serac pieces falling straight down from the terminus,
4. loose ice avalanche of small, broken ice debris,
5. sudden "gunshot" event, heard but not seen,
6. rumble event, heard but not seen, and
7. not associated with Yahtse Glacier: glaciers and icebergs overturning in other parts of the fjord occasionally produce audible events.

The qualitative iceberg size was intended to describe the volume of ice involved in a calving event and is an integer with a minimum value of 1. This size scale is similar to

that of *O'Neel et al.* (2007), is non-linear and intended to be approximately logarithmic. Although this scaling is subjective, it provides a useful classification of larger vs. smaller events. Size 1 events are no more than roughly 15 m tall, 20 m wide and 10 m deep (in the along-flow direction). Size 3 events may incorporate the entire height of the glacier terminus (50-60 m), be 30 m wide and 20 m deep. The typical size 5 event incorporates the entire subaerial terminus height, is 200 m wide and 50 m deep. Calving events at Yahtse Glacier tend to be smaller than those of Columbia Glacier, Alaska. Therefore, this size scale is finer than that used by *O'Neel et al.* (2007), for whom a size 1 was equivalent to a 3 or 4 by the scale used in the present study. The largest size event observed at Yahtse during the observation period was assigned a 7. We assigned sizes to audible-only events based on the visible volumes of ice involved in similar sounding events.

Event duration is an estimate for the amount of time during which the calved ice motion is substantially vertical, i.e., during free fall or buoyant rise, or while sound was audible. Timing was kept with a watch synchronized to the second with a handheld GPS unit. Four people contributed to the 81 hrs of observations, typically in 1- or 2-hr shifts. Overlap between shifts, and several hours of training when two observers were present helped to maintain consistency throughout the record. These shift overlaps and comparisons of the simultaneous records do not reveal any clear biases among the different observers.

2.4.3 Video and timelapse photography

Between 6-11 September 2010, 8.4 hrs of video were recorded of the terminus from Camp (Fig. 2.2). Video was recorded with a Canon EOS 7D digital camera, shooting at 29.97 frames per second. Absolute timing was kept with a handheld GPS that was occasionally passed into the frame of the video so that the time on the screen was visible for several seconds. Following fieldwork, we made repeat measurements of the lag between the handheld GPS time and UTC, as reported by a millisecond-accurate clock. The lag of 14 comparisons made over two months approximated a normal distribution with a mean of 0.01 s and a standard deviation of 0.44 s. However, additional errors arise when we synchronize seismic data with these videos in the sections that follow. Thus we conservatively consider our video (with 0.033 s precision) to be synchronized via GPS to UTC (and the seismic data) with an accuracy of < 1 s (*Welty et al.*, 2013).

Table 2.1. Number of observer-recorded Yahtse terminus events per type. A given terminus event may consist of multiple different types, and thus be present in the count for more than one event type.

Event type	Heard ("rumble")	Heard ("gunshot")	Avalanche	Drop	Topple	Submarine
Number of events	2814	305	219	1388	79	112

Three digital SLR cameras were arrayed around the glacier terminus at the locations of the BOOM and DOST seismometers and at Camp. These cameras captured images of the terminus every 20 minutes during daylight hours for the duration of our 27-month project.

2.5 Results

The combination of seismic data with a long time series of in-person, direct calving observations and high-frame-rate video allows us to investigate the relationship between iceberg calving and glaciogenic seismicity at both inter-event (minutes to days) and intra-event (seconds) timescales.

2.5.1 Inter-event timescales: minutes to days

During the observer period, we recorded 4659 observed events at or within a short distance behind the Yahtse terminus, at an average rate of one per 63 s (Fig. 2.3). An additional 134 events were heard to originate from Guyot or other glaciers, or from within Icy Bay, apart from the Yahtse terminus. We discard these non-Yahtse events for the purposes of this study. Of the Yahtse events, 36% were seen; the others were only heard. The rate at which events occurred was not steady; strong variations in event rate were apparent at both hourly and multi-day timescales. Calving events also clustered spatially along the face of the terminus. Many calving events would occur in succession at one location over a period of 10 minutes or more while other regions of the terminus were quiet. Only 2.4% of calving events involved iceberg releases from below the sea surface (submarine events), although these tended to involve larger icebergs than subaerial calving events (similar to other observations (*Motyka*, 1997; *O'Neel et al.*, 2007)). Frequently, submarine events were part of a longer, more complicated sequence of calving that also included subaerial components (*Motyka*, 1997). Tables 2.1 and 2.2 present a summary of the observer record.

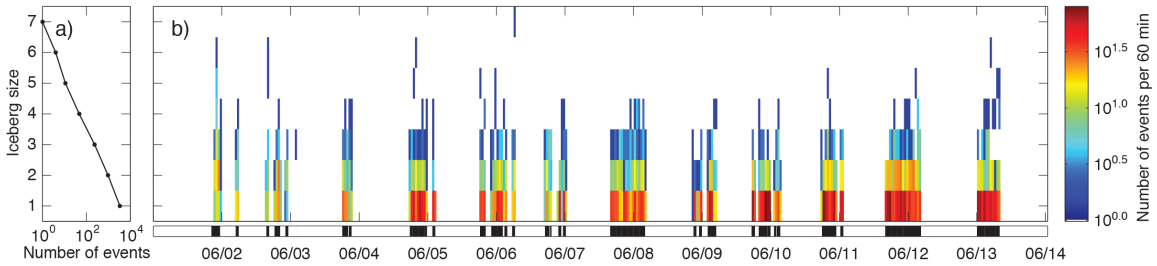

Figure 2.3. Observed events at the terminus of Yahtse Glacier during 12 days of observation, June 2010 (UTC time). a) Total number of events observed per iceberg size (Table 2.2). b) Event rate over the 12 day observer record per iceberg sizes, where the color scale represents the event rate on a logarithmic scale. The black bars at the base of the figure identify periods during which an observer was present.

Table 2.2. Number of observer-recorded Yahtse terminus events per size.

Iceberg size	1	2	3	4	5	6	7
Number of events	3329	962	235	47	11	4	1

The simultaneous operation of our seismic network with the observer record allows us to identify relationships between calving events observed at the terminus of Yahtse Glacier and icequakes (Fig. 2.4). This comparison and others like it reveal several interesting patterns:

1. Approximately 75% of seismic events have a near-synchronous observed terminus event in the observer record. However, the converse is not necessarily true; many brief (< 5 s), small size (≤ 2) observed events do not have coincident seismic events identifiable above the background seismicity. Time lags on the order of 15 s between the onset of an icequake and its associated calving event most likely reflect inaccuracy by the human observers.

2. Almost every visually-observed, subaerial calving event (i.e., avalanches, drops, and topples) also has an associated seismic event. However, most of the audible-only events do not have a coincident seismic event.

3. Iceberg size and peak icequake amplitude are weakly related.

4. Topple events, which were generally observed to create the largest splashes as ice impacted the fjord surface, often are associated with the largest amplitude seismic

events. For example, the largest amplitude icequake in Figure 2.4 (at 11 June 2010 21:57) is associated with a relatively modest (size 3) topple event.

5. Submarine calving is associated with relatively low amplitude seismicity, unless the calving event was multi-part and also had a drop or topple (i.e., subaerial) component.

6. The observer-recorded duration of terminus events correlates well with the duration of seismic events.

2.5.2 Intra-event timescales: seconds

The largest subaerial calving events at Yahtse Glacier are observed to involve brittle failure of the ice supporting the base of intact seracs. Visual inspection of 20-minute-interval timelapse photographs taken perpendicular to the flow direction from the station BOOM reveal that seracs may slowly rotate top-out from the terminus for up to 4 hrs prior to calving. In addition to intact serac release, calving occurs as the release of interstitial ice from between less-damaged seracs and from the collapse of portions of seracs along pre-existing planes of weakness. However, the more closely one observes the terminus of Yahtse Glacier, the more continuous calving appears. Frequent small cracks and crumbles that are undetectable at kilometer distances are apparent at 100 m distances. More commonly, the human experience of calving is dominated by an awareness only of the infrequent, larger calving icebergs. Our observer record reflects this: discrete calving events punctuate relatively long-duration periods of quiet. While we document the largest calving events, there are undoubtedly many smaller events which we were unable to detect from our > 0.5 km distance from the terminus.

As at other glaciers, a large calving event at Yahtse Glacier may be viewed as the sum of many smaller contributing calving events(*Qamar*, 1988; *Motyka*, 1997). Furthermore, small calving events consist of several distinct parts. Small, subaerial calving events with iceberg size 1 or 2 (the most frequent calving events at Yahtse) have typical durations of 10 s and consist of (1) ice fracture and iceberg detachment, (2) iceberg fall and acceleration towards the water surface, (3) "crown" splash as the iceberg begins to displace water at the sea surface and decelerate, and, in some cases, (4) the creation of a high-speed, Worthington jet following complete submergence of the iceberg below the water surface (*Gekle and Gordillo*,

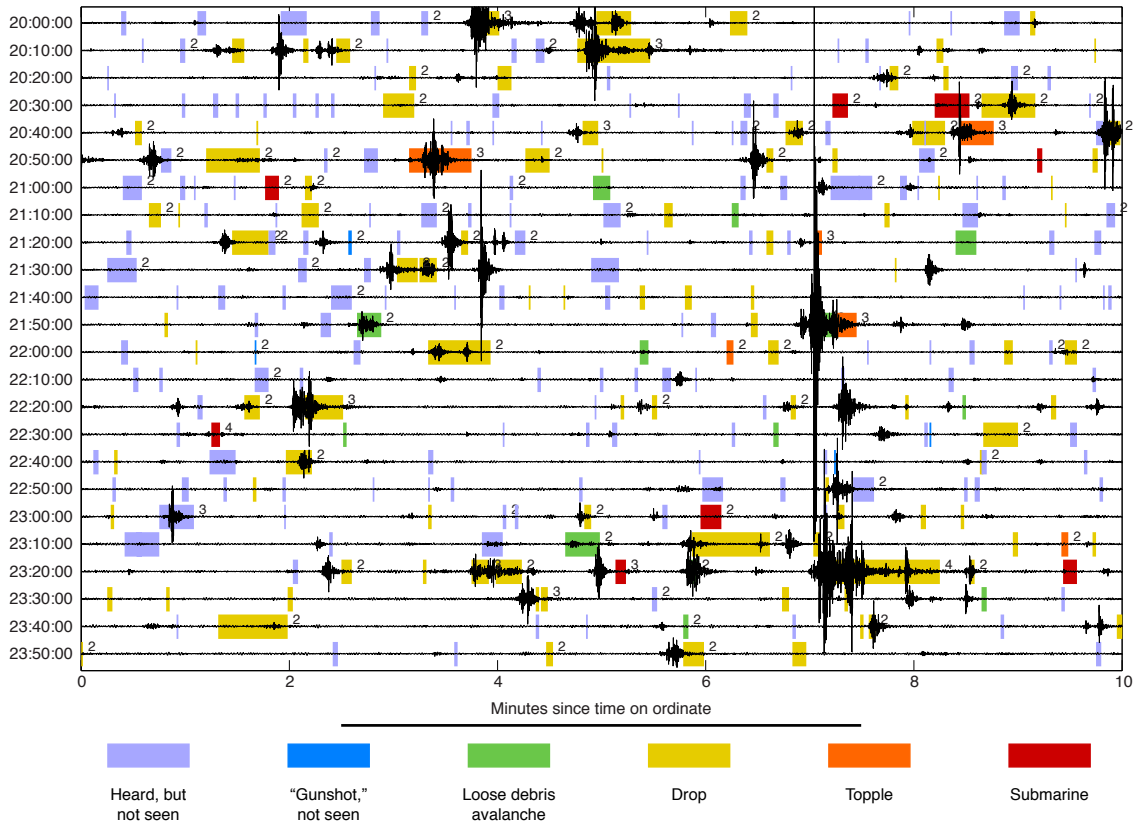

Figure 2.4. Four hours of seismic data with individual Yahtse terminus events from the calving observer record superimposed. Seismograms recorded on the vertical channel of BOOM (black lines) are shown, ten minutes per line, beginning 11 June 2010, 20:00:00 UTC, a time period with particularly frequent calving (Fig. 2.3). The differently colored symbols represent different *styles* of terminus events. Although a single calving event may occur as a chain of linked events with different calving *styles*, only one *style* is identified per event. The hierarchy of styles used for plotting is as presented in the text, regardless of the temporal style order. That is, for an event that began as a subaerial drop, followed with a topple, and then ended with a loose avalanche, the event will be identified as a subaerial topple. Length of colored bar is the duration of the observed event. Observed iceberg sizes greater than one are identified with a number to the right of the colored bar. No earthquakes in the catalogs of the Alaska Earthquake Information Center or the USGS Preliminary Determination of Epicenters are visible in this figure. Seismograms are filtered between 0.5 and 5 Hz.

2010). Larger calving events result from larger blocks of detached ice and the simultaneous or enchained occurrence of several smaller events.

2.5.2.1 Synchronous calving and seismic observations: 'What are the mechanisms responsible for calving seismicity?'

To examine the sources and patterns of calving seismicity, we synchronized seismic data from the vertical channel of BOOM with video of 70 calving events. Of these, 57 events were sufficiently well-recorded by both video and seismometers to use in our analyses. Two example videos are available as supplementary material (http://onlinelibrary.wiley.com/ doi/10.1029/2012JF002513/suppinfo and on the CD accompanying this dissertation). For each of these calving events, we can track the icequake ground motion through our seismic network to 13 km distances. Relative to the extended durations of recorded icequakes, the observed dispersion is small; qualitative icequake duration recorded at a sensor 12 km from the source is approximately 1.5 times the duration recorded at BOOM, 1.8 km from the source. Thus, due to its proximity, the timeseries of ground velocities recorded at BOOM is largely controlled by the source time function. We time shift the recorded seismogram back to the origin time using the source-receiver distance and the average speed at which the maximum icequake ground velocity moves through our network (1.9 km s^{-1}). Although this is a rough estimate, the correction (≤ 1.1 s) is smaller or on par with errors in video timing and is far shorter than the event durations.

Two example calving events To characterize our observations from the 57 calving events with synchronized seismograms and video, we present two simple, typical, well-recorded examples of different types of calving (Figs. 2.5 and 2.6 and supplementary videos 2.S.1 and 2.S.2). To discern if different mechanisms emit seismic energy in different frequency bands, we present spectrograms of seismic data surrounding each calving event.

In the first example, which we refer to as "Block" (Fig. 2.5 and video 2.S.1 of the supplementary files, http://onlinelibrary.wiley.com/doi/10.1029/2012JF002513/suppinfo), a large, intact block falls from high on the terminus, entrains a small additional amount of ice during its fall, creates a large crown splash, and then emits a Worthington jet that launches ice fragments over 100 m into the air, nearly twice the terminus height (visible in video 2.S.1). In this example, weak 4–15 Hz seismic signals precede and coincide with

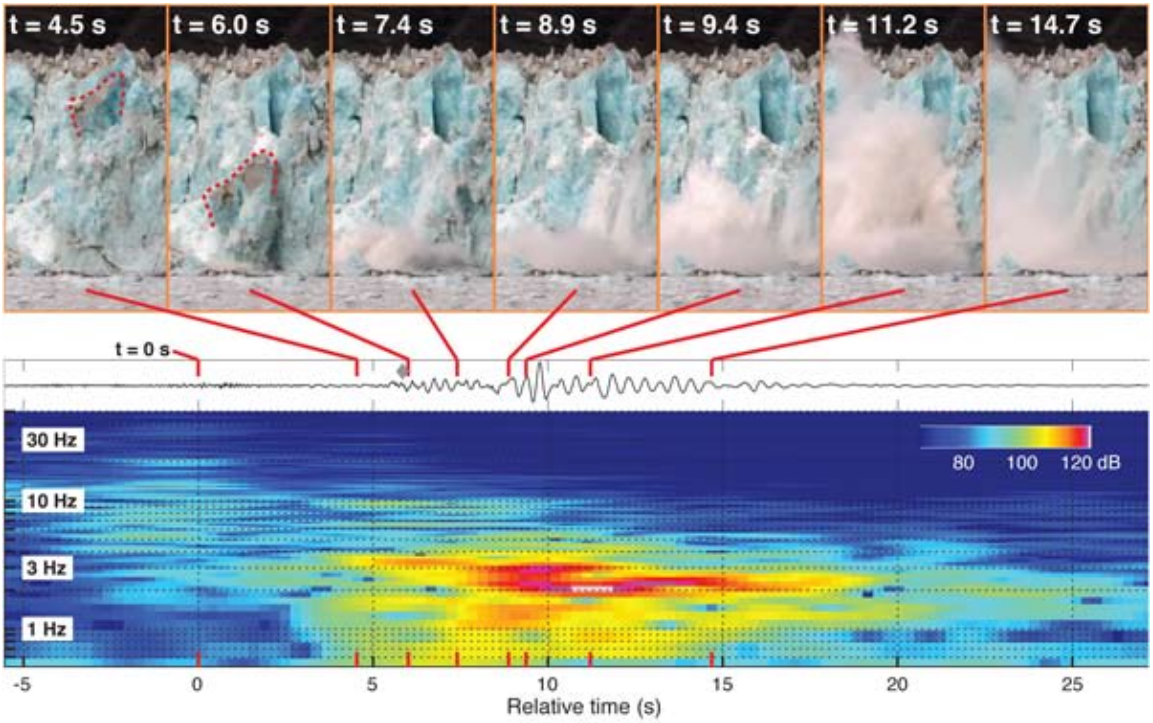

Figure 2.5. Video stills and seismic data for calving event "Block" at the terminus of Yahtse Glacier. The lower panels show the unfiltered waveform from the vertical channel of BOOM and the waveform spectrogram. Terminal cliff is approximately 60 m tall. Event has an iceberg size of 3 and a 18 μm s^{-1} maximum ground velocity. In the first two panels from video, the top of the major detached block is outlined with a red, dashed line. Ice associated with the calving event is observed to begin falling at 7 Sept 2010, 22:13:50.3 UTC (t = 0). The time of each video panel is identified in seconds relative to t = 0 and marked on the seismic data by vertical red ticks at the top of the waveform and bottom of the spectrogram. Seismic data has been shifted forward 0.95 s to correct for seismic wave travel time. A "step" in the icequake amplitude is identified with a gray diamond. At 8.8 s, a Worthington jet emerges from the fjord. The spectrogram presents the velocity of the sensor (in dB) as a function of frequencies between 0.5 and 50 Hz, as a function of time. Video of this calving event, synchronized with the seismic data, is available as video 2.S.1 of the supplementary files.

the release of several small ice fragments from around the largest iceberg block (t = 0 s). At 3.5 s, the initial small fragments begin to collide with the fjord surface at the same time as a rapid increase in lower-frequency 1–3 Hz seismic energy. Between 5.6 and 8.9 s, the rain of larger icebergs collides with the fjord surface and a "step" in the seismic amplitude occurs, with peak power between 1 and 4 Hz. Additional lower-amplitude seismic signals between 6 and 10 Hz coincide with these impacts. At 8.8 s, the Worthington jet erupts from the fjord surface with greater velocity than the splashing observed previously. At 9.0 s, the amplitude of the low frequency 1-3 Hz seismic waves increases yet again and the unfiltered seismic waves reach their maximum amplitude, 18.3 μm s^{-1}, at 9.7 s. By 10.5 s, all debris has completely fallen from the terminus, but seismic amplitudes between 0.6 and 4 Hz remain strong. A protracted coda eventually approaches background levels at around 20 s. The amplitudes between 2 and 3 Hz exceed the amplitudes at other frequencies throughout the duration of the calving event by 20 db.

In the second example, which we refer to as "Flake" (Fig. 2.6 and video 2.S.2 of the supplementary files, http://onlinelibrary.wiley.com/doi/10.1029/2012JF002513/suppinfo), an entire, intact serac-flake collapses from the terminal cliff. The volume of calved ice in Flake appears to be twice that of Block (Fig. 2.5) and, although crown splashing is present, no Worthington jet is observed. This calving event initiates with the release of several small ice fragments, barely visible in the recorded video (t = 0 s). No significant seismicity is coincident with these small releases. At 4.0 s, ice on the right-hand-side of the intact flake crumbles and breaks away, coincident with the initiation of weak seismicity at frequencies that span the range from 0.5 to 10 Hz; ice on the left-hand side follows at 4.9 s. At 6.0 s, the large, intact flake begins to fall and at 6.3 s, water at the base of the flake is seen displaced by the collapsing flake. These events are coincident with an increase in energy across a range of frequencies, although ground motion near 3 Hz is approximately an order of magnitude greater than that at other frequencies. Between 6.7 and 7.9 s, crown splashing associated with the impact of the right-hand-side ice is seen in the video and the peak frequencies spread down to include 1.5 Hz. Crown splashing and a surge of water spreads to the left along the terminus while the ground velocity peaks at 9.5 s (5.9 μm s^{-1}, one third the peak amplitude of Block). At 11.4 s, the top of the large flake has slipped below the sea surface and the largest splashes have concluded. Thereafter, several more moderately-sized ice fragments fall from the same region of the terminus until 23 s, during which time the 1.6–4 Hz coda slowly decreases in amplitude. A second wave of calving,

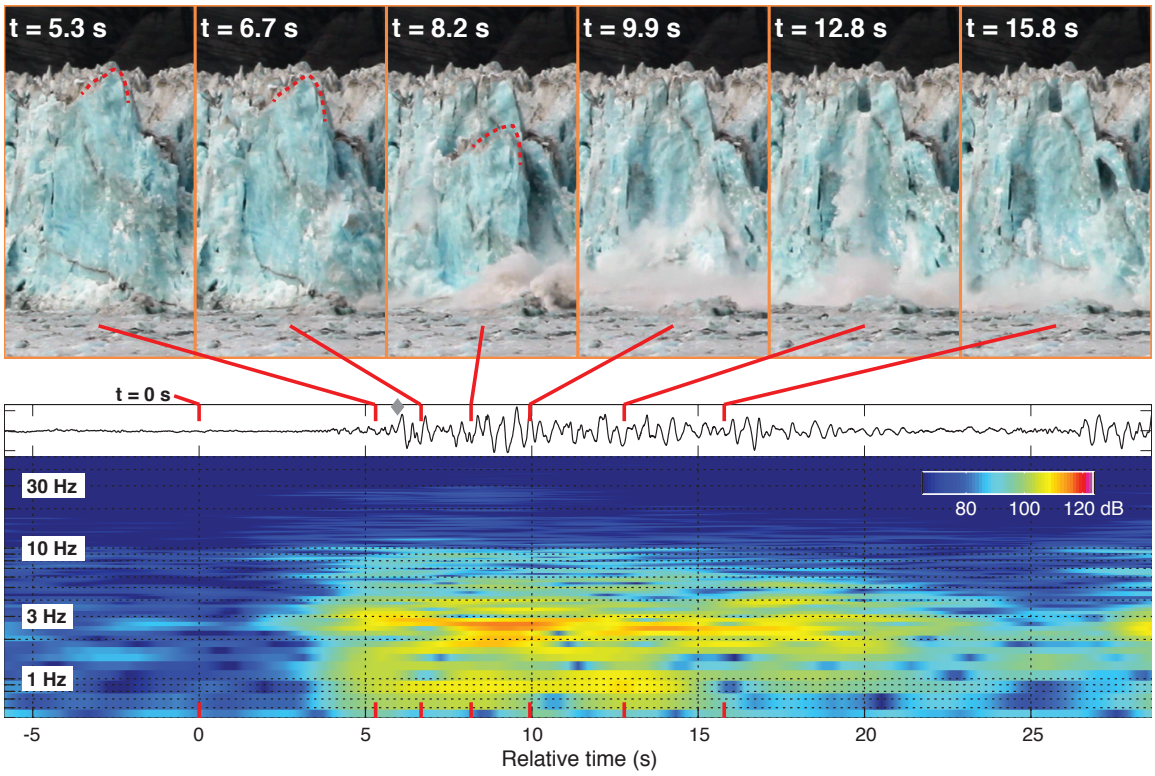

Figure 2.6. Video stills and seismic data for calving event "Flake" at the terminus of Yahtse Glacier. Data are similar to that presented in Fig. 2.5. Event has an iceberg size of 4 and a 6 μm s^{-1} maximum ground velocity. In the first three panels, the top of the collapsing serac/flake is outlined with a red, dashed line. Ice associated with the calving event is observed to begin falling at UTC 7 Sept 2010 23:17:51.6 (t = 0). No Worthington jet is associated with this calving event. Seismic data has been shifted forward 0.94 s to correct for seismic wave travel time. Video of this calving event, synchronized with the seismic data, is available as video 2.S.2 of the supplementary files.

including another flake similar in size, shape and location to the first flake, begins at 24.6 s.

Common characteristics of calving icequakes The two calving events and icequakes described above are representative of Yahtse's calving seismicity (Fig. 2.9). Nearly all of the well-recorded calving icequakes recorded at BOOM lack clear *P*- or *S*-wave arrivals and have 5–30 s durations, emergent onsets, and relatively constant low-amplitude early portions that typically "step" to larger amplitudes. In Block, Flake, and almost all of the calving icequakes, the seismic amplitude in the frequency band from 0.5 to 5 Hz (peaked near 3 Hz) exceeds the amplitude at higher frequencies (see section 2.5.2.2). Below 0.5 Hz, icequake amplitude appears to decrease, although we are limited from examining these lower frequencies by the presence of ocean microseism between 0.1 and 0.5 Hz (*Stein and Wysession*, 2003) (Fig. 2.7). The largest amplitude seismic waves very often correlate in time with interactions between icebergs and the sea surface (Fig. 2.8). Worthington jets appear in 30 of our 57 calving events after largely intact blocks of ice fall from high on the terminal ice cliff and briefly submerge below the sea surface. In these cases, the time of jet eruption coincides well with the time of the peak seismic amplitude (Fig. 2.8a), often 5 s after the iceberg initially hits the fjord surface and the crown splash forms.

Seismic waves at 1–5 Hz frequently exhibit a "step" in their amplitudes and energy early in the evolution of the icequake, when the seismic amplitude may double or more (equivalent to an increase of > 6 dB, Fig. 2.9). Steps in icequake amplitude are also present at t = 5.8 s for Block and t = 5.9 s for Flake (Figs. 2.5 and 2.6 and videos 2.S.1 and 2.S.2). These steps occur with or without jets, were coincident with the biggest splash of the iceberg (the crown splash) and typically lag the detachment of the iceberg from the glacier's terminal cliff by 2 to 4 s (Fig. 2.8b). Seismic waves at 0.5–5 Hz are also associated with iceberg detachment, but these waves are lower amplitude than those related to iceberg splashing.

Seismic waves at greater than 5 Hz are associated better with ice crumbling and fracturing than with splashing, and almost always at least 10 dB weaker than lower frequency energy. However, calving events that create small splashes have commensurately weak seismic waves between 0.5 and 5 Hz. In these cases, the amplitude of higher frequency seismic waves can equal that of the lower frequency waves.

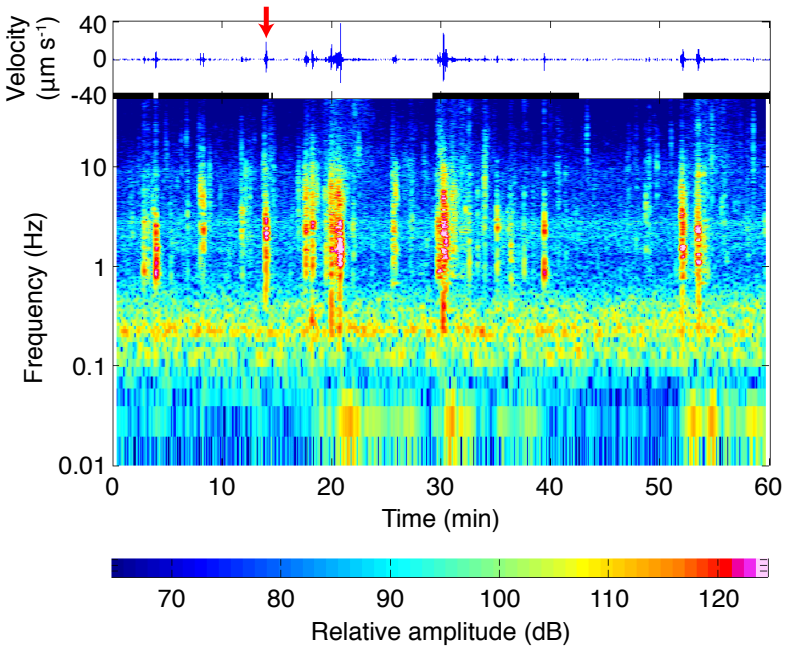

Figure 2.7. One hour spectrogram from the vertical channel of BOOM, starting 7 Sept 2010 22:00:00 UTC. Video of the terminus was recorded during the time period identified with the black band between the seismogram and spectrogram. The icequake generated by example event Block (Fig 2.5) is marked with the red arrow. Inspection of video and an observer record reveal that most of the other icequakes can also be associated with calving events. Decibel scale is the same as in Figs. 2.5 and 2.6.

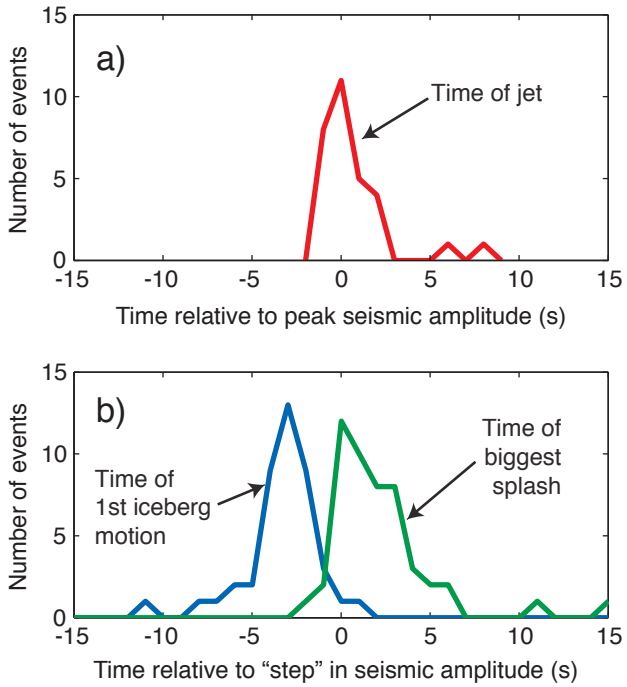

Figure 2.8. Time lags between stages of iceberg calving and seismic events, rounded to the nearest second. (a) Time lag between the peak seismic amplitude and Worthington jets visible in the video. Thirty jets associated with calving events were identified. (b) Time lag between large amplitude “step” in the seismic amplitude and (at left) the first motion in the video of the large collapsing iceberg, and (at right) the largest splash of the calving event. “Steps” are a common feature of the calving icequake waveforms (Figs. 2.5, 2.6 and 2.9).

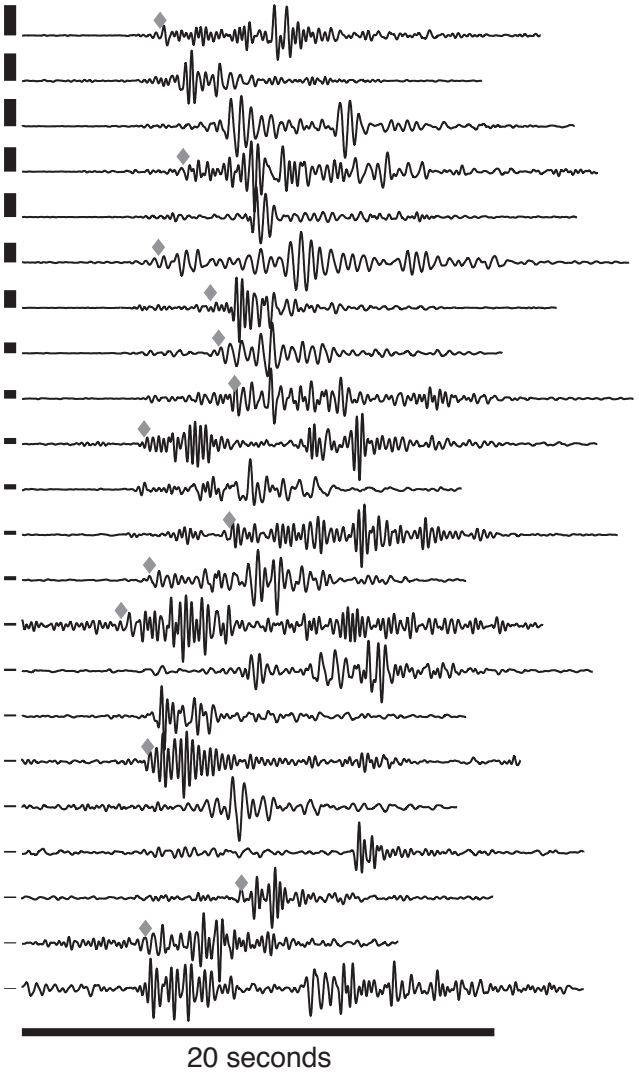

Figure 2.9. Example icequakes resulting from subaerial calving events in the observer record. The third icequake from the bottom is the result of a topple event. All others resulted from drop calving events. Events occurred between 20:00 and 21:00, 11 June 2010, the first hour of the data presented in Fig. 2.4. Seismograms were recorded on the vertical channel of BOOM and are shown filtered between 1 and 5 Hz. Icequake amplitudes are normalized, with the relative amplitude of each event indicated by the height of the vertical black bar to the left of the icequake. The top seismogram, with the largest amplitude, reaches a peak of 22 μm s^{-1}. Gray diamonds above many of the seismograms identify "steps" in the seismic amplitude that are discussed within the text.

2.5.2.2 Frequency content of calving icequakes

In both the Block (Fig. 2.5) and Flake (Fig. 2.6) examples, the amplitude of ground motion between 1 and 3 Hz exceeds that at higher frequencies. The spectra of these two examples are shown in Figure 2.10, along with the spectra from a set of local, tectonic earthquakes and a period during which no calving events are observable in the video and no clear seismic events occurred. The 10 earthquakes have magnitudes $1.0 < M_L < 1.5$ and are located within 30 km of BOOM by the Alaska Earthquake Information Center. Block, Flake and the earthquakes each have seismic energy at levels greater than that of background for all observed frequencies. However, the shapes of the earthquake and icequake spectra have clear differences. Relative to the earthquakes, the icequakes have comparable seismic amplitudes between 5 and 10 Hz and have lower amplitudes between 10 and 20 Hz. The two icequakes are most different from the earthquakes in the frequency range between 1 and 3 Hz, where the spectra exceed the median earthquake amplitude by an order of magnitude or more. This result is consistent with previous studies that have associated strong 1–3 Hz seismicity with iceberg calving (*Wolf and Davies*, 1986; *Qamar*, 1988; *O'Neel et al.*, 2007; *Walter et al.*, 2012).

Throughout the spectra, including within the 1–3 Hz band, Block and Flake have multiple, distinct peaks of nearly equal amplitude, as do the earthquakes. The presence of these multiple spectral peaks was common amongst the 57 calving events for which video was recorded. The specific frequencies of 1–3 Hz peaks and troughs vary amongst our recorded calving events, with no persistent maxima or band gaps. Among the video-recorded calving events, the median peak frequency was 2.3 Hz with an interquartile range of 0.7 Hz; 92% of calving events had a peak frequency between 1 and 5 Hz. Across our network, the value of this peak frequency decreased only slightly ($\lesssim 0.5$ Hz) as the seismic waves traveled the 12 km out from terminus.

None of the calving events observed were of sufficient size or duration to generate seismicity such as the glacial earthquakes reported in *Ekström et al.* (2003) and elsewhere. However, ground motion with 25–50 s periods was detected above background levels at BOOM 1 to 3 minutes after many icequakes with amplitudes in excess of 10 μm s^{-1} (Fig. 2.7). The source of this ground motion is different than that described in *Tsai et al.* (2008) and *Amundson et al.* (2010). For events with simultaneous video, these very-long-period seismic waves coincided with the arrival of water waves with comparable periods arriving

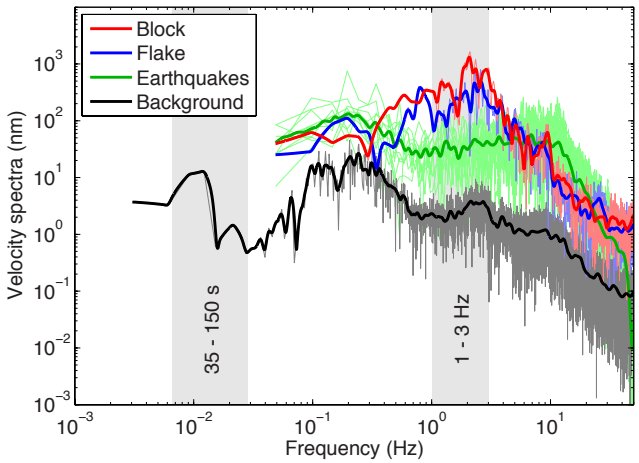

Figure 2.10. Comparison of velocity spectra from the two calving events displayed in Figs. 2.5 and 2.6, local earthquakes and background seismicity. Ten local earthquakes within the magnitude ranges of $1.0 < M_L < 1.5$ are shown in pale colors. Smoothed spectra are displayed bold on top of the unsmoothed spectra; the earthquake spectra have been stacked prior to smoothing. Durations for which spectra are displayed are 18 s for the Block, 19 s for the Flake, 20 s for each earthquake and 300 s for background. All waveforms are from the vertical channel of BOOM, as reported elsewhere. The BOOM sensor has a flat response to seismic signals between 0.008 and 50 Hz. Two gray-shaded rectangles identify the frequency ranges discussed in previous studies of glacial earthquakes (e.g. *Ekström et al.*, 2003) and icequakes (e.g. *O'Neel et al.*, 2007).

on the shore. These earth-loading signals are absent from stations more distant from the shoreline. Some very-long-period signals exhibited dispersion, consistent with the arrivals of surface (water) waves (*Amundson et al.*, 2008, 2012).

2.6 Discussion

2.6.1 Contributions to the seismicity of Yahtse Glacier

Based on an examination of Fig. 2.4 and other figures like it, iceberg calving at Yahtse Glacier dominates the locally-recorded seismic wavefield and can be conclusively identified as the source of at least 75% of icequakes recorded near the glacier terminus. In actuality, given the consistent appearance of most of the waveforms (see section 2.5.2.1) and considering that only 60% of the terminus was visible from our observation point, the calving contribution to the local seismic wavefield may be even greater.

Within a single calving event, interactions between the iceberg and the fjord surface (i.e., splashing, jetting) are the most seismically energetic sources. In particular, cavitation (identified by the occurrence of Worthington jets created by collapsing air cavities) is the mechanism identified with the greatest potential for large amplitude seismic waves (Fig. 2.5 and 2.8). This mechanism, with the entrainment of a cavity above the plunging iceberg and the subsequent collapse of an enclosed air bubble, is akin to the firing of air-guns, commonly used in marine seismic surveys as an active seismic source (e.g., *Stein and Wysession*, 2003).

The association between iceberg-sea surface interactions and high amplitude icequakes offers a potential explanation for the lack of coincidence between audible-only terminus events and icequakes (Fig. 2.4). Many of these audible-only terminus events sounded as though they originated from behind Yahtse Glacier's terminal cliff. We suspect that these audible-only events were generated by serac collapse within the highly-crevassed lower reach of Yahtse Glacier. If the falling serac ice blocks never impact the fjord surface, then they do not splash nor lead to cavitation beneath the water surface–the mechanisms of strongest icequake generation in our study.

These observations further support the conclusions of *O'Neel et al.* (2010): calving is the source of the concentrated epicenters at the head of Icy Bay. Thus, not only are ice-water impact and cavitation the most seismically energetic parts of iceberg calving, they appear to be the most common and efficient of any glaciological process acting within the ice-rich and glaciologically diverse St. Elias Range of Alaska and Yukon Territory. Yahtse

Glacier produces smaller icebergs than other Alaskan Glaciers, where $> 2 \times 10^6$ m^3 of ice can be released in a single calving event (*Motyka*, 1997; *O'Neel et al.*, 2007). We propose that the relative stability of this grounded, advancing glacier (shallow, 110 m, water depth and terminus height ∼45 m above its flotation threshold) limits the maximum size of individual calving events. This height above buoyancy is close to the level observed previously for stable tidewater termini (*van der Veen*, 1996). Closely-spaced crevasses and crevasse penetration through the entire subaerial portion of the terminus serve to further limit the maximum size of calving events. In spite of these limitations on calving event size, Yahtse Glacier remains a regional "hot spot" of icequake occurrence due to the high occurrence rate of icebergs falling from high on the glacier terminus.

Fjord interaction mechanisms are certainly not the only seismogenic mechanisms associated with iceberg calving. We record relatively weak seismicity at frequencies > 5 Hz often associated with the earliest parts of a calving event, including during and preceding iceberg detachment and clearly before any apparent splashing. Energy at these higher frequencies is particularly strong in calving events with significant crumbling and avalanching character, supporting previous research that suggests high frequency seismicity in glacial environments is related to ice fracturing (*Neave and Savage*, 1970; *Deichmann et al.*, 2000; *Walter et al.*, 2008; *Carmichael et al.*, 2012).

We do not discount potential contributions from the other mechanisms listed in the introduction, including basal slip, subglacial conduit hydraulics, grinding of ice mélange, unloading of the remaining ice surface, or resonance of water filled-fractures or of free-standing seracs. Indeed, relatively low-amplitude, 0.5–5 Hz seismicity coincident with iceberg detachment is common. In the present work, we are unable to identify the exact source of this early part of the calving waveforms (that beginning at t = 3.3 s and t = 4.8 s in Figs. 2.5 and 2.6), but vibration of water-filled cracks (*Métaxian*, 2003; *O'Neel and Pfeffer*, 2007; *Winberry et al.*, 2009) or the remaining serac, or friction and/or collisions between the falling block and the terminal cliff remain possibilities.

2.6.2 Source mechanisms

We envision four mechanisms by which icebergs could interact with the sea surface to generate seismic energy. These are sequentially: (a) the moment of impact of an iceberg on the fjord surface, when momentum is rapidly transferred from the falling iceberg to the sea water, (b) the deceleration of the iceberg through the water, under the influence of drag

and buoyancy, (c) in the case of complete submergence of the iceberg below the sea surface (i.e., cavitation), the inward acceleration and collapse of the walls of the below-sea-surface air cavity, and (d) the moment of air cavity pinch off, when the water walls, all moving radially inward, contact each other, accelerate outward, and generate a Worthington jet (Fig. 2.1). Slamming (mechanism (a)) will only occur in the case of subaerial calving; however iceberg deceleration and cavitation seismogenesis can also occur during submarine calving, particularly if a rising iceberg has sufficient momentum at the sea surface to carry it substantially above its position of hydrostatic equilibrium. This is most likely to occur at tidewater termini in deep fjords (e.g., *Motyka*, 1997; *O'Neel et al.*, 2007)

The timescales for these four mechanisms vary from nearly instantaneous impulses, (a) and (d), to longer-duration mechanisms that evolve over tenths to whole second durations, (b) and (c). The more impulsive mechanisms may generate ground motion across a wide range of frequencies, just as a Lamb pulse or delta function contains energy at all frequencies (e.g., *Kanamori and Given*, 1983). The three-dimensional structure of our field site, including soft, glaciomarine mud that blankets the fjord bottom, has the potential to trap and amplify some frequencies of seismic waves (*Kennett*, 2002). However, further exploration of these path effects would tell us more about geologic structure and the transmission of seismic waves than about the seismic source. Thus, we focus on the iceberg deceleration (b) and cavity collapse (c) mechanisms. If the forces associated with iceberg deceleration and cavity collapse act over durations similar to half the wave period at the peak seismogram amplitude, then we gain confidence that this mechanism may be a significant part of the icequake source (*Stein and Wysession*, 2003).

2.6.2.1 Set-up of hydrodynamic model

We first consider the vertical deceleration forces on an idealized, vertical, cylindrical iceberg, with bottom radius R and height H (mechanism (b), above). We define z as the height of the iceberg bottom above the water surface. Thus, $m = \rho_i H \pi R^2$ is the mass of the iceberg, where ρ_i is the ice density, 917 kg m^{-3}. During iceberg impact on the fjord surface, the iceberg will transfer some of its momentum to the water (mechanism (a)), and accelerate that water along its downward trajectory. The mass of the entrained water is accounted for as an *added mass*, m_a, which is defined for periodic motion of a solid object within a fluid (*Sabunco and Calisal*, 1981; *De Backer et al.*, 2009). For the case of abrupt impact, the high frequency limit is appropriate. The expression for the added mass of a normally incident,

impacting, vertical cylinder is:

$$m_a = 0.37\pi\rho_w R^3 \tag{2.1}$$

(*Korotkin*, 2009; *Sabunco and Calisal*, 1981), where ρ_w is the density of seawater (1014 kg m^{-3} for temperature and salinity conditions near the terminus of Yahtse Glacier, unpublished hydrographic data).

The equation of motion is

$$\frac{d}{dt}(m + m_a)U = mg - F_B - F_D \tag{2.2}$$

or equivalently

$$(m + m_a)\frac{dU}{dt} = mg - F_B - F_D - U\frac{dm_a}{dt} \tag{2.3}$$

where U is the iceberg velocity, dz/dt, g is the gravitational acceleration, F_B is the buoyancy force, and F_D is the drag force. The relative importance of surface tension and inertia is given by the Weber number, which in this case indicates that surface tension is negligible. The buoyancy and drag forces are defined as

$$F_B = \rho_w \left(W_r \pi R^2 H\right) g \tag{2.4}$$

where W_r is the wetted ratio of the iceberg height, between 0 and 1, and, for $z < 0$,

$$F_D = \frac{1}{2} C_D \rho_w \pi R^2 U|U|, \tag{2.5}$$

where C_D is the drag coefficient. The drag coefficient depends on the shape and roughness of the iceberg and on the nature of the water flow around the iceberg, typically described by the non-dimensional Reynolds, Re, and Froude, Fr, numbers (e.g., *May and Woodhull*, 1948; *Gaudet*, 1998; *Goossens*, 1987):

$$\mathrm{Fr} = \frac{U^2}{gR}, \qquad \mathrm{Re} = \frac{UR}{\nu} \tag{2.6}$$

where ν is the kinematic viscosity of water. For an iceberg with R = 8 m, after free fall from a height of 20 m, Re = 9.5×10^7 and Fr = 5 at the moment of impact. Although the values of Re and Fr, and therefore C_D, will change as the iceberg begins to decelerate, we are most interested in the first seconds after impact, when the drag force is greatest. Furthermore, C_D is substantially controlled by the location on the iceberg where laminar flow separates from the iceberg surface and turbulence initiates. For a smooth, circular disk pressed through a fluid, *Batchelor* (1967) reports that the location of this flow separation is fixed at the sharp disk edge for Re $\gtrsim 3 \times 10^3$, and thus C_D (with a value of 1.1)

is independent of Re. Therefore, for our envisioned rough, angular icebergs, we select one value of C_D and hold it constant for the duration of each model run. Based on results from dimensionally similar experiments (e.g., *Aristoff et al.*, 2010; *Gaudet*, 1998; *Glasheen and McMahon*, 1996) and the knowledge that the drag for rough, irregularly-shaped icebergs is greater than that for idealized objects (*Hottovy and Sylvester*, 1979; *Goossens*, 1987), we test our model with $C_D = \{1, 2, 4\}$.

The $-U dm_a/dt$ term of eq. (2.3) is often regarded as a "slamming" force in the water-entry literature (*Miloh*, 1991; *De Backer et al.*, 2009) and is equivalent to mechanism (a). Particularly for blunt objects, this slamming force may be of very large magnitude but brief duration–typically on the order of several milliseconds. We prescribe a radial, hemispherical growth of m_a at the pressure wave velocity α for brackish seawater, 1470 m s^{-1}. For the short time interval while m_a grows to its full value (eq. (2.1)),

$$\frac{dm_a}{dt} = \rho_w 2\pi r^2 \frac{dr}{dt}, \tag{2.7}$$

where r is the instantaneous radius of added mass, i.e., the fluid entrained by the iceberg, and

$$m_a = \rho_w \frac{2}{3}\pi\alpha^3 t^3. \tag{2.8}$$

The expression for $\frac{dm_a}{dt}$ need not be exactly of the form of eq. (2.7); however, the large ratio of α/U ensures that the slamming force associated with momentum transfer from iceberg to water occurs over millisecond timescales as identified in studies with other objects (*Miloh*, 1991; *De Backer et al.*, 2009).

2.6.2.2 Model results and interpretation

The numerically integrated results of eq. (2.3) are presented in Figure 2.11. Approximately 2 s prior to impact ($t \sim -2$ s), an iceberg (H = 10 m, R = 8 m) detaches and begins free-fall from 20 m, impacting the fjord surface at t = 0 s. On impact, the net force on the iceberg abruptly switches from body-force-dominated, with negative net force, to slamming- and drag-force-dominated, with positive (upward directed) net force (Fig. 2.11a). Within 5 milliseconds, the slamming force associated with the entrainment of seawater peaks at 6000×10^6 N and the iceberg reaches a peak acceleration of 2500 m s^{-2}. Once m_a has reached its maximum value, the slamming force vanishes and the net force is dominated by the drag force; iceberg acceleration falls to 45 m s^{-2}. The net slamming impulse (equiv-

alent to the change in momentum) is given by

$$\int_0^{5\text{ ms}} U\frac{dm_a}{dt}dt = \Delta U m_a = 1.0 \times 10^{12}\text{ N s}, \tag{2.9}$$

and is roughly half that of the impulse imparted by the drag force,

$$\int_0^{\tau_d} F_D dt = 2.1 \times 10^{12}\text{ N s}, \tag{2.10}$$

where τ_d is the timescale over which the seismic source is expected to act, defined within the following paragraph. Slamming has the potential to act as a Lamb pulse on the water surface and contribute to the icequake signals recorded at our seismometers (e.g., *Kanamori and Given*, 1983). However the transmission of these waves will be hampered by water's inability to transmit shear waves and complicated by unquantifiable path effects. Thus, while acknowledging that slamming may contribute to our icequake signals, we focus the discussion on the longer duration evolution of the iceberg motion.

As the calved iceberg and entrained fluid ($m + m_a$) decelerate under the influence of drag, the drag force decreases (Eq. (2.5)). In the example presented here, the model results are truncated at 2.5 s because the choice of large, constant C_D becomes inappropriate at large t due to the C_D dependence on Re and Fr. As the iceberg approaches zero velocity at the nadir of its trajectory, the drag force decays towards zero. However, due to the gradual decay of F_D, we do not anticipate that the time to $F_D = 0$ is the relevant timescale for the seismic source. Instead, we select the deceleration timescale to be the e-folding time τ_d, i.e., the time by which F_D has fallen to $1/e$ of its maximum value. This definition of τ_d is somewhat arbitrary; however, the value of τ_d in this and other examples is fairly insensitive to its definition.

With τ_d as the approximate duration of the icequake source, $f_d \sim 1/2\tau_d$, where f_d is the icequake frequency measured by a seismometer (*Stein and Wysession*, 2003). In the case of Fig. 2.11, $f_d = 0.7$ Hz. Figure 2.12 illustrates the relationship between f_d, iceberg height and the drag coefficient. The icequake frequency depends on other parameters as well. If R is nearly doubled to 15 m, the resulting values of f_d decrease by approximately 50%. If the initial free-fall height of the iceberg is doubled from 20 m to 40 m, f_d increases by approximately 50%. For a wide variety of iceberg sizes and fall heights, we may expect that iceberg deceleration after impact has the potential to create seismic signals with frequencies between 0.5 and 2 Hz. These frequencies are slightly lower than we have observed at Yahtse Glacier, but given the simplicity of our model, they are remarkably close to the

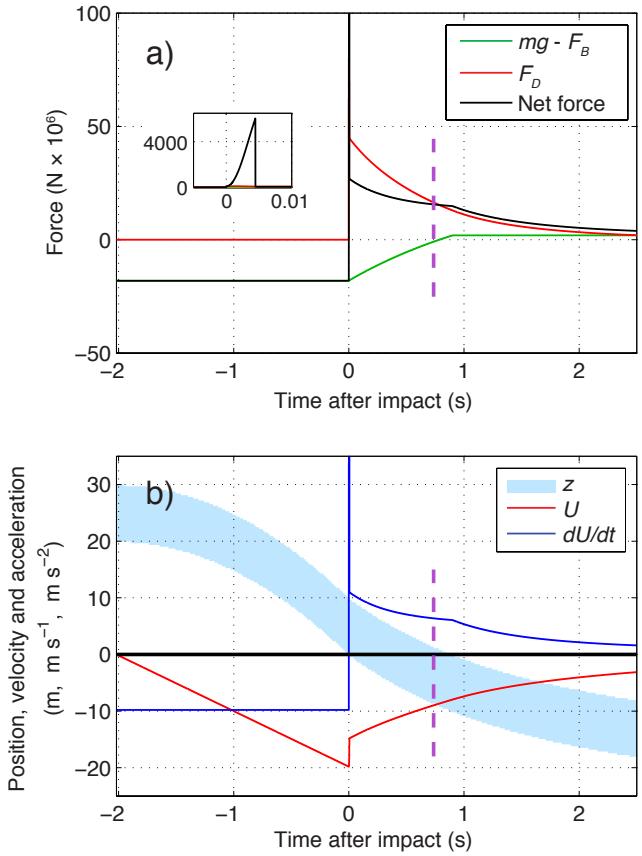

Figure 2.11. Results of the hydrodynamic model for a calved iceberg ($H = 10$ m, $R = 8$ m) falling into a fjord. (a) Total body force, drag force ($C_D = 2$), and sum of forces acting on the iceberg (right-hand side of eq. (2.3)). Inset shows the slamming force. Axes labels as in main plot. (b) Vertical position (z, shaded band), velocity and acceleration of the iceberg resulting from the forces of panel (a). Vertical, dashed, purple lines identify $\tau_d = 0.74$ s: that time by which *most* of the drag force has been imparted to the iceberg.

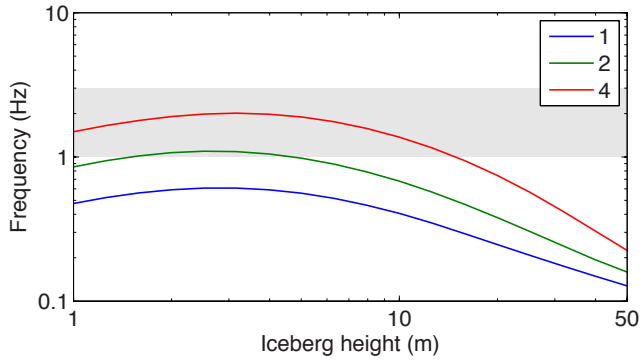

Figure 2.12. Dependence of the icequake frequency, f_d, on variables iceberg height, H, and a range of plausible drag coefficients $C_D = \{1, 2, 4\}$. $R = 8$ m and the iceberg free-fall height is 20 m for all cases. Gray shaded box identifies 1 Hz $\leq f_d \leq$ 3 Hz.

frequencies of observed calving icequakes. Iceberg deceleration is a potential explanation for the observed "steps" in the strength of low-frequency seismic amplitude that are associated with icebergs splashing and decelerating into the fjord.

In Fig. 2.11, cavitation begins at $t = 0.9$ s, after the top of the iceberg has descended below the sea surface. Although cavitation is not accounted for in the one-dimensional Eq. 2.3, we can apply a similar hydrodynamic analysis to the case of cavity wall collapse (mechanism (c)). Cavity collapse immediately precedes cavity pinch-off and the eruption of the Worthington jet (mechanism (d)) that coincides with peak amplitudes in calving icequakes. An air cavity formed after water impact in the lee of a descending object will pinch off at a location largely controlled by the value of Fr. In our cases, where surface tension may be neglected and the density of the object is approximately equal to the density of the fluid, $\frac{z_c}{R} \sim \mathrm{Fr}^{1/2}$, where z_c is the depth below the water surface at which the cavity first pinches off (*Gaudet*, 1998; *Gekle et al.*, 2008; *Bergmann et al.*, 2009).

The difference in potential energy between the surrounding water surface and the pinch-off depth of the fully open cavity, z_c, is approximately equal to the kinetic energy of the collapsing cavity walls at the moment of pinch-off:

$$V\rho_w g z_c \sim \frac{1}{2} V \rho_w \left(\frac{R}{\tau_c}\right)^2, \tag{2.11}$$

where V is the cavity volume and τ_c is the cavity collapse timescale. When we substitute for z_c, this reduces to

$$\tau_c \sim \sqrt{\frac{R}{2g\mathrm{Fr}^{1/2}}}. \tag{2.12}$$

If we apply the particular parameters and geometric values used in Fig. 2.11 again, then $\tau_c \sim 0.43$ s. As above, we define an icequake frequency $f_c \sim 1/2\tau_c$, so the icequake frequency we would expect from this cavity collapse is 1.2 Hz. This value is again within the range of peak frequencies observed for calving icequakes at Yahtse Glacier.

Our deceleration model result is consistent with observations from Jakobshavn Isbræ, where the terminus height is approximately 100 m—taller than the 40–80 m termini common at Alaskan Glaciers (*Brown et al.*, 1982; *Walter et al.*, 2012). At Jakobshavn Isbræ, *Amundson et al.* (2010) report icequakes with emergent onsets, 4–6 Hz dominant frequencies, 5–300 s durations, and associations with rumbling acoustic signals (their "Type 2" seismic signals). The appearance of their example waveform, with higher frequency ground motion early in the icequake arrival, is remarkably similar to the calving icequakes

we observe at Yahtse Glacier. *Amundson et al.* (2010) attribute these icequakes to avalanching of debris from the terminus and from icebergs in the fjord rotating and crashing onto dense ice debris mélange. However, the slamming (a) and iceberg deceleration (b) mechanisms are also potential icequake sources in a mélange-choked fjord. As stated above, our model of iceberg deceleration predicts higher frequency seismic signals for larger fall heights. Thus, if some of the type 2 icequakes of *Amundson et al.* (2010) are the product of iceberg calving, iceberg deceleration offers an explanation for why their 4-6 Hz dominant frequencies are slightly higher than the 1-3 Hz frequencies reported at Alaskan glaciers (e.g., *O'Neel et al.*, 2007).

To summarize, both iceberg deceleration (mechanism (b)) and cavity collapse (mechanism (c)) involve forces that act over timescales similar to those we would expect given the observed 1 – 5 Hz seismic signals described above. This modeling result corroborates the observations reported earlier and increases our confidence that we have identified the correct seismogenic mechanisms. Iceberg slamming (mechanism (a)) and cavity pinch-off (mechanism (d)) can involve forces far greater than those associated with deceleration and cavity collapse, but act over millisecond timescales and, in the case of slamming, generate a smaller impulse. While we have not explored mechanisms (a) and (d) explicitly, the interaction between brief, high-frequency pressure waves traveling through the water and the surrounding geologic structure may also be compatible with the generation of seismic signals within the 1 – 5 Hz band identified at Yahtse Glacier and elsewhere.

2.6.3 Seismic monitoring of iceberg calving

This and previous studies have demonstrated that iceberg calving generates significant seismic energy. However, the use of seismology as a tool to remotely monitor iceberg calving discharge has been hampered by two factors: uncertainty associated with source mechanisms, and the inability to form broadly applicable relationships between iceberg discharge and seismic parameters. We are able to contribute to this development through comparison of calving style and calving seismicity between Yahtse Glacier and nearby Columbia Glacier.

Studies at Columbia Glacier have found no correlation between peak icequake amplitude and the size of calving events (*Qamar*, 1988; *O'Neel et al.*, 2007). However, *O'Neel et al.* (2007) successfully used icequake recordings to estimate the rate of terminus retreat at Columbia Glacier. Their approach relied on a calibrated icequake duration metric and

an assumption that changes in the rate of terminus retreat are independent of changes in ice velocity. This metric was strongly modulated by relatively infrequent, very large, long-duration (100's s) calving events that involved submarine iceberg discharge.

The importance of calving style on calving seismicity was also manifest at Columbia Glacier during the summer of 2007, when the glacier terminus transitioned from grounded to floating (*Walter et al.*, 2010). Coincident with that grounded to floating transition was a shift in calving style from frequent, small, energetic calving events (similar to, but bigger than Yahtse Glacier events) to infrequent, larger, less energetic calving events. Calving from the post-2007 floating terminus was characterized by rift propagation leading to the release of tabular icebergs. Accompanying this shift in calving style was a dramatic decrease in the amplitude and occurrence rate of seismic signals between 1 and 5 Hz. *Walter et al.* (2010) found their pre-2007 observations consistent with a hydraulic fracturing source for calving under grounded conditions (see also *O'Neel and Pfeffer*, 2007). They suggested that when the terminus became afloat, hydraulic fracturing no longer took place at the terminus, altering both the icequake source and the style of calving.

Our result that calved iceberg volume is not proportional to seismic amplitude is consistent with the Columbia Glacier observations (*Qamar*, 1988; *O'Neel et al.*, 2007). We observed that iceberg free falls that result in cavitation produce high-amplitude seismograms irrespective of their size. At Yahtse Glacier, simple, 5 s, size 1 calving events produce icequakes detectable at least 13 km from the terminus, and, as demonstrated by the contrasting sizes and peak amplitudes of Block and Flake (Figs. 2.5 and 2.6), seismic amplitude is not a function of iceberg size. Larger icebergs with short free falls or that detach below the sea surface in the shallow waters of Icy Bay do not move fast enough to form an air cavity in their lee. Forces leading to deceleration will be weaker, and the lack of cavitation results in small peak seismic amplitudes for long event durations.

While hydraulic fracturing might be important in driving some calving events, the present study leads us to favor an alternate explanation for the change in calving seismicity reported at Columbia Glacier in 2007. Consistent with the calving observations reported by *Walter et al.* (2010), we suggest that glaciers with floating termini more rarely calve the types of icebergs that cavitate or create large splashes and powerful deceleration forces. Because the thinner, neutrally-buoyant post-2007 terminus of Columbia Glacier had less gravitational potential energy, interactions between icebergs and the sea surface were less forceful than from its grounded terminus, and 1–5 Hz calving seismicity is less

pronounced.

Our study, and the findings from *Walter et al.* (2010), suggest some caution in the use of 1–5 Hz icequakes for the purpose of studying calving at rapidly changing glaciers with diverse terminus geometries. The generation of icequakes with peak frequencies in this band is substantially dependent on the style of calving, the height of the terminal cliff and the depth of the fjord. For example, if the terminus of Yahtse Glacier were to thin, retreat, and eventually switch from grounded to floating, icebergs would detach closer to the waterline (as occurred at Columbia Glacier in 2007). As a result, we would expect that icequake peak frequencies and amplitudes would decrease. Within the limited range of observed terminal cliff heights and iceberg sizes, our numerical model indicates that the peak frequency of calving icequakes should be similar, regardless of whether the calving was subaerial or submarine. Deviations in the peak frequency or seismic amplitude of calving icequakes from a particular tidewater glacier can be expected to indicate a change in terminus geometry and/or calving style, as *Walter et al.* (2010) demonstrated.

With these caveats, future studies that aim to model calving flux from seismic parameters should continue to explore empirical relationships between icequake duration and amplitude as well as other seismic parameters, such as pseudo-energy (integrated squared velocity), coda duration, etc. If probabilistic modeling is carried out in enough cases and in a diversity of glacierized settings (e.g., thick and thin glaciers, varying levels of ice fracture), then perhaps a general empirical model can be developed that will apply at least to temperate, grounded glaciers. We can expect that a different empirical model would be necessary for floating termini or different calving styles. The development and application of such a model could be a powerful tool for quantifying the mass balance of rapidly-changing tidewater glaciers.

2.7 Conclusions

The seismic wavefield at the terminus of Yahtse Glacier is dominated by icequakes generated by iceberg calving—at least 75% of locally recorded seismic events can be conclusively linked to calving. We observe a strong correlation between calving duration and icequake duration; the relationship between peak icequake amplitude and iceberg size appears to be weak at Yahtse Glacier.

Our paired seismograms and calving videos reveal that interactions between icebergs and the sea surface generate the strongest icequake signals (as illustrated in Fig. 2.1). Seis-

mic energy is produced during iceberg impact on the sea surface as well as several seconds after impact, during cavitation. Cavitation is recognized by the occurrence of Worthington jets, in which water and ice debris are thrown high above the fjord surface. During iceberg impact, when we see steps in the amplitudes of our locally-recorded seismograms, potential seismogenic mechanisms include momentum transfer from icebergs to sea water (Fig. 2.1a) and iceberg deceleration (Fig. 2.1b). Following iceberg impact and coincident with the generation of Worthington jets, we record the largest amplitude portions of each subaerial calving icequake. Air cavity collapse (Fig. 2.1c) and cavity pinch-off (Fig. 2.1d) are the potential seismogenic mechanisms at these times.

Our proposed mechanisms are consistent with the repeated observation that icebergs calved from below the sea surface (submarine calving events) are rarely associated with large amplitude icequakes at Yahtse Glacier. Previous explanations of calving seismicity cannot easily explain the weak submarine calving seismicity described in this study. Compared with observations from deep-water termini (e.g., *Motyka*, 1997), our results suggest that Yahtse Glacier's fjord is too shallow to allow sufficient upward velocity to bring rising submarine icebergs to a height equivalent to the calving face. At glaciers in deeper fjords, submarine calved icebergs have the potential to rise significantly above their neutrally buoyant position ("shooters" in *Motyka* (1997)). When these "shooters" descend, they have the same potential to experience strong drag forces and generate cavities as the subaerially calved icebergs that are most common at Yahtse Glacier.

In a numerical model of iceberg/fjord source mechanisms, we explored the duration of forces associated with both iceberg deceleration and cavity collapse. Both of these mechanisms act over timescales similar to the peak icequake frequencies we document, 1–5 Hz. The other mechanisms considered herein, momentum transfer from iceberg to seawater and cavity pinch-off, act over far shorter timescales and may be associated with smaller impulses. While we cannot discount contributions from other source mechanisms not delineated here, the combination of observations and modeling we have described implicate some iceberg-sea surface interactions as strong sources of tidewater glacier seismicity.

2.8 Acknowledgments

This study was made possible by the National Science Foundation, through grant EAR-0810313. Additional funding is from USGS Climate and Land Use Change Program and Dept. of the Interior Climate Science Center. Jeff Aristoff, Channon Price and Wendy

Zhang offered insight and enlightening conversation regarding hydrodynamics. Joshua Carmichael, Seth Moran, Victor Tsai, an anonymous reviewer, and our scientific editor, Jeremy Bassis, contributed thorough and constructive reviews. Justin Rich assisted with the preparation of Fig. 2.2. Sophie Gilbert illustrated Fig. 2.1. Expert air support was from pilots Tony Oney and Paul Claus. David Conner and Jared Steyaert assisted with the calving observer record. PASSCAL and UNAVCO provided seismic and geodetic instruments for this work. The Wrangell Mountains Center, McCarthy, AK, provided logistical assistance. The GISMO toolbox significantly facilitated the manipulation and plotting of seismic data (*Reyes and West*, 2011). We gratefully thank all of the people who contributed to help make this work happen.

References

Alaska Earthquake Information Center (2012), Monthly Earthquake Catalogs.

Amundson, J. M., M. Truffer, M. P. Lüthi, M. Fahnestock, M. West, and R. J. Motyka (2008), Glacier, fjord, and seismic response to recent large calving events, Jakobshavn Isbræ, Greenland, *Geophys. Res. Lett.*, *35*(22), 1–5, doi: 10.1029/2008GL035281.

Amundson, J. M., M. Fahnestock, M. Truffer, J. Brown, M. P. Lüthi, and R. J. Motyka (2010), Ice mélange dynamics and implications for terminus stability, Jakobshavn Isbræ, Greenland, *J. Geophys. Res.*, *115*(F1), 1–12, doi: 10.1029/2009JF001405.

Amundson, J. M., J. F. Clinton, M. Fahnestock, M. Truffer, M. P. Luthi, and R. J. Motyka (2012), Observing calving-generated ocean waves with coastal broadband, Jakobshavn Isbr\ae, Greenland, *Ann. Glaciol.*, *53*(60), 79–84, doi: 10.3189/2012/AoG60A200.

Aristoff, J., T. Truscott, A. Techet, and J. Bush (2010), The water entry of decelerating spheres, *Phys. Fluids*, *22*(3), 1–8, doi: 10.1063/1.3309454.

Barclay, D. J., J. L. Barclay, P. E. Calkin, and G. C. Wiles (2006), A Revised and Extended Holocene Glacial History of Icy Bay, Southern Alaska, U.S.A, *Arctic, Antarctic, and Alpine Research*, *38*(2), 153–162, doi: 10.1657/1523-0430(2006)38[153:ARAEHG]2.0.CO;2.

Bassis, J. N., R. Coleman, H. A. Fricker, and J. B. Minster (2005), Episodic propagation of a rift on the Amery Ice Shelf, East Antarctica, *Geophys. Res. Lett.*, *32*(L06502), 1–5, doi: 10.1029/2004GL022048.

Batchelor, G. (1967), *An Introduction to Fluid Dynamics*, 615 pp., Cambridge Univ. Press, Cambridge, U.K.

Bergmann, R., D. Van Der Meer, S. Gekle, A. Van Der Bos, and D. Lohse (2009), Controlled impact of a disk on a water surface: cavity dynamics, *Journal of Fluid Mechanics*, *633*, 381, doi: 10.1017/S0022112009006983.

Brown, C. S., M. F. Meier, and A. Post (1982), Calving speed of Alaska tidewater glaciers, with application to Columbia Glacier, *USGS Prof. Pap.*, *1258-C*, C1–C13.

Carmichael, J. D., E. C. Pettit, M. Hoffman, A. Fountain, and B. Hallet (2012), Seismic multiplet response triggered by melt at Blood Falls, Taylor Glacier, Antarctica, *J. Geophys. Res.*, *117*(F3), 1–16, doi: 10.1029/2011JF002221.

Chouet, B., G. Saccorotti, M. Martini, P. Dawson, G. D. Luca, G. Milana, and R. Scarpa (1997), Source and path effects in the wave fields of tremor and explosions at Stromboli Volcano, Italy, *J. Geophys. Res.*, *102*(B7), 15,129–15,150.

De Backer, G., M. Vantorre, C. Beels, J. De Pré, S. Victor, J. De Rouck, C. Blommaert, and W. Van Paepegem (2009), Experimental investigation of water impact on axisymmetric bodies, *Appl. Ocean Res.*, *31*(3), 143–156, doi: 10.1016/j.apor.2009.07.003.

Deichmann, N., J. Ansorge, F. Scherbaum, A. Aschwanden, F. Bernardi, and G. H. Gudmundsson (2000), Evidence for deep icequakes in an Alpine glacier, *Ann. Glaciol.*, *31*(1), 85–90, doi: 10.3189/172756400781820462.

Ekström, G., M. Nettles, and G. A. Abers (2003), Glacial earthquakes, *Science*, *302*(5645), 622–4, doi: 10.1126/science.1088057.

Gaudet, S. (1998), Numerical simulation of circular disks entering the free surface of a fluid, *Phys. Fluids*, *10*(10), 2489–2499, doi: 10.1063/1.869787.

Gekle, S., and J. M. Gordillo (2010), Generation and breakup of Worthington jets after cavity collapse. Part 1. Jet formation, *Journal of Fluid Mechanics*, *663*, 293–330, doi: 10.1017/S0022112010003526.

Gekle, S., A. van der Bos, R. Bergmann, D. van der Meer, and D. Lohse (2008), Noncontinuous Froude Number Scaling for the Closure Depth of a Cylindrical Cavity, *Physical Review Letters*, *100*(8), 1–4, doi: 10.1103/PhysRevLett.100.084502.

Glasheen, J. W., and T. A. McMahon (1996), Vertical water entry of disks at low Froude numbers, *Phys. Fluids*, *8*(8), 2078–2083, doi: 10.1063/1.869010.

Goossens, D. (1987), A drag coefficient equation for natural, irregularly shaped particles, *Catena*, *14*(1-3), 73–99, doi: 10.1016/S0341-8162(87)80007-3.

Hottovy, J. D., and N. D. Sylvester (1979), Drag coefficients for irregularly shaped particles, *Industrial & Engineering Chemistry Process Design and Development*, *18*(3), 433–436, doi: 10.1021/i260071a014.

Joughin, I., I. Howat, R. B. Alley, G. Ekstrom, M. Fahnestock, T. Moon, M. Nettles, M. Truffer, and V. Tsai (2008), Ice-front variation and tidewater behavior on Hel-

heim and Kangerdlugssuaq Glaciers, Greenland, *J. Geophys. Res.*, *113*(F1), 1–11, doi: 10.1029/2007JF000837.

Kanamori, H., and J. W. Given (1983), Lamb pulses observed in nature, *Geophys. Res. Lett.*, *10*(5), 373–379.

Kennett, B. L. N. (2002), *The Seismic Wavefield, Volume II: Interpretation of Seismograms on Regional and Global Scales*, 534 pp., Cambridge Univ. Press, Cambridge, U.K.

Korotkin, A. I. (2009), *Added masses of ship structures*, 401 pp., Springer.

May, A., and J. C. Woodhull (1948), Drag coefficients of steel spheres entering water vertically, *J. Appl. Phys.*, *19*, 1109–1121.

Meier, M. F., and A. Post (1987), Fast tidewater glaciers, *J. Geophys. Res.*, *92*(B9), 9051–9058.

Métaxian, J.-P. (2003), Seismicity related to the glacier of Cotopaxi Volcano, Ecuador, *Geophys. Res. Lett.*, *30*(9), 3–6, doi: 10.1029/2002GL016773.

Miloh, T. (1991), On the initial-stage slamming of a rigid sphere in a vertical water entry, *Appl. Ocean Res.*, *13*(1), 43–48.

Motyka, R. J. (1997), Deep-water calving at LeConte Glacier, southeast Alaska, *Byrd Polar Res. Center Rep.*, *15*, 115–118.

Muskett, R. R., C. S. Lingle, J. M. Sauber, B. T. Rabus, and W. V. Tangborn (2008), Acceleration of surface lowering on the tidewater glaciers of Icy Bay, Alaska, U.S.A. from InSAR DEMs and ICESat altimetry, *Earth and Planetary Science Letters*, *265*(3-4), 345–359, doi: 10.1016/j.epsl.2007.10.012.

Neave, K. G., and J. C. Savage (1970), Icequakes on the Athabasca Glacier, *J. Geophys. Res.*, *75*(8), 1351–1362, doi: 10.1029/JB075i008p01351.

Nettles, M., and G. Ekström (2010), Glacial earthquakes in Greenland and Antarctica, *Annual Review of Earth and Planetary Sciences*, *38*(1), 467–491, doi: 10.1146/annurev-earth-040809-152414.

O'Neel, S., and W. T. Pfeffer (2007), Source mechanics for monochromatic icequakes produced during iceberg calving at Columbia Glacier, AK, *Geophys. Res. Lett.*, *34*(22), 1–5, doi: 10.1029/2007GL031370.

O'Neel, S., K. A. Echelmeyer, and R. J. Motyka (2003), Short-term variations in calving of a tidewater glacier: LeConte Glacier, Alaska, U.S.A., *J. Glaciol.*, *49*(167), 587–598, doi: 10.3189/172756503781830430.

O'Neel, S., H. Marshall, D. McNamara, and W. T. Pfeffer (2007), Seismic detection and analysis of icequakes at Columbia Glacier, Alaska, *J. Geophys. Res.*, *112*(F3), 1–14, doi: 10.1029/2006JF000595.

O'Neel, S., C. F. Larsen, N. Rupert, and R. Hansen (2010), Iceberg calving as a primary source of regional-scale glacier-generated seismicity in the St. Elias Mountains, Alaska, *J. Geophys. Res.*, *115*(F4), 1–12, doi: 10.1029/2009JF001598.

Porter, S. C. (1989), Late Holocene Fluctuations of the Fiord Glacier System in Icy Bay, Alaska, U.S.A., *Arctic Alp. Res.*, *21*(4), 364, doi: 10.2307/1551646.

Qamar, A. (1988), Calving icebergs: a source of low-frequency seismic signals from Columbia Glacier, Alaska, *J. Geophys. Res.*, *93*(B6), 6615–6623.

Reyes, C. G., and M. E. West (2011), The Waveform Suite: A Robust Platform for Manipulating Waveforms in MATLAB, *Seismological Research Letters*, *82*(1), 104–110, doi: 10.1785/gssrl.

Sabunco, T., and S. Calisal (1981), Hydrodynamic coefficients for vertical circular cylinders at finite depth, *Ocean Engng.*, *8*, 25–63.

Spray, J. G. (1999), Shocking rocks by cavitation and bubble implosion, *Geology*, *27*(8), 695–698.

St. Lawrence, W., and A. Qamar (1979), Hydraulic transients: a seismic source in volcanoes and glaciers., *Science*, *203*(4381), 654–6, doi: 10.1126/science.203.4381.654.

Stein, S., and M. Wysession (2003), *An Introduction to Seismology, Earthquakes, and Earth Structure*, 498 pp., Blackwell Publishing, Malden, MA, USA.

Tsai, V., and G. Ekström (2007), Analysis of glacial earthquakes, *J. Geophys. Res.*, *112*(F3), 1–13, doi: 10.1029/2006JF000596.

Tsai, V., J. Rice, and M. Fahnestock (2008), Possible mechanisms for glacial earthquakes, *J. Geophys. Res.*, *113*(F03014), 1–17, doi: 10.1029/2007JF000944.

van der Veen, C. J. (1996), Tidewater calving, *J. Glaciol.*, *42*(141), 375–385.

Walter, F., N. Deichmann, and M. Funk (2008), Basal icequakes during changing subglacial water pressures beneath Gornergletscher, Switzerland, *J. Glaciol.*, *54*(186), 511–521, doi: 10.3189/002214308785837110.

Walter, F., J. F. Clinton, N. Deichmann, D. S. Dreger, S. E. Minson, and M. Funk (2009), Moment Tensor Inversions of Icequakes on Gornergletscher, Switzerland, *Bulletin of the Seismological Society of America*, *99*(2A), 852–870, doi: 10.1785/0120080110.

Walter, F., S. O'Neel, D. McNamara, W. T. Pfeffer, J. Bassis, and H. Fricker (2010), Iceberg calving during transition from grounded to floating ice: Columbia Glacier, Alaska, *Geophys. Res. Lett.*, *37*(15), 1–5, doi: 10.1029/2010GL043201.

Walter, F., J. M. Amundson, S. O'Neel, M. Truffer, M. Fahnestock, and H. a. Fricker (2012), Analysis of low-frequency seismic signals generated during a multiple-iceberg calving event at Jakobshavn Isbræ, Greenland, *J. Geophys. Res.*, *117*(F1), 1–11, doi: 10.1029/2011JF002132.

Welty, E. Z., T. C. Bartholomaus, S. O'Neel, and W. T. Pfeffer (2013), Cameras as clocks, *J. Glaciol.*, *59*(214), 275–286, doi: 10.3189/2013JoG12J126.

West, M., C. Larsen, M. Truffer, S. O'Neel, and L. LeBlanc (2010), Glacier microseismicity, *Geology*, *38*(4), 319–322, doi: 10.1130/G30606.1.

Whipple, K. X., G. S. Hancock, and R. S. Anderson (2000), River incision into bedrock : Mechanics and relative efficacy of plucking , abrasion , and cavitation, *Geol. Soc. Amer. Bull.*, *112*(3), 490–503.

Wiens, D. A., S. Anandakrishnan, J. P. Winberry, and M. A. King (2008), Simultaneous teleseismic and geodetic observations of the stick-slip motion of an Antarctic ice stream., *Nature*, *453*(7196), 770–4, doi: 10.1038/nature06990.

Winberry, J. P., S. Anandakrishnan, and R. B. Alley (2009), Seismic observations of transient subglacial water-flow beneath MacAyeal Ice Stream, West Antarctica, *Geophys. Res. Lett.*, *36*(L11502), 1–5, doi: 10.1029/2009GL037730.

Winberry, J. P., S. Anandakrishnan, D. A. Wiens, R. B. Alley, and K. Christianson (2011), Dynamics of stickâĂŞslip motion, Whillans Ice Stream, Antarctica, *Earth and Planetary Science Letters*, *305*(3-4), 283–289, doi: 10.1016/j.epsl.2011.02.052.

Wolf, L. W., and J. N. Davies (1986), Glacier-generated earthquakes from Prince William Sound, Alaska, *Bull. Seismol. Soc. Am.*, *76*(2), 367–379.

Chapter 3

Does calving matter? Evidence for significant submarine melt[1]

3.1 Abstract

During the summer in the northeast Pacific Ocean, the Alaska Coastal Current sweeps water with temperatures in excess of 12 °C past the mouths of glacierized fjords and bays. The extent to which these warm waters affect the mass balance of Alaskan tidewater glaciers is uncertain. Here we report hydrographic measurements made within Icy Bay, Alaska, and calculate rates of submarine melt at Yahtse Glacier, a tidewater glacier terminating in Icy Bay. We find strongly stratified water properties consistent with estuarine circulation and evidence that warm Gulf of Alaska water reaches the head of 40 km-long Icy Bay, largely unaltered. A 10 - 20 m layer of cold, fresh, glacially-modified water overlies warm, saline water. The saline water is observed to reach up to 10.4 °C within 1.5 km of the terminus of Yahtse Glacier. By quantifying the heat and salt deficit within the glacially-modified water, we place bounds on the rate of submarine melt. The submarine melt rate is estimated at > 9 m d^{-1}, at least half the rate at which ice flows into the terminus region, and can plausibly account for all of the submarine terminus mass loss. Our measurements suggest that summer and fall subaerial calving is a direct response to thermal undercutting of the terminus, further demonstrating the critical role of the ocean in modulating tidewater glacier dynamics.

3.2 Introduction

Marine-terminating glaciers worldwide are undergoing rapid changes (e.g., *Larsen et al.*, 2007; *Pritchard et al.*, 2009). In many cases, rapid mass changes of tidewater glaciers are controlled by processes acting at the terminus (*Nick et al.*, 2009). Changes in glacier terminus position dL/dt result from differences in the ice flux to the terminus Q_i and ice flux from the terminus,

$$\frac{dL}{dt} = \frac{Q_i - Q_a}{A} \tag{3.1}$$

where Q_a is the frontal ablation rate (i.e., rate of ice loss from the glacier terminus, *Cogley et al.* (2011)), and A is the cross sectional area of the terminus. The terminus ice flux $Q_i = u_i A$, where u_i is the terminus-averaged ice velocity. Ice melt (both above and below the water line) and iceberg calving contribute to the frontal ablation rate. In accordance with

[1]Published as Bartholomaus, T. C., C. F. Larsen, and S. O'Neel (2013), Does calving matter? Evidence for significant submarine melt, *Earth Planet. Sci. Lett.*, *380*, 21–30.

previous studies in Alaska that found submarine melt rates 100-fold greater than subaerial melt rates (*Walters et al.*, 1988; *Motyka et al.*, 2003), we disregard subaerial frontal melt. The flux of ice lost to submarine melt Q_m is

$$Q_m = \dot{m} A_w, \tag{3.2}$$

where $\dot{m}$ is the terminus-averaged submarine melt rate, and A_w is the submarine portion of the terminus cross section A, and similarly, the calving flux Q_c is

$$Q_c = \dot{c} A, \tag{3.3}$$

where $\dot{c}$ is the terminus-averaged calving rate. Grounded tidewater glaciers such as Yahtse Glacier are unable to support significantly overhanging termini (*O'Leary and Christoffersen*, 2013), so, in essence,

$$dL/dt = u_i - \dot{c} - \dot{m}, \tag{3.4}$$

and where $dL/dt \ll u_i$, as is frequently the case (*van der Veen*, 2002),

$$u_i \sim \dot{c} + \dot{m}. \tag{3.5}$$

While, in many tidewater systems, the components of Eq. 3.4 are clearly changing, the calving and submarine melt processes are poorly understood and their rates are difficult to measure. Quantifying the magnitude of the submarine melt rate, and therefore the relative size of $\dot{m}$ and $\dot{c}$, at Yahtse Glacier, Alaska, is the goal of this study.

Theoretical and modeling studies have found that the submarine melt rate at a glacier terminus is dependent on subglacial discharge and ambient seawater temperature, such that

$$\dot{m} \propto q^p \Theta_s, \tag{3.6}$$

where q is the flux of subglacial discharge per terminus length, p is a parameter, and Θ_s is the ambient seawater temperature (*Jenkins*, 2011; *Xu et al.*, 2012; *Sciascia et al.*, 2013). Both *Jenkins* (2011) and *Xu et al.* (2012) found $p = 1/3$, whereas $p = 1/2$ better fit the modeling results of *Sciascia et al.* (2013).

Several authors have attributed rapid geometry changes observed at tidewater glacier termini in Alaska and Greenland to submarine melt (e.g., *Motyka et al.*, 2003; *Ritchie et al.*, 2008; *Nick et al.*, 2009; *Seale et al.*, 2011). In Alaska, several studies have demonstrated that warm (> 7 °C) water can reach within 2-3 km of tidewater glacier termini (*Matthews*, 1981;

Walters et al., 1988; *Motyka et al.*, 2003). Submarine melt rates across Alaska are poorly resolved, but have been shown to reach up to 12 m d^{-1} averaged across submarine termini (*Walters et al.*, 1988; *Motyka et al.*, 2003). However, despite these observations, substantial uncertainty persists regarding the temporal and spatial extent over which submarine ice melt is important, the upper bound of $\dot{m}$, and the interplay within glacierized fjords between subglacial discharge, submarine melt, and continental shelf seawater.

Herein, we present observations and model results of submarine melt at Yahtse Glacier and Icy Bay, located along the Gulf of Alaska coast, based upon 123 conductivity-temperature-depth (CTD) casts made during Julys in 2009–2011. These hydrographic measurements reveal a 10–20 m thick, surface layer of glacially-modified water and allow us to infer the near-terminus fjord circulation. Adjacent to the terminus of Yahtse Glacier, we draw on observations of water temperature and salinity to identify the amount of submarine glacier melt, subglacial discharge and ambient seawater present within the glacially-modified water. To quantify the flux of these waters, and therefore $\dot{m}$, we estimate the near-surface currents with a variety of local observations. Finally, we place our summertime estimate into longer, seasonal, annual and multi-decadal contexts.

3.3 Field Site

Icy Bay is a 40-km-long indentation on the Gulf of Alaska coast (Fig. 3.1). During the summer, the Alaska Coastal Current (ACC) sweeps warm (> 12 °C) near-surface water north and west along Alaska's continental shelf, past the mouth of Icy Bay (*Stabeno et al.*, 2004; *Weingartner et al.*, 2005). This approximately 20-25 km-wide baroclinic current is driven in large part by fresh water delivery along the coast. Since much of this fresh water is glacier runoff (*Neal et al.*, 2010), the influence of glaciers on the current is unquestioned (*Weingartner et al.*, 2005; *Royer and Grosch*, 2006). However, the reciprocal relationship, the current's influence on glaciers, is poorly understood despite the current's potential to impose a significant melt forcing on the termini of all tidewater glaciers surrounding the Gulf of Alaska.

Icy Bay was entirely occupied by glaciers flowing out of the St. Elias Range during the mid-19th century (Fig. 3.1) (*Porter*, 1989; *Barclay et al.*, 2006). Near the end of the 19th century, the coalesced tidewater Icy Bay glaciers began a 100 yr retreat from its Little Ice Age (LIA) maximum at an average rate of 400 m yr^{-1}. This retreat culminated in the division of the Icy Bay glaciers into several distinct, formerly tributary glaciers, of which Yahtse

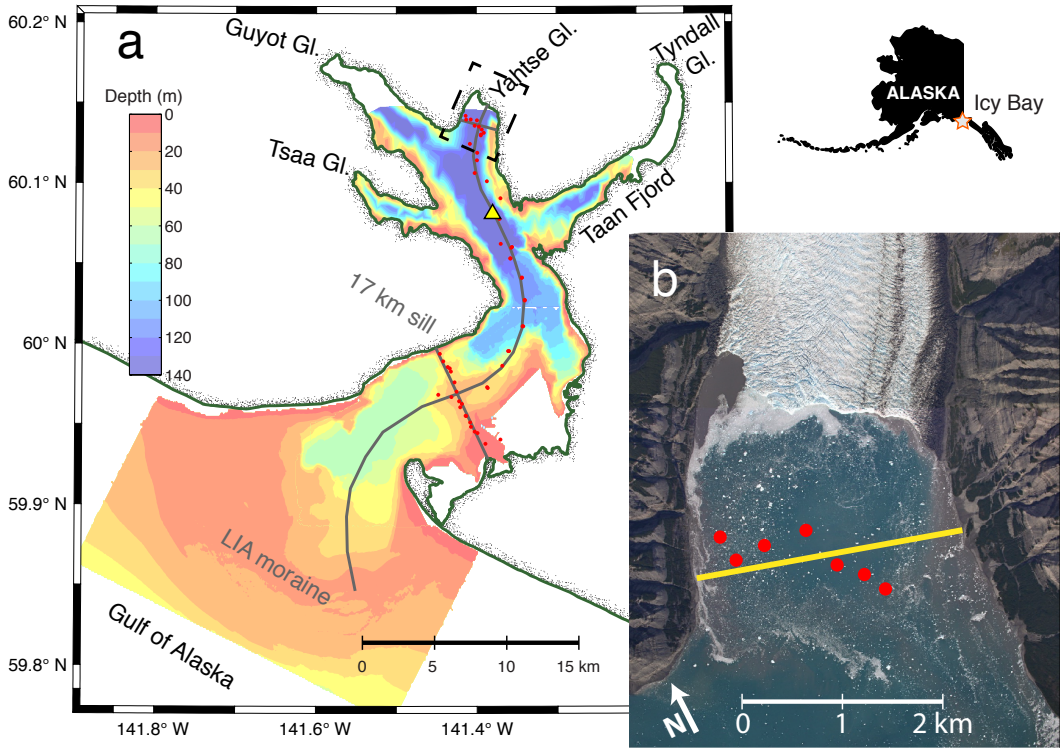

Figure 3.1. Map of Icy Bay and the terminus of Yahtse Glacier. (a) Icy Bay with 10 m bathymetric filled contours. The shoreline is identified in green and two shallow sills are labeled. The locations of CTD casts made in 2011 are shown as small red circles. The locations of cross section profiles (Figs. 3.3 and Appendix 3.A) are shown in gray. The 2011 termini of four glaciers are identified. The area of panel (b) is enclosed within the dashed black rectangle. The location of the casts presented in Fig. 3.2 is marked with a yellow triangle. (b) Aerial photograph of the terminus of Yahtse Glacier (12 Sept. 2011), the locations of the 7 CTD casts presented in Figs. 3.3 and 3.4 (29 July 2011), and the fjord-perpendicular profile onto which these casts are projected. The persistent subglacial discharge plume is apparent on the NW side of the terminus. During late July 2011, it extended to include the location of the 2 western-most casts.

Glacier has the largest area (1020 km^2 in 2000). Yahtse Glacier reached its most retracted position in approximately 1990, after which it began a 2 km re-advance that continues today. Since 2009, we have observed a spring advance and fall retreat (approximately 300 m range) superimposed on the multi-year advance (*Bartholomaus et al.*, 2012).

Icy Bay is separated from the Gulf of Alaska by a submarine terminal moraine at the location of the LIA maximum; the maximum depth across the crest of this moraine/sill is 17 m. Inland by 17 km of the LIA maximum sill is a second, intermediate sill with a maximum depth of 35 m. The retreat of the Icy Bay glacier paused here between 1916 and 1926 (*Porter*, 1989). In 1981, as Yahtse Glacier was approaching its most receded position, the greatest depths within Icy Bay ($\sim$ 185 m) were found within the narrow Yahtse Glacier fjord (*Post*, 1983). Most of the bathymetry in Fig. 3.1a was collected between 2000 and 2008 by the U.S. National Oceanic and Atmospheric Administration (NOAA) (www.ngdc.noaa.gov/mgg/bathymetry/$\sim$relief.html). Near the glacier termini, where multibeam data are unavailable, we contour the 1981 soundings (*Post*, 1983, and NOAA Icy Bay nautical chart 16741). Soundings reported in this study reveal shallowing by more than 50 m near the Yahtse Glacier terminus; thus, these near-terminus depths are uncertain (section 3.5).

Tides have been recorded within 3 km of the mouth of Taan Fjord. There, the difference between Mean Higher High Water and Mean Lower Low Water is 2.9 m (http://tidesandcurrents.noaa.gov, Tidal station 9453431).

3.4 Data collection and processing

During late July of 2009, 2010 and 2011, we made respectively 6, 55 and 62 CTD casts to characterize the hydrography within Icy Bay. Each year, we collected data with a Sea-Bird Electronics (SBE) 19 profiler. In 2011, an SBE 19plus additionally recorded turbidity, pH, and dissolved oxygen. The manufacturer-provided accuracies for these instruments are < 0.01 °C, < 0.01 g kg^{-1}, and < 1.7 dbar. Instruments were calibrated prior to use each year. Casts were made along three profiles: one profile along the axis of Icy Bay and two perpendicular transects (Fig. 3.1). The 2011 casts provide the best spatial coverage of Icy Bay and are the focus of this study. For plotting and analysis, water properties from each cast are averaged at 1 m intervals. To construct cross sections of water properties, we project casts onto the profiles by translating them up to 0.5 km and linearly interpolating between measurements.

We place our CTD casts within a broader geographic and temporal context by drawing on measurements from GAK1, an oceanographic station within the ACC, 450 km west of Icy Bay (*Weingartner et al.*, 2005). In particular, we choose to use water properties collected at 20 m depth, the shallowest moored measurements. Other depths reveal water property variations with similar temporal structure to those at 20 m depth. For all analyses, we present water properties as conservative temperatures Θ and absolute salinities S_A, in accordance with the International Thermodynamic Equation of Seawater - 2010 (TEOS-10) (*IOC et al.*, 2010).

A time lapse camera looking south above Icy Bay allows us to characterize near-surface water currents by the influence they exert on icebergs, as well as the rates of ice flow near the terminus. For 11 days during time lapse camera operation, we used an auto-theodolite to survey the position of prisms placed on a serac 1 km from the glacier terminus. We extend this surveyed record of daily glacier speeds by cross-correlating time lapse images (following *Scambos et al.*, 1992) and extracting the pixel offsets for the region where the prisms were placed. Linear regression of surveyed speed onto pixel offset enables us to identify glacier terminus speeds during our hydrographic survey, when surveyed serac positions are unavailable.

3.5 Icy Bay hydrography and sedimentation

The water properties within Icy Bay were similar during each of the three years and can be considered a two-layer system (Fig. 3.2a-c). Water above 10 - 20 m depth is cold (1 - 5 °C) and relatively fresh (< 25 g kg^{-1}). The deeper water is warmer (> 6 °C) and has a near-uniform, high salinity. Both the temperature and salinity are typical of the ACC during the months preceding our measurements (Fig. 3.2d and *Weingartner et al.*, 2005). At the bottom of Icy Bay, we find cool, saline water similar to the ACC during winter and spring. The warming and freshening as one moves up within the water column is consistent with the warming and freshening of the ACC through the early summer. The relatively low density of this early summer ACC water is sufficient to prevent its displacing the cooler winter water at the bottom of Icy Bay.

Vertical stratification of water within the fjord is quantified by the square of the Brunt-Väisälä frequency N,

$$N^2 = -\frac{g}{\rho}\frac{d\rho}{dz}, \tag{3.7}$$

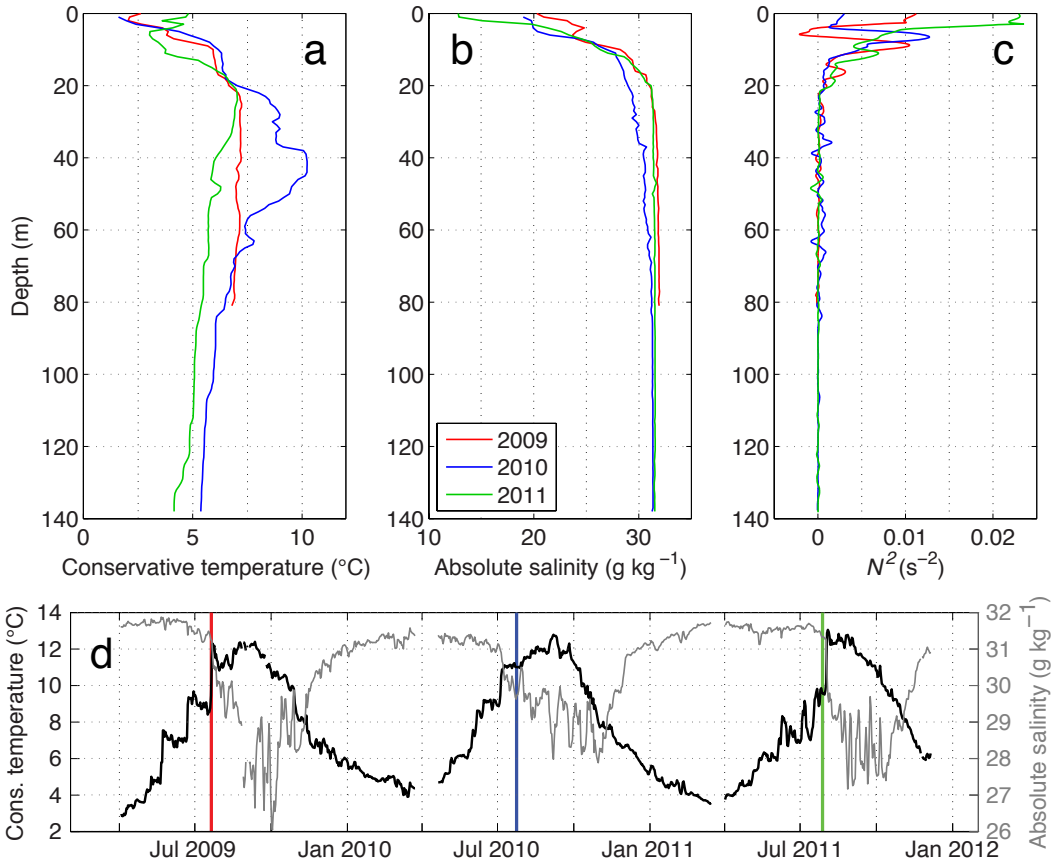

Figure 3.2. Three years of hydrographic data from Icy Bay and the Gulf of Alaska. (a-c) Representative late-July casts from 3 consecutive years at a location between Tsaa and Taan fjords, 33 km from the LIA maximum and 8 km from the Yahtse terminus. (d) Daily-averaged, 20-m-depth conservative temperature and absolute salinity at station GAK1, a location within the ACC 450 km west of Icy Bay. Vertical, colored lines identify the times of each of the three casts in panels (a-c).

where ρ is water density, g is gravitational acceleration, and z is height above sea level. Negative N^2 values indicate buoyantly unstable water volumes; increasing values of N^2 indicate increasing stability. In order to minimize small-scale instabilities, we have smoothed N^2 in all figures with a 5 m moving average. The boundary between the cold surface and warm sub-surface layer is shown in Fig. 3.2c by local maxima in N^2 in 2009, 2010, and 2011 at 8.8, 6.5, and 11.0 m, respectively.

Horizontal variability of water properties is far less than in the vertical; the same two layers presented within Fig. 3.2 can be traced throughout Icy Bay (see Appendix 3.A). Isohalines are nearly horizontal and salinity is nearly constant at depths greater than 20 m in 2009 and 2011. Temperatures within the deep layer are 1 - 2 °C cooler at a given depth near the Yahtse terminus than they are 15 km farther from the terminus. At the 17 km intermediate sill, we recorded our highest water temperatures, 12 °C in 2011. We suggest that this indicates water entering upper Icy Bay from the Gulf of Alaska.

Along a line approximately 1.5 km from the terminus of Yahtse Glacier, a set of casts made on 29 July 2011 reveal water properties consistent with the broader patterns described above (Fig. 3.3). This profile was begun at a high tide and was completed in 2.4 hrs, during which time the tide fell approximately 0.8 m. Absolute salinity increases with depth from a minimum of 17 g kg^{-1} at the surface to 30 g kg^{-1} at 20 m, then increases more slowly to a uniform 31.5 g kg^{-1} at 60 m (Fig. 3.3a). A sharp thermocline is present between 15 and 20 m depth, below which the water temperature rises to 7 °C, then gradually decreases with depth (Fig. 3.3b). In 2010, when a single CTD cast was made mid-fjord at this location, we found structure similar to that shown in Fig. 3.2 for that year, with 10.4 °C water at 38 m depth.

The turbidity signal in 2011 is dominated by the presence of the persistent 2011 subglacial discharge plume on the northwest side of the fjord (Fig. 3.3c). The edge of the plume was sharp while we made our casts, with an abrupt change from blue-green water and a dense iceberg cover outside the plume to brown, rapidly flowing water free of icebergs within the plume. Water sampled within this plume exceeded the range of the turbidimeter ($>$ 128 Nephelometric Turbidity Units (NTU)). Below the plume (approximately 10 m depth) the turbidity fell quickly to background levels ($\sim$ 10 NTU). Several less-pronounced lenses of turbid water were also identified, the greatest of which was between 65 and 85 m depth near the center of the fjord. This deep turbidity plume is associated with a weak, negative salinity anomaly. Dissolved oxygen and pH were highest near the surface (Fig.

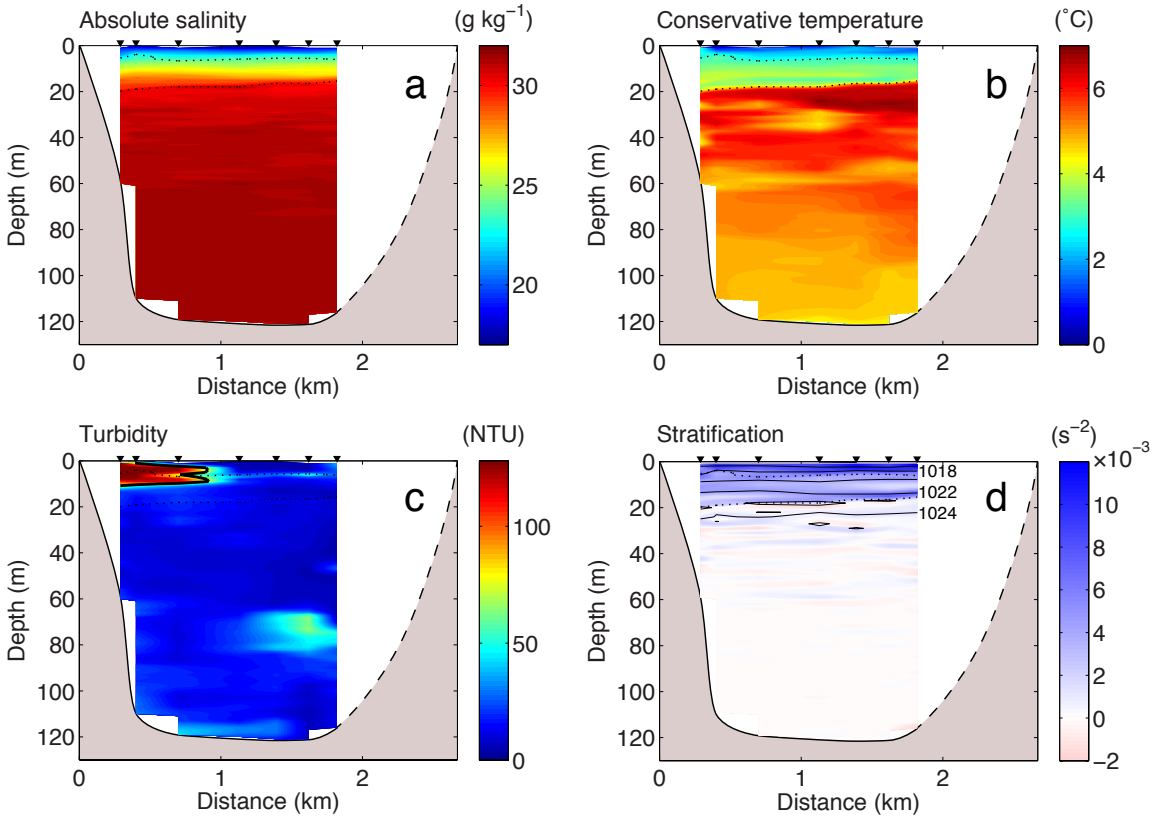

Figure 3.3. Water properties in the near-terminus cross section. The location of the fjord-perpendicular, 29 July 2011, cross section is shown in Fig. 3.1. View is looking up-fjord, toward Yahtse Glacier. (a) absolute salinity, (b) conservative temperature, (c) turbidity, and (d) N^2 shown by the colorbar, overlain by black density contours (contour interval is 2 kg m^{-3}; several densities are labeled). Triangles at the top of each profile identify the locations of casts. In each panel, the 3 and 5 °C contours are dotted to aid comparison between panels. In (c), the black line highlights the 70 NTU contour, which we assume represents the bounds of the swift-flowing current out away from glacier terminus (see end of section 3.7). Fjord bottom identified by CTD casts is shown, dashed where inferred.

3.A.1), with the relatively high dissolved oxygen concentrations (~ 6.5 mL L^{-1}) at depth suggestive of renewal at subannual timescales (Fig. 3.A.1 and *Muench and Heggie*, 1978).

Stratification is high in the shallow layers where salinity changes rapidly, then falls off abruptly at the thermocline between 15 and 18 m, at approximately the 1024 kg m^{-3} isopycnal (Fig. 3.3f). However, smaller instabilities with $-1.5 \times 10^{-3} \lesssim N^2 \lesssim -0.5 \times 10^{-3}$ are present across the fjord down to a depth of 60 - 65 m. Below 65 m, the near-terminus water is less unstable, with $N^2 > -0.3 \times 10^{-3}$.

As all of the CTD casts in Fig. 3.3 reached the sea floor, we can compare their depths with soundings made in 1981, approximately 3 yrs after the terminus of Yahtse Glacier retreated through this part of the fjord (*Post*, 1983; *Porter*, 1989). Thirty years prior to our casts, the fjord bottom at our cross section was sounded between 173.4 and 181.4 m. Our casts, corrected to the same datum, are 118.9 m deep. This implies sedimentation rates ranging from 1.82 to 2.08 m yr^{-1} at a mean distance of approximately 2.5 km from the glacier terminus. These sedimentation rates are within the ranges of previous near-glacier marine sedimentation studies within Icy Bay and elsewhere along the Gulf of Alaska coast (e.g. *Cowan and Powell*, 1991; *Jaeger and Nittrouer*, 1999; *Koppes and Hallet*, 2006; *Goff et al.*, 2012).

3.6 Near-terminus single-cell estuarine circulation

Each of our hydrographic observations are consistent with the estuarine circulation described by *Motyka et al.* (2003), in which subglacial discharge emerging at depth within the fjord entrains warm seawater and, driven by its low salinity, rises buoyantly to the fjord surface. While rising, the seawater–subglacial discharge mixture flows along the submarine glacier terminus, melting ice. On the surface, the combined mixture of seawater, subglacial discharge and submarine melt comprise an outflowing plume of glacially-modified water 10-20 m thick.

The dominant circulation pattern at the head of Icy Bay appears to be shallow, glacially-modified water flowing out of the fjord over the top of ACC water. Further from the terminus, particularly over the top of the sills, more complicated circulation patterns likely prevail. These pathways are not a focus of this study. In our near-terminus section (Fig. 3.3), we cannot entirely rule out some component of secondary circulation, or interweaving of glacially-modified water at multiple depths (cf., *Straneo et al.*, 2011). Water at 50-60 m depth is cooler and fresher than water above or below it. This pattern extends for ap-

proximately 15 km south from the glacier terminus. If multi-cell circulation is present, the small size of the salinity and temperature anomalies at depth (< 0.4 g kg^{-1} and < 1.2 °C) indicate that it is weak. The dominance of the 10-20 m thick shallow plume and the relative homogeneity of the deeper water is consistent with the shallowness of the LIA sill and the single (ACC) origin of the seawater within Icy Bay.

The depths over which Gulf of Alaska seawater is entrained at the Yahtse Glacier terminus are unclear. However, several lines of evidence indicate that the circulation may be constrained to depths less than 60 - 65 m. Between 50 and 60 m, we see an abrupt ~ 1 °C cooling. Below this depth, we see uniform, high salinities and a turbid water plume near the center of the fjord. N^2 is closer to zero, indicating a decrease in small-scale instabilities and mixing. Water near the bottom of Icy Bay may be relatively inert, and not involved in the estuarine circulation. Regardless of the details of the circulation, our across-fjord profile allows us to place bounds on the properties of the seawater entrained at the terminus by the buoyant subglacial discharge. Most likely, this entrained seawater is a mixture with properties intermediate between a deep end member ($S_A = 31.5$ g kg^{-1}, $\Theta = 4.45$ °C) and a shallow end member ($S_A = 30.9$ g kg^{-1}, $\Theta = 6.8$ °C). The mean properties over the entire near-terminus water column, appropriate for a uniform entrainment rate independent of depth, are $S_A = 30.31$ g kg^{-1}, $\Theta = 4.94$ °C.

3.7 Analysis of submarine melt rate

We consider the shallow, glacially-modified water (Fig. 3.3) to be a mixture from three sources: ambient seawater (with properties S_{As}, Θ_s), subglacial discharge (S_{Ad}, Θ_d), and submarine glacier melt (S_{Am}, Θ_m). Non-glacial freshwater sources were insignificant. The mouth of the only watershed > 10 km^2 enters Icy Bay 18 km down-fjord of the Yahtse Glacier terminus. Rain recorded by a weather station at the Yahtse Glacier terminus during the days leading up to our CTD casts was insignificant. Furthermore, we assume that all ice melting occurs at the submarine terminus and that iceberg melt is insignificant. We are justified in this due to our close proximity to the terminus, iceberg keel depths that rarely extend below 20 m, cold near-surface water temperatures and strong stratification that inhibits mixing of warmer water up to the base of the icebergs.

On a Θ/S_A diagram (Fig. 3.4), any water that is purely a mixture of seawater and subglacial discharge should fall on the mixing line joining ($S_{Ad} = 0$ g kg^{-1}, $\Theta_d = 0$ °C) with (S_{As}, Θ_s). As there are two extreme seawater end members (a deep, cold one (a) and a

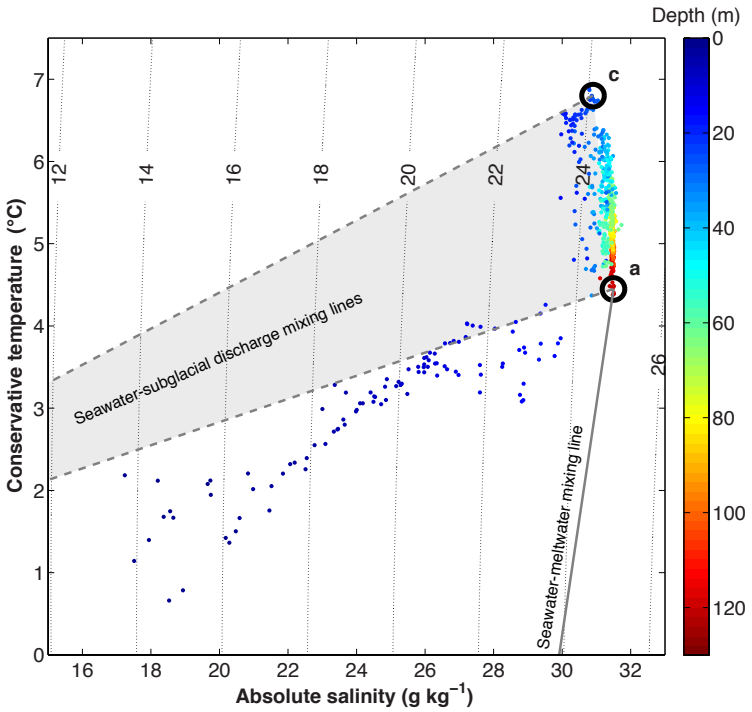

Figure 3.4. Measurements of S_A and Θ at 1 m depth intervals for each of the 7 CTD casts shown in Figs. 3.1 and 3.3. Two potential seawater end members (S_{As}, Θ_s) are circled in thick black lines and labeled as (a) and (c) to match Fig. 3.5. Mixing lines between these end members and subglacial discharge are shown as gray dashed lines and the region between these subglacial discharge mixing lines is lightly shaded. A mixing line with ice melt (*Gade*, 1979; *Jenkins*, 1999) for the cool and deep seawater end member is shown as a solid, gray line. Meltwater lines for other Θ/S_A values have similar slopes. Finely-dotted contours of potential density anomaly ($\rho_{S_A,\Theta,0} - 1000$) are labeled in kg m^{-3}.

shallow, warmer one (c)) both are identified with dashed mixing lines on Fig. 3.4. If ice is melted into a seawater-subglacial discharge mixture, the final 3-component mixture will plot below the mixing line, largely as a result of the transfer of sensible seawater heat to the latent heat needed to melt ice (*Gade*, 1979; *Jenkins*, 1999). Nearly all of the water shallower than 16 m falls outside the shaded region bounded by the two mixing lines; thus ice melt must be present at appreciable concentrations within this shallow, outflowing plume.

To solve for the relative mass fractions of seawater, subglacial discharge and submarine glacier melt within a given parcel of water (X_s, X_d, and X_m respectively), we simultane-

ously solve the following system of conservation equations

$$S_{As}X_s + S_{Ad}X_d + S_{Am}X_m = S_A \tag{3.8}$$

$$\Theta_s\, X_s + \Theta_d\, X_d + \Theta_m\, X_m = \Theta \tag{3.9}$$

$$X_s + \quad X_d + \quad X_m = 1 \tag{3.10}$$

where (S_A, Θ) are the measured, in-situ water properties.

Whereas $S_{Am} = 0$ g kg^{-1}, Θ_m is reduced by a variety of factors, the most significant of which is the latent heat necessary to melt ice. Thus,

$$\Theta_m = \Theta_f - \frac{L}{c_w} - \frac{c_i}{c_w}(\Theta_f - \Theta_i) \tag{3.11}$$

where Θ_f is the freezing point of seawater, L is the latent heat of fusion, c_w and c_i are the specific heat capacities of seawater and ice, and Θ_i is the ice temperature (*Jenkins*, 1999). At temperate Yahtse Glacier, where surface melt occurs during the summer even at the highest elevations, $\Theta_i = 0$ °C and $\Theta_m = -83.9$ °C. The influence of submarine glacier melt is shown by a third mixing line in Fig. 3.4, which represents the potential water properties of seawater mixed with varying amounts of ice melt.

To place bounds on the mass fractions of ambient seawater, subglacial discharge and submarine melt within the near-terminus glacially-modified water, we solved equations 3.8 - 3.10 at each depth and location across the fjord using the two seawater end members. These results (Fig. 3.5) reveal that up to 43% of the glacially-modified water is subglacial discharge. Meltwater reaches maximum concentrations between 2.3% and 4.1% of the shallowest water layers, with mean values for X_m between 0.5 and 2.8% across the glacially-modified water.

We emphasize that the water contents presented in Fig. 3.5 are only bounds on the true values. Neither panels (a) nor (c) of Fig. 3.5 are correct; a more plausible model will have values of X_d and X_m that lie between the two ends of the spectrum (Fig. 3.5b). For example, for the depth-averaged water properties ($S_{As} = 30.31$, $\Theta_s = 4.94$ °C), the mean $X_m = 1.1\%$. These results are summarized in Table 3.1.

In order to calculate submarine melt rates from our mass fractions, we must make an assumption about the currents within Icy Bay. Previous studies in glacierized fjords have demonstrated that instantaneous velocities, such as those measured with acoustic Doppler current profilers (ADCP), do not necessarily reflect the average currents necessary to identify melt rates (*Straneo et al.*, 2011). Instead, we draw on our time lapse photographs

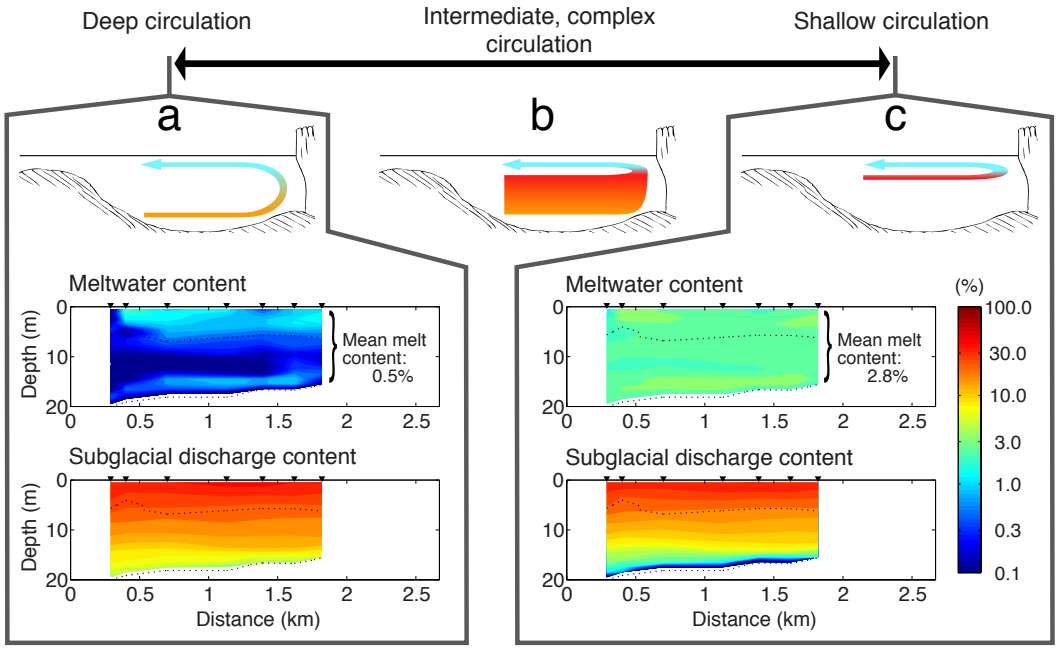

Figure 3.5. End member glacially-modified water contents and fjord circulation, showing the spectrum of possible deep to shallow water circulation patterns. (a) and (c) represent the extreme end members of the estuarine circulation. (b) represents a more plausible model, in that it is characterized by a more complex circulation that involves the entire fjord depth, and is bracketed between (a) and (c). Cartoons (approximately to scale, with vertical exaggeration) are longitudinal cross sections illustrating circulation in which (a) only deep, cool seawater is entrained and melts ice at the terminus, (b) some combination of the entire water column melts ice along the terminus, and (c) only shallow, warm water is entrained and melts ice. Lower panels show the values of X_m and X_d of the glacially-modified water, calculated from the solution of Eqs. 3.8 - 3.10 for (a) S_{As} = 31.5 g kg^{-1}, Θ_s = 4.45 °C and (c) S_{As} = 30.9 g kg^{-1}, Θ_s = 6.8 °C. The values in (a) and (c) bound the actual water contents that result from the pattern of circulation illustrated in case (b). The locations of CTD casts and the 3 and 5 °C contours are shown as in Fig. 3.3.

Table 3.1. Estimates of submarine melt for three different choices of seawater (S_{As}, Θ_s) mixed through equations 3.8 - 3.10. Mean X_m is the mean meltwater mass fraction in the glacially-modified water. Heat transport is the power necessary to melt Q_m. Q_d is an estimate of subglacial discharge within the glacially-modified water. Note that Q_m represents a flux of ice lost to submarine melt, whereas Q_d if a flux of water. † Comparison between u_i and $\dot{m}$ reveals that $\dot{m}$ cannot exceed 17 m d^{-1}.

Choice of (S_{As}, Θ_s)	Mean X_m %	Q_m m^3 s^{-1}	Heat transport 10^9 W	$\dot{m}$ m d^{-1}	Q_d m^3 s^{-1}
Warm end member	2.8	120	38	52†	650
Mean of water column	1.1	49	15	20†	650
Cold end member	0.5	20	6	9	800

of the upper fjord and field observations of drift rates to estimate u_{gmw}, the mean current within the approximately 18 m-thick outflowing surface plume.

The time lapse photograph sequence reveals two distinct regions of near-surface water flow. Outside of the turbid subglacial discharge plume, icebergs drift slowly in the absence of any strong currents (left side of fjord in Fig. 3.6 and supplementary video 3.S.1, http://www.sciencedirect.com/science/article/pii/S0012821X13004408#se0140). In contrast, icebergs that enter the persistent subglacial discharge plume are quickly carried away from the glacier terminus. The turbid, brown surface of the subglacial discharge plume largely remains iceberg free. Boat drift rates at the time of our casts were consistent with this pattern. While we did record a relatively weak down-fjord drift outside of the plume, the drift rate inside the plume was far faster, exceeding 0.50 m s^{-1}. While this observation is contemporaneous with the hydrographic survey, the time lapse photographs indicate that the swift currents within the turbid plume are persistent for several months around our survey. To ensure that our assessment of submarine melt rate is conservative, we assume that an 0.50 m s^{-1} current is confined to those parts of the fjord cross section where the turbidity was high, in excess of 70 NTU (Fig. 3.3c). We assume that no current exists elsewhere within the cross section of glacially-modified water. If we average the 0.50 m s^{-1} current of the turbid water and the zero current elsewhere, u_{gmw} = 0.084 m s^{-1}. This estimate is similar to the mean currents reported in other glacierized fjords (e.g., *Motyka et al.*, 2003; *Rignot et al.*, 2010; *Sutherland and Straneo*, 2012).

These calculations require that our currents and water properties represent tidally averaged conditions. Two lines of reasoning support this. First, tidal currents are small near the head of inlets with negligible tidal flats. A first-order, continuity-based estimate for tidal currents under these circumstances (Eq. 13 of *Friedrichs and Aubrey*, 1994) indicates that tidal currents during our cast profile were 0.0018 m s^{-1}. This is more than an order of magnitude smaller than u_{gmw}. Second, the flushing time for the portion of the fjord north of our casts (i.e., the fjord volume north of the profile divided by the flux of glacially-modified water) is approximately 1 day, larger than the semi-diurnal tidal timescale.

If we multiply u_{gmw} by the cross sectional area of the glacially-modified water and its meltwater content, we arrive at meltwater fluxes for each of our choices of (S_{As}, Θ_s) in Fig. 3.5. We estimate that the vertical surface area of the submarine portion of the terminus is 0.21 km^2 by fitting a parabola through the maximum fjord depth. Because we assume that meltwater is sourced uniformly over the submarine terminus, we arrive at submarine melt

Figure 3.6. Time lapse still image looking south over Icy Bay and the Yahtse Glacier terminus, one day prior to the CTD casts that serve as the basis for this study. Image is a still frame taken from supplementary video 3.S.1, in which the icebergs on the left (SE) 3/4 of the fjord are slowly circulating in the absence of strong near-surface currents. On the right (NW) side, the brown subglacial discharge plume with strong currents rapidly sweeps floating icebergs south into Icy Bay.

rates between 9 and 52 m d^{-1} (Table 3.1). For the case of the mean salinity and temperature, $\dot{m} = 20$ m d^{-1}. However, application of Eq. 3.5 reveals that $\dot{m}$ should not exceed 17 m d^{-1} (next section).

3.8 Comparison between submarine melt rate and the near-terminus glacier velocity

Ice surface speeds near the glacier terminus derived through the calibrated image cross-correlation are 17 m d^{-1} during the July 2011 hydrographic survey (results not shown). As at other rapidly flowing, tidewater glaciers, we assume that motion between the glacier and its bed makes up the significant majority of the speed recorded at the surface (e.g., *Meier et al.*, 1994). Furthermore the thickness (180 m) to width (2700 m) aspect ratio of the Yahtse Glacier terminus is small; the glacier is at most ~ 180 m thick and is 2700 m wide. Thus we expect that lateral stress and velocity gradients will be small and the ice flow speed near the middle of the glacier is representative of the entire terminus area. While we cannot precisely quantify the depth- and width-averaged, terminus-normal glacier velocity u_i, it is most likely not significantly less than the observed rate of 17 m d^{-1}.

At Yahtse Glacier, the terminus position change dL/dt over one day is insignificant; equation 3.5 is appropriate and, on average, $\dot{c} + \dot{m} = 17$ m d^{-1}. Thus, 52 m d^{-1} of submarine melt is contradicted by observations; $\dot{c} \geq 0$ m d^{-1}, so $\dot{m} \lesssim 17$ m d^{-1}. Because we estimate

9 m d^{-1} as a lower bound on $\dot{m}$, the submarine melt rate is at least 50% of and may easily control the entire frontal ablation rate. Subaerial calving still occurs, but we find that it is likely paced by the rate at which submarine melt undercuts the terminus.

3.9 Discussion

3.9.1 Additional assessments of our melt rate calculation

Similar to our method of calculating the meltwater flux, we can determine the subglacial discharge Q_d by multiplying u_{gmw} by the cross sectional area of the glacially-modified water and its subglacial discharge content. Depending on our choice of seawater source (Fig. 3.5), we find Q_d is between 650 and 800 m^3 s^{-1} (Table 3.1). We can compare this hydrographic estimate with an independent estimate of Q_d calculated from ablation over the entire 1020 km^2 surface area of Yahtse Glacier. During the 2011 melt season, the Michigan Tech Research Institute measured ablation at Bering Glacier, another highly-crevassed coastal glacier 70 km west of Yahtse Glacier. From their results, we derive an elevation-dependent ablation rate for the period immediately preceding our CTD casts. Then, by applying this ablation function to the hypsometry of Yahtse Glacier and assuming there are no changes in glacier water storage, we arrive at an ablation-based estimate for Q_d of 363 m^3 s^{-1}, approximately half the hydrographic estimate for subglacial discharge.

All of the rates presented within Table 3.1 scale linearly with u_{gmw}. The assumption of no change in glacier water storage is crude, but if the ablation rate Q_d estimate is correct and the hydrographic estimates for Q_d are too large by a factor of 2, then the u_{gmw} and $\dot{m}$ are also large by a factor of 2. In this case, better bounds would be $4.5 \leq \dot{m} \leq 26$. A 2-D numerical model based on *Jenkins* (2011) is another approach for estimating $\dot{m}$, which is entirely different than our method of un-mixing the glacially modified water. Application of this model to our CTD casts, under the assumption that subglacial discharge is released evenly across the width of the terminus, suggests that our estimate of $\dot{m}$ may be high by a factor of 2 – 3 (A. Jenkins, pers. comm. 2013). However, the similarity of the results from each of these approaches increases our confidence in the magnitude of our $\dot{m}$ calculation.

3.9.2 Seasonal to interannual context

Our late July measurements from each year are a snapshot from an annual cycle. Salinity and temperature of the ACC vary seasonally and we expect $\dot{m}$ to as well. After rising

through a series of step increases, near-surface temperatures within the ACC typically reach their maximum values (~ 13 °C) in July and August before decaying through the fall and winter (Fig. 3.2d and *Royer*, 2005). During the summer, increases in temperature may be associated with decreases in salinity.

Relatively small-scale deviations from these seasonal patterns appear manifest within our Icy Bay casts. In 2010, the temperature of the ACC stepped from 9 to 11 °C, 18 days prior to our measurement for that year (Fig. 3.2d). Steps to similarly warm temperatures occurred either during or after our 2009 and 2011 measurements. In those years, temperatures prior to the casts were cooler and barely exceeded 9 °C. This interannual contrast in the ACC is reflected in the contrast among our Icy Bay CTD casts. The pronounced warmth between 20 and 60 m in 2010 demonstrates that the water reaching the heads of Icy Bay's glacierized fjords is strongly connected to the water on Alaska's continental shelf.

We can determine a first-order time series of submarine melt rates for Yahtse and other tidewater glaciers around the Gulf of Alaska by applying equation 3.6 to the ACC temperature (a proxy for Θ_s) and estimates of freshwater discharge to the Gulf of Alaska from *Royer* (1982) (a proxy for q). Freshwater delivery to the ACC (including contributions from subglacial discharge) peaks between September and November, with values roughly twice those typical of July. This calculation reveals that the submarine melt rate typically peaks in September, when the ACC is warm and powerful fall storms drench the Gulf of Alaska (Fig. 3.7). July $\dot{m}$ is typically 70% of the September maximum, however, due to the unseasonably cool July 2011 water temperatures, our calculations reveal that typical September $\dot{m}$ may be 1.8 times greater than we report in this study. In a typical year, submarine melt rates may be at least as high as we report during 6 months of the year. Again, $\dot{m} \lesssim u_i$, but these simple calculations emphasize the significance of submarine melt as a controlling mass loss process at Yahtse Glacier.

We expect that submarine melting may be an important driver of the seasonal cycle of terminus advance and retreat observed at Yahtse Glacier. The terminus is most-advanced in the spring, after the minimum in melt rate, and most-retracted in the fall, after the maximum in melt rate. *Motyka et al.* (2003) and *Ritchie et al.* (2008) report similar observations at LeConte and Hubbard Glaciers. Seasonal terminus retreat has also been reported at Columbia Glacier. There, the development of "seasonal embayments" (locally retracted regions of the terminus) were also associated with the location of turbid subglacial discharge plumes (*Sikonia and Post*, 1980; *Krimmel and Vaughn*, 1987). *Sikonia and Post* (1980)

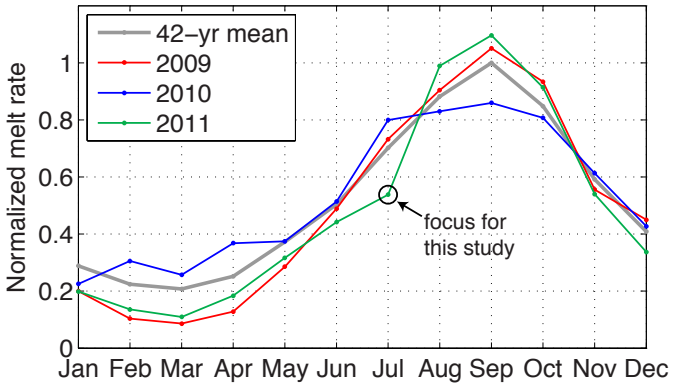

Figure 3.7. Annual cycle of submarine melt rates for Gulf of Alaska tidewater glaciers. Values are calculated according to equation 3.6 with $p = 1/3$ by application of the monthly mean 20-m-depth conservative temperature from GAK1 (*Royer*, 2005), and the monthly mean freshwater discharge to the Gulf of Alaska (*Royer*, 1982). The annual cycle is not significantly different with $p = 1/2$. Melt rates are normalized by the maximum monthly rate of the 42-yr mean. The 42-yr mean uses temperature data from opportunistic casts made between 1970 and 2011; January is the least-represented month, with measurements from 14 yrs. The 2009-2011 data use the monthly mean temperature recorded by a mooring (Fig. 3.2d).

demonstrated a strong link between a proxy for subglacial discharge and frontal ablation rate. A seasonal embayment was present at Yahtse Glacier for much of the summer of 2011, where the terminus above the persistent, turbid plume retracted 400 m behind the rest of the terminus (Fig. 3.1b).

3.9.3 Onset of rapid tidewater glacier retreat

At their most advanced positions, many Alaskan tidewater glaciers terminated on shallow shoals that have the potential to shield the glacier terminus from warm water at depth. The LIA maximum at Icy Bay is no deeper than 17 m; elsewhere in Alaska, sills are similarly shallow (*Muench and Heggie*, 1978; *Walters et al.*, 1988). Subglacial discharge emerging at depths less than 20 m would only entrain cool water against the glacier terminus and melt rates would have been small. However, once retreat begins (perhaps through a change in climate (*Post et al.*, 2011)), ambient seawater may be exchanged with the deepening basin in front of the terminus and discharge of subglacial water at greater depths initiates the estuarine circulation described in this study and in *Motyka et al.* (2003). Submarine melt rates will increase.

As the terminus retreats into yet deeper water, more submarine ice surface area is exposed to warm seawater and Q_m increases, even if $\dot{m}$ remains constant. Even in ~ 110 m deep water, the glacially-modified water that emerges at the surface of Icy Bay is several degrees above its freezing point, and thus could potentially melt more ice. Therefore, we can expect submarine melt to increase if the terminus is exposed to more warm water at depth. This mechanism offers a potential physical explanation for empirical relationships between water depth and frontal ablation rate (*Brown et al.*, 1982; *van der Veen*, 2002).

3.9.4 Comparison with other glacier-fjord systems

Subglacial discharge and warm seawater promote submarine melt together (Eq. 3.6). If the flux of subglacial discharge is the same in two different fjords, we expect submarine melt rates in the narrower fjord to be greater than those in the wider fjords. In narrow fjords, subglacial discharge is focused beneath a narrow glacier terminus (q is greater), more warm seawater is entrained (*Jenkins*, 2011), and a larger proportion of the glacier terminus undergoes significant submarine melt. Overall, Q_m is greater for narrow fjords, than for wide fjords. Similarly, q is also greater at glaciers with larger rates of subaerial surface melt. These glaciers should also experience larger rates of submarine melt. Thus, the submarine melt rate is linked to surface melt and runoff on the glacier surface.

In contrast, we anticipate less submarine melt where glaciers with low surface melt rates flow steeply down to tidewater within a wide fjord. This is the case at the East Greenland outlet glaciers, including Helheim and Kangerdlugssuaq Glaciers. At Helheim Glacier, mid-summer subaerial melt production is estimated at 170 $m^3\ s^{-1}$ (*Andersen et al.*, 2010), approximately half the melt at Yahtse Glacier, and is released at a glacier terminus that is twice as wide as that of Yahtse Glacier. Thus, it is not surprising that the submarine melt rates are small, approximately 2 m d^{-1} (even disregarding the contrast in water temperature (*Sutherland and Straneo*, 2012)). Furthermore, the buoyancy flux provided by subglacial discharge is insufficient to bring all of the mixed, glacially-modified water to the surface (*Straneo et al.*, 2011; *Sciascia et al.*, 2013). Instead, the fjord in front of Helheim Glacier is characterized by a more complicated circulation pattern, with glacially-modified water found at depth, as well as on the surface.

The relative warmth of the ACC compared with the east and west coasts of Greenland also plays an important part in governing submarine melt (*Weingartner et al.*, 2005; *Straneo et al.*, 2012). These differences in temperatures on the shelf propagate up-fjord and persist

at the glacier terminus. The temperature of the ACC is at least 8 °C warmer than the water temperature at the mouths of Greenlandic fjords (*Straneo et al.*, 2012) and at least 11 °C warmer than the water off the coast of Antarctica (*Pritchard et al.*, 2012). These temperature contrasts can be expected to yield melt rates at Alaskan glaciers that are severalfold greater than those at either of the polar ice sheets (Eq. 3.6).

Further contrasts among glacier-fjord systems, such as ice flow rate or advance/retreat state of the terminus, are unlikely to have a direct effect on the submarine melt rate. Indirect effects may come about through development of submarine moraines that can shield the terminus from the warmest water (Section 3.9.3), or through the generation of meltwater at the glacier bed. Faster flowing ice, with a more dynamic subglacial hydrologic system, can potentially move sediment more quickly to the terminus than slower flowing ice. If a glacier terminus is also advancing or stable, then that sediment will contribute to the development or maintenance of a submarine terminal moraine.

3.10 Conclusions

Near the front of Yahtse Glacier, a tidewater glacier terminating in Icy Bay, we quantified the heat deficit of the water within the cold surface layer to place bounds on the rate of submarine melt. We have demonstrated that submarine melt has the potential to match the speed at which ice flows into the terminus. Therefore, calving of subaerial icebergs may largely be a response to undercutting of the terminus during our observation period. Because approximately one third of this grounded glacier terminus is above sea level, one third of frontal ablation at Yahtse Glacier is subaerial calving. However, the rate at which subaerial calving occurs may be controlled by how quickly submarine melt removes the pedestals on which subaerial seracs rest. Process-based models that attempt to predict iceberg calving without accounting for submarine melt are unlikely to be successful.

Observations in the field are consistent with the results of this study. We observed rapid terminus retreat in the vicinity of upwelling, turbid subglacial discharge, and a dearth of submarine iceberg calving events. During an early-June observation period, only 6% of visually-observed calving events involved a submarine-released iceberg despite an estimated 65% of the terminus being below sea level (*Bartholomaus et al.*, 2012). Similar to the case at LeConte Glacier (*Motyka et al.*, 2003), subglacial discharge produced by several cm d^{-1} ablation over an extensive subaerial glacier surface exits through a relatively narrow glacier terminus. This drives convection at the glacier front that entrains warm,

ambient seawater, melts the submarine terminus, and generates a 10 - 20 m thick surface layer of water flowing out away from the glacier terminus.

We note that large, 9 – 17 m d^{-1} melt rates are insufficient on their own to drive terminus retreat. Rather, the terminus of Yahtse Glacier has been advancing at 100 m yr^{-1} for the last two decades. Similarly, most of Alaska's tidewater glaciers are presently stable, despite the observed 0.3 °C per decade temperature increase of the ACC since the 1970s (*McNabb*, 2013; *Royer and Grosch*, 2006). These observations demonstrate that other factors, such as glacier geometry, must also be important in dictating whether rapid submarine melt will be associated with terminus retreat.

Submarine melt represents an important link between the ocean and tidewater glaciers. In East Greenland, increased freshwater discharge to the coastal current enhances the rate at which cold water is advected from the north, potentially reducing submarine melt and stabilizing the tidewater glaciers found there (*Murray et al.*, 2010). On the Alaska coast, the effect is opposite: as freshwater runoff increases, the ACC more rapidly transports warm water from lower latitudes to the mouths of Alaska's fjords (*Royer*, 1982; *Weingartner et al.*, 2005). This feedback has been implicated in the ACC warming (*Royer and Grosch*, 2006). Should rates of freshwater delivery continue to increase (*Neal et al.*, 2010), we can expect the strong links between the ACC and glacierized fjords to enable future increases in submarine melt rates.

3.11 Acknowledgements

This research was supported in part by a UAF Center for Global Change Student Research Grant with funds from the Cooperative Institute for Alaska Research. Additional funding was provided by the National Science Foundation through grant EAR-0810313, the USGS Climate and Land Use Change R&D program, and the Dept. of Interior Alaska Climate Science Center. This work would not have been possible without the generous loan of instruments by Roman Motyka and a skiff by Michelle Kissling; our heartiest thanks go to them. We thank Erin Pettit and Jeff Nystuen for their contributions toward collecting the CTD data from 2009. Roman Motyka, Erin Pettit, Barbara Truessel, Megan O'Sadnick, Joel Brann, Paul Aguilar, and Eric Boget assisted with field work. We thank Mark Fahnestock for providing the image cross correlation algorithm. Comments by Johnny Sanders and three anonymous reviewers significantly improved this manuscript. We gratefully acknowledge the Institute of Marine Sciences at UAF for provision of GAK1

data (http://www.ims.uaf.edu/gak1/) and the Michigan Tech Research Institute Bering Glacier project for provision of ablation data (http://geodjango.mtri.org/gass/).

References

Andersen, M. L., et al. (2010), Spatial and temporal melt variability at Helheim Glacier, East Greenland, and its effect on ice dynamics, *J. Geophys. Res.*, *115*(F4), 1–18, doi: 10.1029/2010JF001760.

Arimitsu, M. L., J. F. Piatt, E. N. Madison, J. S. Conaway, and N. Hillgruber (2012), Oceanographic gradients and seabird prey community dynamics in glacial fjords, *Fish. Oceanogr.*, *21*(2-3), 148–169, doi: 10.1111/j.1365-2419.2012.00616.x.

Barclay, D. J., J. L. Barclay, P. E. Calkin, and G. C. Wiles (2006), A Revised and Extended Holocene Glacial History of Icy Bay, Southern Alaska, U.S.A, *Arctic, Antarctic, and Alpine Research*, *38*(2), 153–162, doi: 10.1657/1523-0430(2006)38[153:ARAEHG]2.0.CO;2.

Bartholomaus, T. C., C. F. Larsen, S. O'Neel, and M. E. West (2012), Calving seismicity from iceberg-sea surface interactions, *J. Geophys. Res.*, *117*(F4), 1–16, doi: 10.1029/2012JF002513.

Brown, C. S., M. F. Meier, and A. Post (1982), Calving speed of Alaska tidewater glaciers, with application to Columbia Glacier, *USGS Prof. Pap.*, *1258-C*, C1–C13.

Cogley, J. G., et al. (2011), Glossary of glacier mass balance and related terms, *Tech. rep.*, IHP-VII Technical Documents in Hydrology No. 86, IACS Contribution No. 2, UNESCO-IHP, Paris.

Cowan, E. A., and R. Powell (1991), Ice-proximal sediment accumulation rates in a temperate glacial fjord, southeastern Alaska, in *Glacial Marine Sedimentation: Paleoclimatic Significance*, edited by J. B. Anderson and G. M. Ashley, pp. 61–74, Geol. Soc. Am. Spec. Pap., 261.

Friedrichs, C. T., and D. G. Aubrey (1994), Tidal propagation in strongly convergent channels, *J. Geophys. Res.*, *99*(C2), 3321–3336, doi: 10.1029/93JC03219.

Gade, H. G. (1979), Melting of ice in sea water: a primitive model with application to the Antarctic ice shelf and icebergs, *J. Phys. Oceanogr.*, *9*(1), 189–198.

Goff, J. A., D. E. Lawson, B. A. Willems, M. Davis, and S. P. S. Gulick (2012), Morainal bank progradation and sediment accumulation in Disenchantment Bay, Alaska: Response to advancing Hubbard Glacier, *J. Geophys. Res.*, *117*(F2), 1–15, doi: 10.1029/2011JF002312.

IOC, SCOR, and IAPSO (2010), *The international thermodynamic equation of seawater - 2010: Calculation and use of thermodynamic properties.*, 196 pp., Intergovernmental Oceanographic Commission, Manuals and Guides No. 56, UNESCO.

Jaeger, J. M., and C. A. Nittrouer (1999), Sediment deposition in an Alaskan fjord: Controls on the formation and preservation of sedimentary structures in Icy Bay, *J. Sediment. Res.*, *69*, 1011–1026, doi: 10.1306/D4268AF4-2B26-11D7-8648000102C1865D.

Jenkins, A. (1999), The Impact of Melting Ice on Ocean Waters, *J. Phys. Oceanogr.*, *29*(9), 2370–2381, doi: 10.1175/1520-0485(1999)029<2370:TIOMIO>2.0.CO;2.

Jenkins, A. (2011), Convection-driven melting near the grounding lines of ice shelves and tidewater glaciers, *J. Phys. Oceanogr.*, *41*(12), 2279–2294.

Koppes, M., and B. Hallet (2006), Erosion rates during rapid deglaciation in Icy Bay, Alaska, *J. Geophys. Res.*, *111*(F2), 1–11, doi: 10.1029/2005JF000349.

Krimmel, R. M., and B. H. Vaughn (1987), Columbia Glacier, Alaska: changes in velocity 1977âĂŞ1986, *J. Geophys. Res.*, *92*(B9), 8961–8968, doi: 10.1029/JB092iB09p08961.

Larsen, C. F., R. J. Motyka, A. A. Arendt, K. A. Echelmeyer, and P. E. Geissler (2007), Glacier changes in southeast Alaska and northwest British Columbia and contribution to sea level rise, *J. Geophys. Res.*, *112*(F1), 1–11, doi: 10.1029/2006JF000586.

Matthews, J. B. (1981), The seasonal circulation of the Glacier Bay, Alaska fjord system, *Estuar. Coast. Shelf S.*, *12*, 679–700.

McNabb, R. (2013), On the frontal ablation of Alaska tidewater glaciers, Ph.D. Dissertation, University of Alaska Fairbanks.

Meier, M., et al. (1994), Mechanical and hydrologic basis for the rapid motion of a large tidewater glacier, *J. Geophys. Res.*, *99*(B8), 15,219–15,229.

Motyka, R. J., L. Hunter, K. A. Echelmeyer, and C. Connor (2003), Submarine melting at the terminus of a temperate tidewater glacier, LeConte Glacier, Alaska, U.S.A., *Ann. Glaciol.*, *36*(1), 57–65, doi: 10.3189/172756403781816374.

Muench, R. D., and D. T. Heggie (1978), Deep water exchange in Alaskan subarctic fjords, in *Estuarine Transport Processes*, edited by B. Kjerfve, pp. 239–267, University of South Carolina Press, Columbia, South Carolina.

Murray, T., et al. (2010), Ocean regulation hypothesis for glacier dynamics in southeast Greenland and implications for ice sheet mass changes, *J. Geophys. Res.*, *115*(F3), 1–15, doi: 10.1029/2009JF001522.

Neal, E. G., E. Hood, and K. Smikrud (2010), Contribution of glacier runoff to freshwater discharge into the Gulf of Alaska, *Geophys. Res. Lett.*, *37*(6), 1–5, doi: 10.1029/2010GL042385.

Nick, F. M., A. Vieli, I. M. Howat, and I. Joughin (2009), Large-scale changes in Greenland outlet glacier dynamics triggered at the terminus, *Nat. Geosci.*, *2*(2), 110–114, doi: 10.1038/NGEO394.

O'Leary, M., and P. Christoffersen (2013), Calving on tidewater glaciers amplified by submarine frontal melting, *The Cryosphere*, *7*(1), 119–128, doi: 10.5194/tc-7-119-2013.

Porter, S. C. (1989), Late Holocene Fluctuations of the Fiord Glacier System in Icy Bay, Alaska, U.S.A., *Arctic Alp. Res.*, *21*(4), 364, doi: 10.2307/1551646.

Post, A. (1983), Preliminary bathymetry of upper Icy Bay, Alaska, *USGS Prof. Pap.*, *OF 83-256*, 1 sheet.

Post, A., S. O'Neel, R. J. Motyka, and G. Streveler (2011), A complex relationship between calving glaciers and climate, *Eos Trans. AGU*, *92*(37), 305, doi: 10.1029/2011EO370001.

Pritchard, H. D., R. J. Arthern, D. G. Vaughan, and L. A. Edwards (2009), Extensive dynamic thinning on the margins of the Greenland and Antarctic ice sheets., *Nature*, *461*(7266), 971–5, doi: 10.1038/nature08471.

Pritchard, H. D., S. R. M. Ligtenberg, H. a. Fricker, D. G. Vaughan, M. R. van den Broeke, and L. Padman (2012), Antarctic ice-sheet loss driven by basal melting of ice shelves, *Nature*, *484*(7395), 502–505, doi: 10.1038/nature10968.

Rignot, E., M. Koppes, and I. Velicogna (2010), Rapid submarine melting of the calving faces of West Greenland glaciers, *Nat. Geosci.*, *3*(3), 187–191, doi: 10.1038/ngeo765.

Ritchie, J. B., C. S. Lingle, R. J. Motyka, and M. Truffer (2008), Seasonal fluctuations in the advance of a tidewater glacier and potential causes: Hubbard Glacier, Alaska, USA, *J. Glaciol.*, *54*(186), 401–411.

Royer, T. C. (1982), Coastal fresh water discharge in the northeast Pacific, *J. Geophys. Res.*, *87*(1), 2017–2021.

Royer, T. C. (2005), Hydrographic responses at a coastal site in the northern Gulf of Alaska to seasonal and interannual forcing, *Deep Sea Research Part II: Topical Studies in Oceanography*, *52*(1-2), 267–288, doi: 10.1016/j.dsr2.2004.09.022.

Royer, T. C., and C. E. Grosch (2006), Ocean warming and freshening in the northern Gulf of Alaska, *Geophys. Res. Lett.*, *33*(16), L16,605, doi: 10.1029/2006GL026767.

Scambos, T. A., M. J. Dutkiewicz, J. C. Wilson, and R. A. Bindschadler (1992), Application of Image Cross-Correlation to the Measurement of Glacier Velocity Using Satellite Image Data, *Remote Sens. Environ.*, *42*(1992), 177–186.

Sciascia, R., F. Straneo, C. Cenedese, and P. Heimbach (2013), Seasonal variability of submarine melt rate and circulation in an East Greenland fjord, *J. Geophys. Res.*, *118*(February), 1–15, doi: 10.1002/jgrc.20142.

Seale, A., P. Christoffersen, R. I. Mugford, and M. O'Leary (2011), Ocean forcing of the Greenland Ice Sheet: Calving fronts and patterns of retreat identified by automatic satellite monitoring of eastern outlet glaciers, *J. Geophys. Res.*, *116*(F3), 1–16, doi: 10.1029/2010JF001847.

Sikonia, W. G., and A. Post (1980), Columbia Glacier, Alaska; recent ice loss and its relationship to seasonal terminal embayments, thinning, and glacial flow, *U.S. Geological Survey Hydrologic Investigations Atlas 619*, p. 3.

Stabeno, P. J., N. A. Bond, A. J. Hermann, N. B. Kachel, C. W. Mordy, and J. E. Overland (2004), Meteorology and oceanography of the Northern Gulf of Alaska, *Cont. Shelf Res.*, *24*, 859–897, doi: 10.1016/j.csr.2004.02.007.

Straneo, F., R. G. Curry, D. A. Sutherland, G. S. Hamilton, C. Cenedese, K. Vå ge, and L. A. Stearns (2011), Impact of fjord dynamics and glacial runoff on the circulation near Helheim Glacier, *Nat. Geosci.*, *4*(5), 322–327, doi: 10.1038/ngeo1109.

Straneo, F., D. A. Sutherland, D. Holland, C. Gladish, G. S. Hamilton, H. L. Johnson, E. Rignot, Y. Xu, and M. Koppes (2012), Characteristics of ocean waters reaching GreenlandâĂŹs glaciers, *Ann. Glaciol.*, *53*(60), 202–210, doi: 10.3189/2012AoG60A059.

Sutherland, D. A., and F. Straneo (2012), Estimating ocean heat transports and submarine melt rates in Sermilik Fjord, Greenland, using lowered acoustic Doppler current profiler (LADCP) velocity profiles, *Ann. Glaciol.*, *53*(60), 50–58, doi: 10.3189/2012AoG60A050.

van der Veen, C. J. (2002), Calving glaciers, *Prog. Phys. Geog.*, *26*(1), 96–122, doi: 10.1191/0309133302pp327ra.

Walters, R. A., E. G. Josberger, and C. L. Driedger (1988), Columbia Bay, Alaska: an 'upside down' estuary, *Estuar. Coast. Shelf S.*, *26*, 607–617.

Weingartner, T. J., S. L. Danielson, and T. C. Royer (2005), Freshwater variability and predictability in the Alaska Coastal Current, *Deep-Sea Res. Pt. II*, *52*(1-2), 169–191, doi: 10.1016/j.dsr2.2004.09.030.

Xu, Y., E. Rignot, D. Menemenlis, and M. Koppes (2012), Numerical experiments on subaqueous melting of Greenland tidewater glaciers in response to ocean warming and enhanced subglacial discharge, *Ann. Glaciol.*, *53*(60), 229–234, doi: 10.3189/2012AoG60A139.

Appendix 3.A Additional hydrographic data

These supplemental figures depict additional data collected during July 2011.

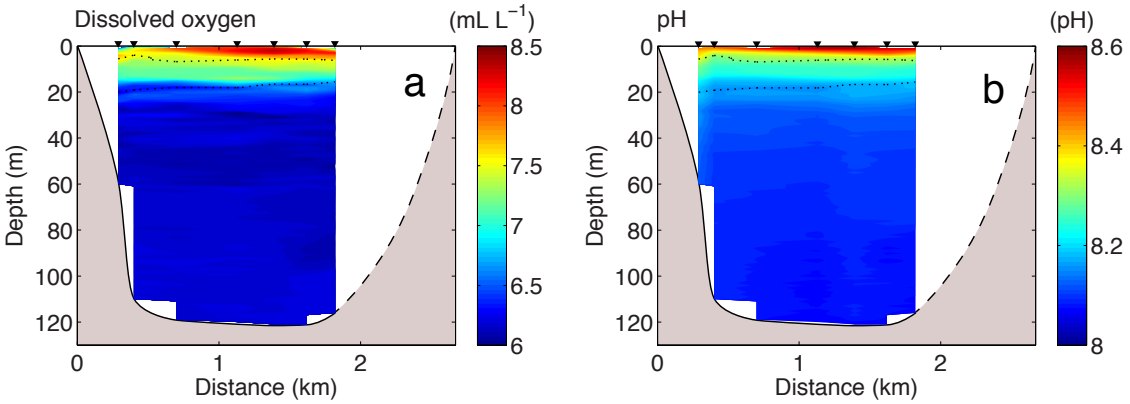

Figure 3.A.1. Dissolved oxygen (a) and pH (b) of the near-terminus section (Fig. 3.3). The dissolved oxygen concentrations equate to an oxygen saturation of approximately 85% across the bottom waters; shallow waters are between 90 - 98% saturated. The patterns of dissolved oxygen and pH may reflect a primary productivity signal in the shallow photic zone (e.g., *Arimitsu et al.*, 2012). High dissolved oxygen near the surface may also indicate water that had recently been on the glacier surface (i.e., is now subglacial discharge). The locations of CTD casts and the 3 and 5 °C contours are shown as in Fig. 3.3.

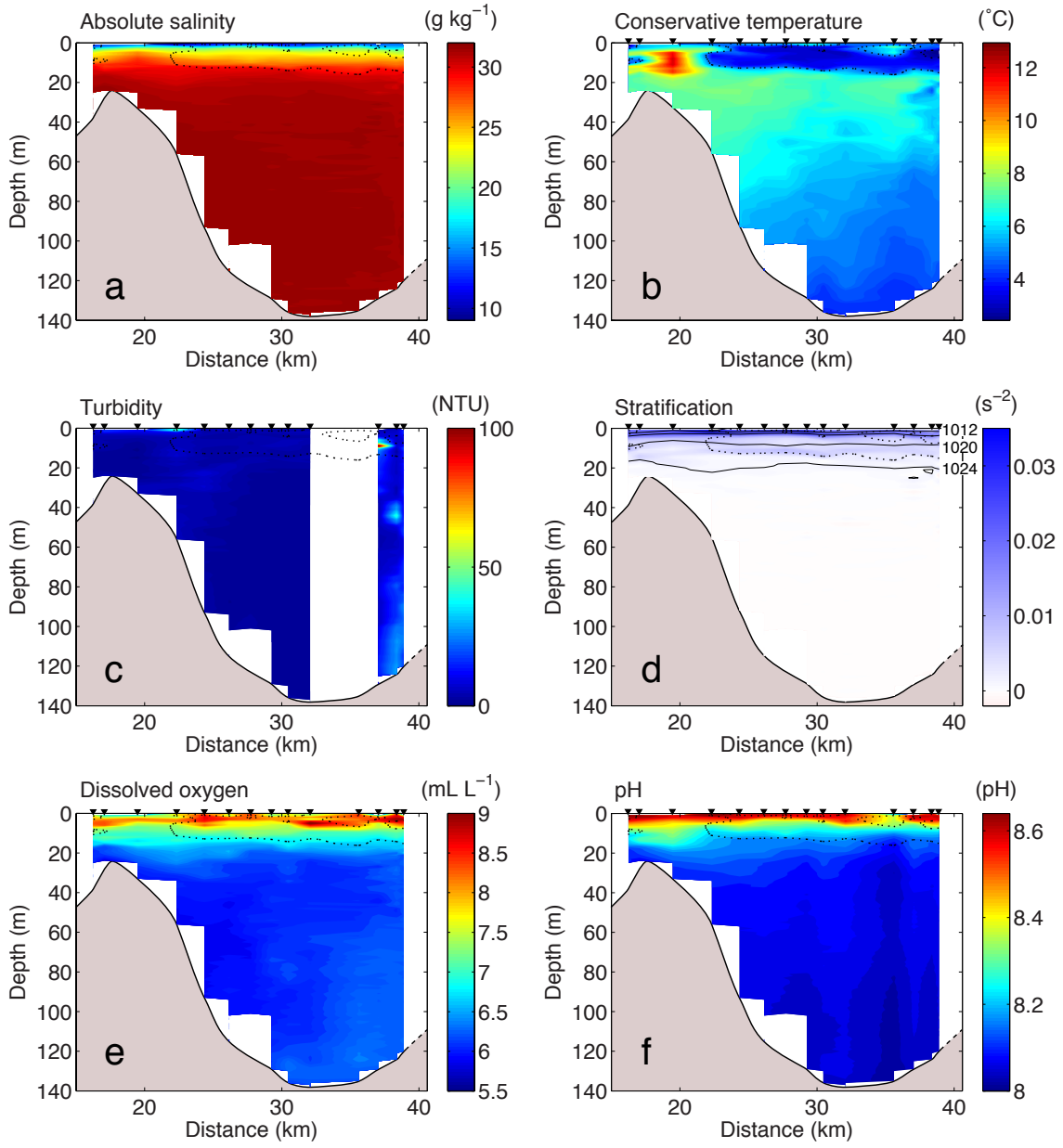

Figure 3.A.2. Water properties in an along-bay, centerline, cross section of Icy Bay, collected on 26-27 July 2011. Location shown with a gray line in Fig. 3.1a. The LIA maximum is at 0 km; 40.6 km is the terminus of Yahtse Glacier. a) absolute salinity, b) conservative temperature, c) turbidity, f) N^2 shown by the colorbar, overlain by black density contours (contour interval is 4 kg m^{-3}; several densities are labeled) e) dissolved oxygen, and f) pH. Note that color scales are different than those used in Fig. 3.3. The cold surface layer extends over the 17 km sill to the NW of this cross section (Fig. 3.A.3). The warm temperatures shown likely reflect incoming water from the ACC over the SE end of the broad sill.

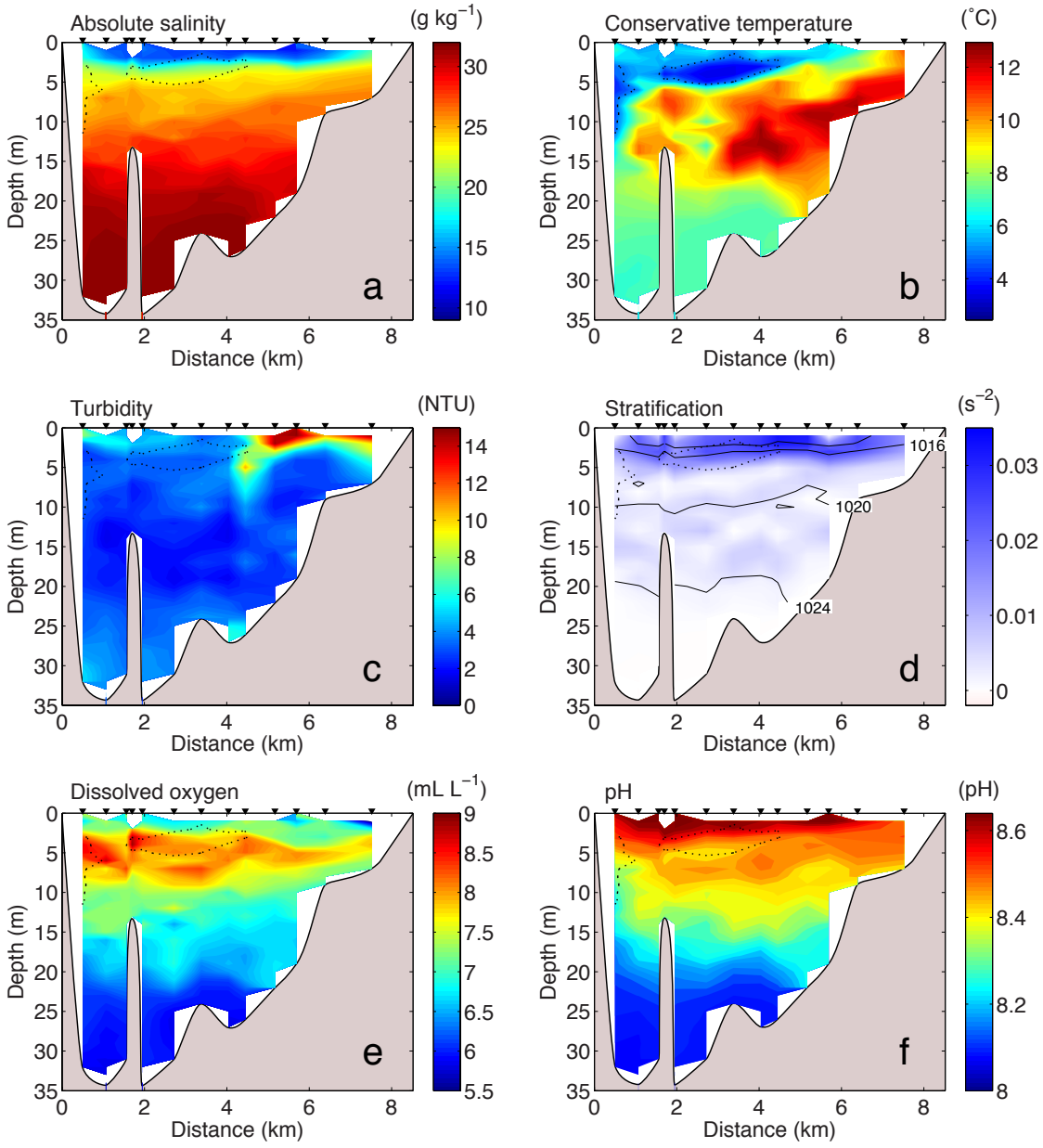

Figure 3.A.3. Water properties in a cross section across the top of the 17 km sill, looking up-Bay. Data collected on 28 July 2011. The NW shore of Icy Bay is at 0 km; 8.5 km is the SE shore. Panels and color scales are as in Fig. 3.A.2, with the exception of the turbidity color scale.

Chapter 4
Observing iceberg calving flux at a grounded tidewater glacier with passive seismology[1]

4.1 Abstract

Iceberg calving regulates the discharge of ice from many of the world's largest glaciers. Annual to seasonal variations in calving flux can be significant, but the processes controlling these variations are poorly known. In part, improved understanding of the controls on iceberg calving requires better knowledge of when and how much iceberg calving occurs. The seismic signatures of calving events, calving icequakes, offer one way to examine calving in greater detail than is available through other methods. However, studies of calving icequakes have thus far been hampered by an inability to identify the size of an iceberg by the icequake it produces. At Yahtse Glacier, Alaska, we use an in-person record of iceberg calving events and coincident, locally-recorded icequakes to build a statistical model through which we can predict the size of an iceberg by the icequake it produces. We find that the icequake duration is the single most significant predictor of iceberg size. We then apply this model to 18 months of icequake recordings and find elevated iceberg calving flux during the summer and fall, and a pronounced lull in calving during mid-winter. Summer calving flux varies among years by up to 50%, and is sensitive to tidal stage at a number of periods including semidiurnal, diurnal, fortnightly and monthly. Our study demonstrates that iceberg sizes and calving flux can be estimated from seismic parameters to remotely monitor temporally-varying calving fluxes.

4.2 Introduction

Passive seismology is an emerging tool for the study of iceberg calving. Wherever seismometers have been deployed in the vicinity of tidewater glaciers, seismic transients ("icequakes") are observed in association with calving events (e.g., *Qamar*, 1988; *Amundson et al.*, 2010; *O'Neel et al.*, 2010; *Köhler et al.*, 2012; *Walter et al.*, 2012; *Veitch and Nettles*, 2012). Calving icequakes are characterized by their detectability at regional distances, peaks in spectra between 1 and 5 Hz, emergent onsets lacking clear phase arrivals, and local magnitudes near 1 (*Wolf and Davies*, 1986; *O'Neel et al.*, 2007, 2010; *Bartholomaus et al.*, 2012). These calving icequakes contrast with another class of calving seismicity: the glacial earthquakes ini-

[1] A version of this manuscript will be submitted to the *Journal of Geophysical Research: Earth Surface*, as Bartholomaus, T.C., C.F. Larsen, M.E. West, S. O'Neel, E.C. Pettit, and M. Truffer, Observing iceberg calving flux at a grounded tidewater glacier with passive seismology.

tially reported by *Ekström et al.* (2003). Glacial earthquakes have surface wave magnitudes near 4 or 5 and are characterized by their globally-detected, 35-150 s period surface waves (*Ekström et al.*, 2003; *Tsai and Ekström*, 2007). These seismic events predominantly originate at fifteen of the largest glaciers in Greenland, when full-glacier-thickness icebergs rotate and push off against the glacier terminus (*Amundson et al.*, 2008; *Tsai et al.*, 2008; *Veitch and Nettles*, 2012).

The different character of glacial earthquakes and calving icequakes indicate that different source mechanisms are responsible for the two types of seismic events. However, calving icequakes do co-locate with glacial earthquakes, and occur both simultaneous with and independent of glacial earthquakes (*Amundson et al.*, 2010; *Walter et al.*, 2012). Calving icequakes appear to be ubiquitous at the termini of calving glaciers.

This study builds on existing calving icequake research that has focused on the identification and location of calving events (*O'Neel et al.*, 2007, 2010; *Köhler et al.*, 2012). Although iceberg sizes are potentially recoverable from glacial earthquake signals (*Tsai and Ekström*, 2007; *Veitch and Nettles*, 2012), few other studies have systematically demonstrated an ability to capture iceberg size, and therefore calving flux, using seismic parameters. Notable exceptions have focused either on a small set of potential predictors (*Qamar*, 1988; *O'Neel et al.*, 2007), or on a short duration (*Qamar*, 1988).

In this study, we explore a rich dataset to identify icequake properties that most reliably predict the size of the iceberg that generated them. Then we apply this statistical model to a set of over 400,000 icequakes that we identify as produced by iceberg calving at Yahtse Glacier. This yields approximately 18 months of calving estimates, whose temporal variability we interpret in an attempt to learn about the factors controlling the rates of iceberg calving.

4.3 Datasets

Our analysis of calving occurrence at Yahtse Glacier builds on a combination of locally-recorded seismic data and a record of visually and audibly observed calving events. The seismic network includes up to 9 broadband seismometers buried within thin sediment near the terminus of Yahtse Glacier between June 2009 and September 2011 (Fig. 4.1). The network aperture was approximately 12 km and stations consisted predominantly of Guralp CMG-3Ts with Quanterra 330 digitizers and balers. These sensors have a flat

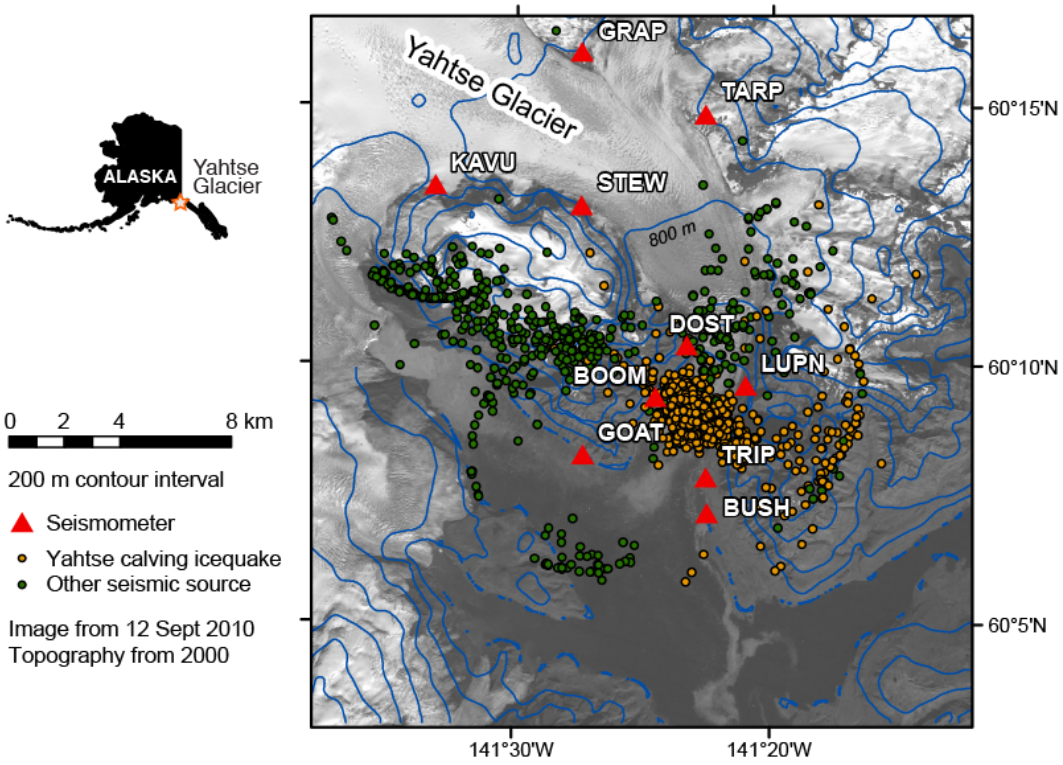

Figure 4.1. Map of lower Yahtse Glacier, with locations of icequakes and 10 seismic stations. Station TRIP was installed after station BUSH was damaged. Small orange and green circles identify the origins of 2000 seismic events identified either as produced by iceberg calving at Yahtse Glacier, or produced by other processes. The terminus of Yahtse Glacier is beneath the densest cluster of located Yahtse calving icequakes. The background image is a Landsat 7 scene overlain with contours from NASA's Shuttle Radar Topography Mission.

response from 120 s to 50 Hz. Sampling rate varied over the course of our experiment between 100 and 200 samples per second.

The observer record consists of direct visual or audible observations of 4589 events at the terminus of Yahtse Glacier over 13 days during June 2010 (described in *Bartholomaus et al.*, 2012). Among other properties, the size of each calving event was estimated using an integer scale. These sizes ranged from 1 to 7; their occurrence rate are well-fit by an exponential distribution (we record 3329 size 1 icebergs for each size 7 iceberg).

4.4 Analysis

4.4.1 Seismic event detections

The seismic energy produced by calving icequakes at Yahtse Glacier and other tidewater glaciers in Alaska is peaked between 1 and 5 Hz (*O'Neel et al.*, 2007, 2010; *Bartholomaus et al.*, 2012). Therefore, we use the frequency domain detector described in *O'Neel et al.* (2007) to automatically detect all seismic events between 1 and 5 Hz recorded at BOOM, the station closest to the Yahtse Glacier terminus. We merge the detection times and durations on the station's vertical, northing and easting channels to create one master list of seismic detections while ensuring that individual seismic events are not double-counted. This yields a list of 568,911 detections during 606 days during which BOOM operated. The average detection rate was 0.65 events per minute; cumulatively, detections make up 13% of the operational time at BOOM.

4.4.2 Source locations

Our goal is to cull the complete catalog of seismic detections to just those icequakes produced by calving at Yahtse Glacier. The first step is to remove earthquakes, because the location procedure we describe next performs unsatisfactorily for any seismic events originating more than a couple km outside the bounds of our network.

Arrivals from teleseismic earthquakes are typically longer-period than the 1-5 Hz passband in which calving icequakes were detected at Yahtse Glacier, and are unlikely to contaminate our catalog (*Bartholomaus et al.*, 2012; *Stein and Wysession*, 2003). Arrivals from regional earthquakes do contain 1-5 Hz energy. Thus we remove the 0.7% of detections that are potentially coincident with arrivals of seismic phases from earthquakes present within the catalog of the Alaska Earthquake Information Center ($M_L > 1.5$, *D'Alessandro and Ruppert*, 2012). Remaining detections may result from iceberg calving at one of the other tidewater glaciers in or near Icy Bay (*O'Neel et al.*, 2010; *Richardson et al.*, 2010; *Bartholomaus et al.*, 2012), other glaciological phenomena (e.g., *West et al.*, 2010), or landslides (e.g., *Zimmer et al.*, 2012).

The second step is to distinguish Yahtse Glacier calving events from other seismogenic phenomena. We locate the remaining detections using the decay of seismic amplitudes (*Battaglia and Aki*, 2003; *Jones et al.*, 2013) and discard those distant from the Yahtse termi-

nus. We expect icequake amplitudes to decay according to

$$A_{obs}(r) = \frac{A_0}{r^n} exp(-\alpha r) \tag{4.1}$$

where $A_{obs}(r)$ is the maximum amplitude observed a distance r from the calving event, A_0 is the source amplitude, n is 1/2 for surface wave spreading of seismic energy or 1 for body wave spreading. The exponential decay coefficient is $\alpha = \pi f / Q\beta$, for which f is the frequency of the seismic signals, Q is the quality factor for attenuation, and β is the seismic wave speed (*Battaglia and Aki*, 2003; *Jones et al.*, 2013).

To identify appropriate values for n and α, we fit Eq. 4.1 to a subset of icequakes produced by calving events witnessed at the terminus of Yahtse Glacier. $A_{obs}(r)$ is the maximum amplitude of the Hilbert transformed waveform, filtered between 1 and 5 Hz, recorded at each of the stations within our network. We find that Eq. 4.1 is best fit with $n = 1$ and $\alpha = 0.005$ and use these values for all locations going forward. With $f = 3$ Hz (a typical icequake frequency) and $\beta = 1.9$ km s^{-1} the speed at which the maximum amplitude signal moves through the network, $Q = 100$.

Eq. 4.1 is poorly suited to inversion-based location methods typically used to identify earthquake epicenters using travel times. The $1/r^n$ term will yield local minima in an error surface, in addition to our preferred global minimum. However, the simplicity of Eq. 4.1 makes it well-suited to computationally-efficient grid searches with which we can map the complete error surface surrounding our network. Therefore, our location algorithm applies Eq. 4.1 to each node of a rectangular grid covering the area of Fig. 4.1 at 110 m spacing. The focal depth is set to zero. We assign the origin of a given seismic event to the location where the error function

$$\text{Err} = 100 \times \frac{\sum_{i=1}^{n} \left| A_{i,pre} - A_{i,obs} \right|}{\sum_{i=1}^{n} A_{i,obs}} \tag{4.2}$$

is minimized (Fig. 4.2). In Eq. 4.2, n is the number of stations, $A_{i,pre}$ is the amplitude predicted at station i using Eq. 4.1, and $A_{i,obs}$ is the amplitude observed at station i. This differs slightly from the error function used by both *Battaglia and Aki* (2003) and *Jones et al.* (2013) in that we use the L_1 norm to minimize the impact of undesirable, local, seismic sources that may act as outliers, such as rockfall, wind noise or calving at adjacent glaciers. The earlier authors used a L_2 norm version of Eq. 4.2 in their studies. For most seismic events, the form of the error function makes a small difference in the epicentral location– the difference between L_1 and L_2 norm locations for 93% of events is less than 2 km.

Figure 4.2 demonstrates an example in which the L_1 norm makes an important difference. In the set of waveforms presented (Fig. 4.2), we expect that the large-amplitude icequake recorded by most stations, including BOOM, LUPN, TRIP, and DOST, was produced by a single calving event at the terminus of Yahtse Glacier. This is the signal of interest that we seek with our measurements of A_{obs}. In Fig. 4.2a, we infer that the signal recorded at TARP is a local seismic event of unknown origin that acts as an outlier as we seek to find the minimum Eq. 4.2. The L_1 location (Figs. 4.2b and c) is not significantly perturbed by this outlier and the amplitude decay equation is smoothly fit through the remaining 8 values of A_{obs}. In the L_2 case (Figs. 4.2d and e), the origin is mislocated by 6.7 km as a result of the TARP outlier.

After locating each of the potential icequakes, we manually examined the origins, error surfaces and waveforms of 2000 arbitrarily-selected seismic events during a time when our complete, 9-station network was operational. Waveform examinations considered whether the peak amplitudes at each station appear generated by a consistent arrival's move-out or whether the peak amplitudes were contaminated by other sources, and whether the waveforms appeared similar to known Yahtse calving events. Based on these inspections, we identified each seismic event as the result of a Yahtse calving event or as generated by some other process (Fig. 4.1). Of the 2000 seismic events, 1455 were consistent with a Yahtse calving source. We mapped each of the 2000 events and delineated a region in which nearly all of these Yahtse calving icequakes located. Also present within this region were 30 (1.5%) false positives. 28 (1.4%) Yahtse calving events fell outside of the delineated region (i.e., false negatives).

To test the location algorithm's sensitivity to station dropout (which plagued our experiment during 2009 and early 2010), we individually dropped stations from our location algorithm and re-ran the 2000 analyst-reviewed origin locations. We find that the algorithm is relatively insensitive to the specific network configuration, and mislocation errors remain small. In an extreme case, with only 4 stations operational (1 month in 2009), we can expect 5% false positives and 19% false negatives. The densest cluster of locations remains concentrated at the Yahtse Glacier terminus.

Therefore, we use the automatic locations and delineated region to create a final 404,294 icequake catalog of non-earthquake seismic events produced by iceberg calving at the Yahtse Glacier terminus.

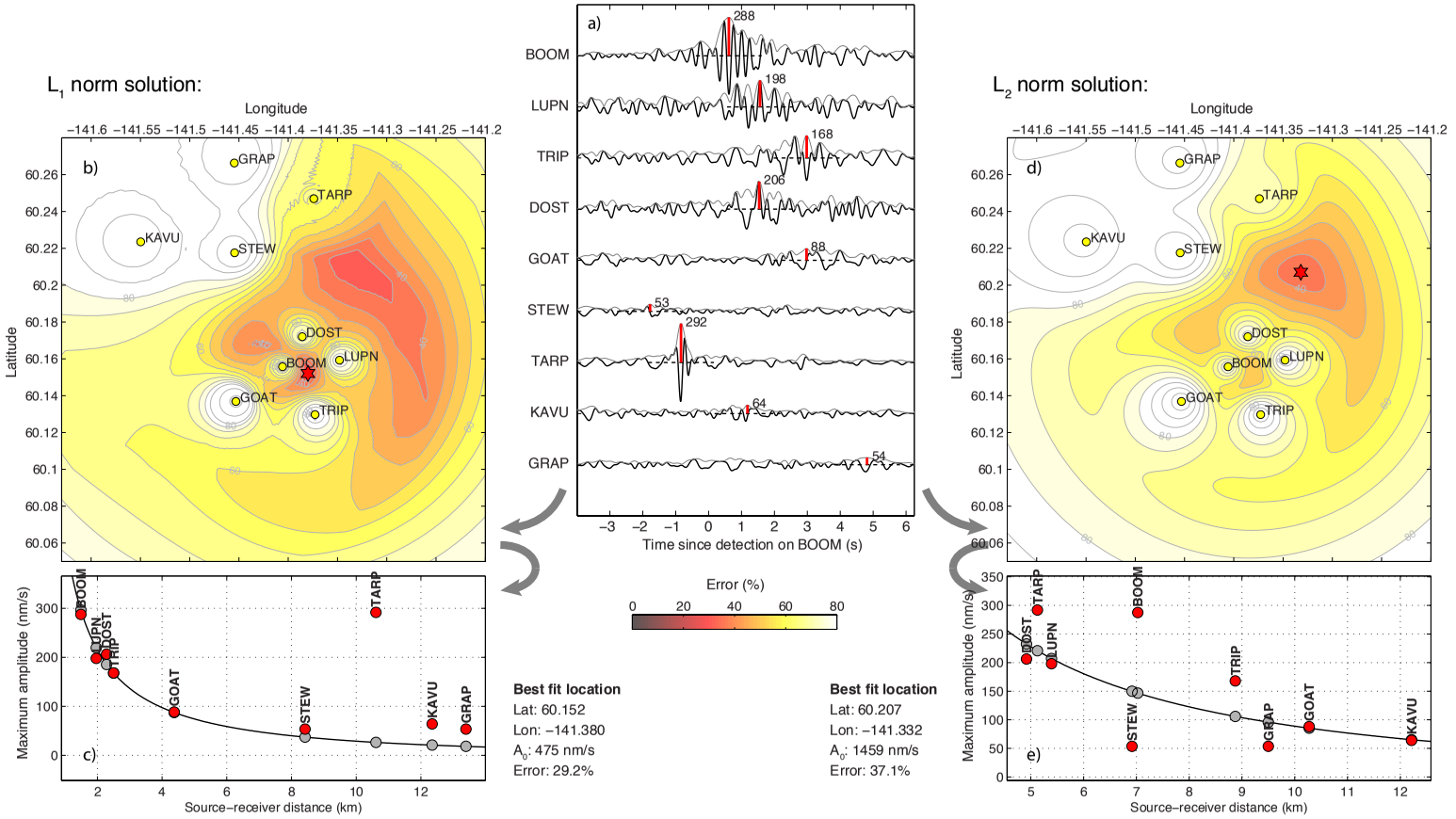

Figure 4.2. Input to and output from the amplitude-based location algorithm for one seismic event detected at BOOM. (a) 1-5 Hz filtered waveforms from the vertical channel of each station. All waveforms are scaled uniformly. The Hilbert transform of each waveform is in gray and the maximum amplitude of each waveform is identified with a red line and a number indicating the maximum recorded amplitude in nm/s. (b) The error surface calculated using Eq. 4.2 and the maximum amplitudes of panel (a). The best fit location is marked with a red star, where the error is smallest. (c) The observed (red) and predicted (gray) maximum amplitudes at each station for the best fit location of panel (b). (d) and (e) As for panels (b) and (c), but with an L_2 norm version of Eq. 4.2.

4.4.3 Icequake properties

For each of these icequakes we extract 13 different seismic properties from the waveforms recorded on the vertical channel of BOOM (Fig. 4.3). These are icequake duration (DUR, from the detector algorithm), maximum waveform amplitude (MAX), root mean squared amplitude (RMS), pseudo-energy (ENR, the integral over time of the squared amplitude of the Hilbert transformed waveform), inter-detection time since the last detection (TI1), 5 detections (TI5) and 20 detections ago (TI20), peak frequency of the icequake spectra (FREQ; > 1 Hz to ensure we are not measuring microseisms), and five icequake envelope shape properties. Visual observations paired with seismic data reveal that calving icequakes are produced by several-second-long, complicated, source processes (e.g., *Bartholomaus et al.*, 2012). When convolved with earth structure and instrument responses, long-duration icequake source-time functions lead to a wide variety of icequake shapes that generally lack the sharp *P*- and *S*-wave arrivals characteristic of most tectonic earthquakes (*Wolf and Davies*, 1986; *Stein and Wysession*, 2003).

To characterize icequake shape, we normalize the Hilbert transformed waveform in both time and amplitude and envision the transformed waveform as a probability density function (PDF) with x- and y-axes bound between 0 and 1 (Fig. 4.3c). From this PDF-envisioned waveform, we calculate the mean (MEAN), standard deviation (STD), skewness (SKEW), and kurtosis (KURT; roughly "peakedness") of the amplitude, as well as the normalized time of maximum amplitude (MODE). *Köhler et al.* (2012) have previously employed waveform standard deviation, skewness, and duration, among other properties, to classify seismic events as either calving-generated or originating from some other process. Here, we explore whether these properties can be used to further discriminate between larger and smaller calving events.

Our frequency domain detector identifies seismic events based on relative increases in power of the spectra between 1 and 5 Hz (*O'Neel et al.*, 2007). All detectors, including ours, that use a fixed signal to noise detection threshold will detect fewer icequakes when the seismic noise floor rises. At Yahtse Glacier, background seismic noise increases during summer months (Fig. 4.A.2). Fig. 4.A.3 shows how the temporal variation in background seismic noise appears to influence the rate of icequake detections.

To limit the possibility of inconsistent detection capability, we examine a frequency-MAX plot of the icequakes located at Yahtse Glacier, similar in concept to a frequency-

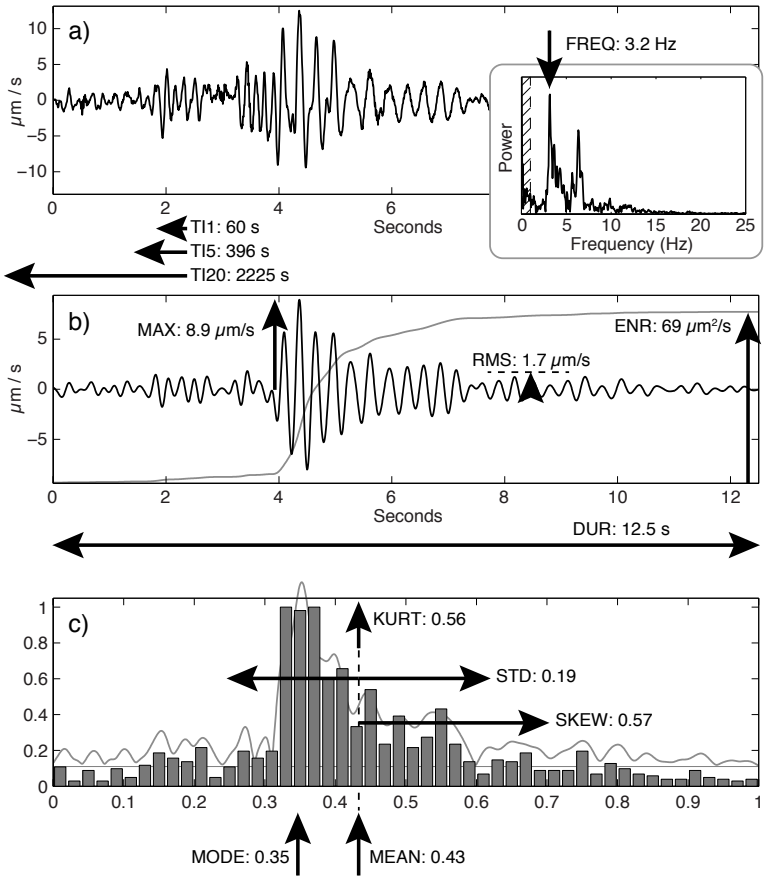

Figure 4.3. Illustration of the 13 icequake properties used to predict iceberg size labeled on a single, relatively simple icequake recorded at BOOM. a) Unfiltered waveform. b) Waveform filtered between 1 and 5 Hz. Cumulative squared amplitude of the waveform envelope (gray), the integral of which is ENR, shown according to different vertical scale in the background. c) Histogram derived from the Hilbert transform of the filtered waveform, plotted over the vertically-offset Hilbert transform.

magnitude plot demonstrating the Gutenberg-Richter relation of earthquake occurrence (Fig. 4.4) (*Gutenberg and Richter*, 1944). On log-log axes, the icequakes with maximum amplitude between 900 and 10,000 nm s^{-1} lie along a straight-line, suggestive of a power-law relationship. The occurrence of icequakes with maximum amplitudes less than 900 nm s^{-1} begins to fall off of this straight line, suggesting that 900 nm s^{-1} is the "amplitude of completeness" for our catalog (by analogy to a magnitude of completeness for earthquake catalogs, *D'Alessandro and Ruppert*, 2012). Thus, we have likely detected every icequake with a maximum amplitude greater than 900 nm s^{-1}, however, our detector may not detect icequakes with lower MAX. At amplitudes higher than 10,000 nm s^{-1}, the number of icequakes begin to deviate from the straight line of lower amplitude icequakes. This may indicate that more than one process is involved in the generation of seismic energy during iceberg calving (*Bartholomaus et al.*, 2012). Alternately, the generation of calving icequakes may not be a power law process.

In order to ensure that Yahtse Glacier calving icequakes are being detected consistently throughout the year, we discard those icequakes with MAX < 900 nm s^{-1}, approximately 50% of our catalog. The occurrence rate of these icequakes is shown in Fig. 4.5. After the model selection portion of our workflow, we will apply our preferred model to the remaining 215,150 consistently identifiable Yahtse Glacier icequakes. This will allow us to derive a time series of iceberg calving fluxes at Yahtse Glacier and examine variability in this time series.

4.4.4 Selection on an iceberg size predicting model

Having identified the icequakes produced by iceberg calving at Yahtse Glacier, we seek to estimate the size of the seismogenic iceberg. We accomplish this goal by associating icequakes with known calving events from the June 2010 observer record. Using the associated icequakes from this training period, we identify the most predictive statistical model of iceberg size using our 13 icequake properties. Our goal for model selection is prediction beyond the training period, physical insight into the importance and significance of the selected icequake properties, and model parsimony.

Icequakes are assumed to originate from an observed calving event if the two overlap in time with a 5 s buffer. This yields a training dataset of 892 events. The icequake properties and corresponding iceberg size are shown in each of the 13 panels of Fig. 4.6. These boxplots allow us to identify which predictors vary systematically as a function

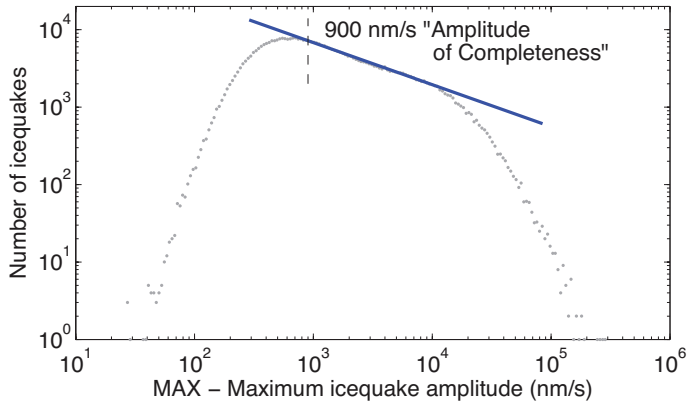

Figure 4.4. Frequency-maximum amplitude relationship for icequakes located at the terminus of Yahtse Glacier (binned logarithmically). Icequakes with moderate maximum amplitudes (MAX) lie along the blue straight line with log-log axes. Below 900 nm s^{-1}, the number of icequakes detected begins to deviate from this straight line.

of iceberg size. We cannot be confident that the distribution of predictor values differ among size classes for FREQ, MEAN, SKEW and TI20 ($\alpha = 0.05$ via the Kruskal-Wallis test). Furthermore, the relationships between iceberg size and STD, KURT and TI1 appear non-monotonic, significantly limiting their use as a predictor of iceberg size. We remove these 7 icequake properties from further consideration as potential regressors, leaving DUR, MAX, RMS, ENR, MODE, and TI5 that may be valuable predictors of iceberg size. To account for the non-linearity apparent in the relationships between iceberg size and DUR, MAX, RMS, and ENR (Fig. 4.6), we include in our model selection process the possibility that the square root of these icequake properties might be a better predictor than untransformed versions. Thus we proceed with 10 candidate regressors: 6 original icequake properties and 4 square root transformed properties.

Our 892-observation training dataset has an exponentially distributed response variable (iceberg size), and the assumptions of normally distributed model errors with constant variance are not met in our case by linear regression models with least squares estimates of model coefficients. Generalized linear models (GLMs) are an alternate approach to estimating model coefficients that do not require these conditions on the data or residuals (*Montgomery et al.*, 2001; *Crawley*, 2009). Thus, to identify a linear relationship between icequake properties and the size of the iceberg that generated the icequake, we use a GLM with a gamma error distribution and a $1/\sqrt{y}$ link function. The link function describes

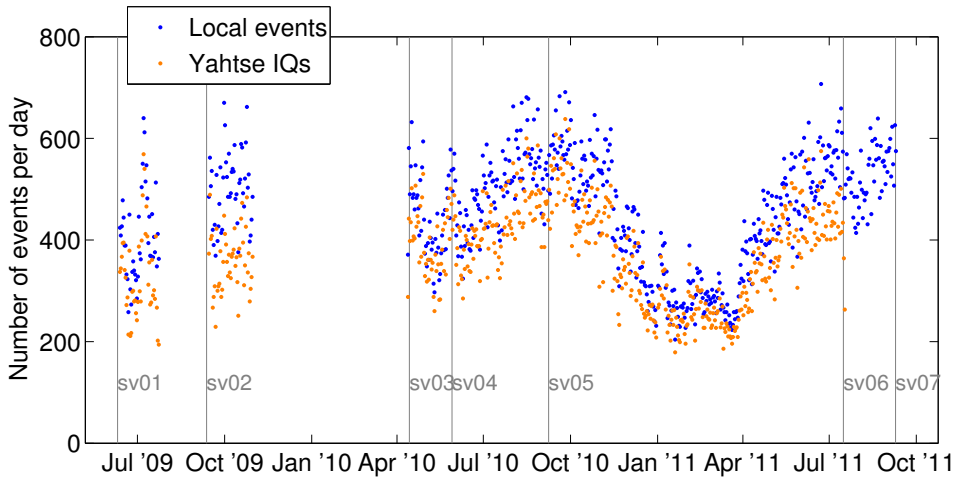

Figure 4.5. The number of seismic events detected and located per day (not including AEIC earthquakes). Blue circles are all non-earthquake events recorded by our network; orange circles are a subset of this group: just those events at the Yahtse Glacier terminus. The ratio of these two event rates is shown below, in the next figure. As with all other time series derived from icequake properties, icequakes with MAX < 900 have been excluded from this figure. The times of 7 service runs are indicated with vertical gray lines.

the relationship between the linear predictor (sum of regressors multiplied by their coefficients) and the response variable (*Montgomery et al.*, 2001; *Crawley*, 2009). The inverse square root link yielded a better model fit than identity, log, or reciprocal link functions.

With 10 candidate regressors, we construct $2^{10} = 1024$ differerent models, where each model represents a different subset of the complete 10 regressor model. Because prediction is our first goal, we assess the performance of each of these 1024 models using 5-fold cross-validation (*Montgomery et al.*, 2001). For each fold of each model, a random 5th of the observations are withheld for testing and coefficients are fit to the remaining 4/5ths of the observations. These coefficients are then applied to the withheld regressors and we calculate the prediction root mean squared error (RMSE) for the fold (where the error is the difference between the predicted and the observed response). This process is repeated for each of the remaining 4 folds, then each model is ranked according to the mean RMSE of the five folds. However, the coefficients of the lowest RMSE model are not necessarily all significant, and multicollinearity among the regressors can lead to coefficients that are highly sensitive to small perturbations in icequake properties (*Montgomery et al.*, 2001). Therefore, from the ranked models, we select the one with the lowest cross-

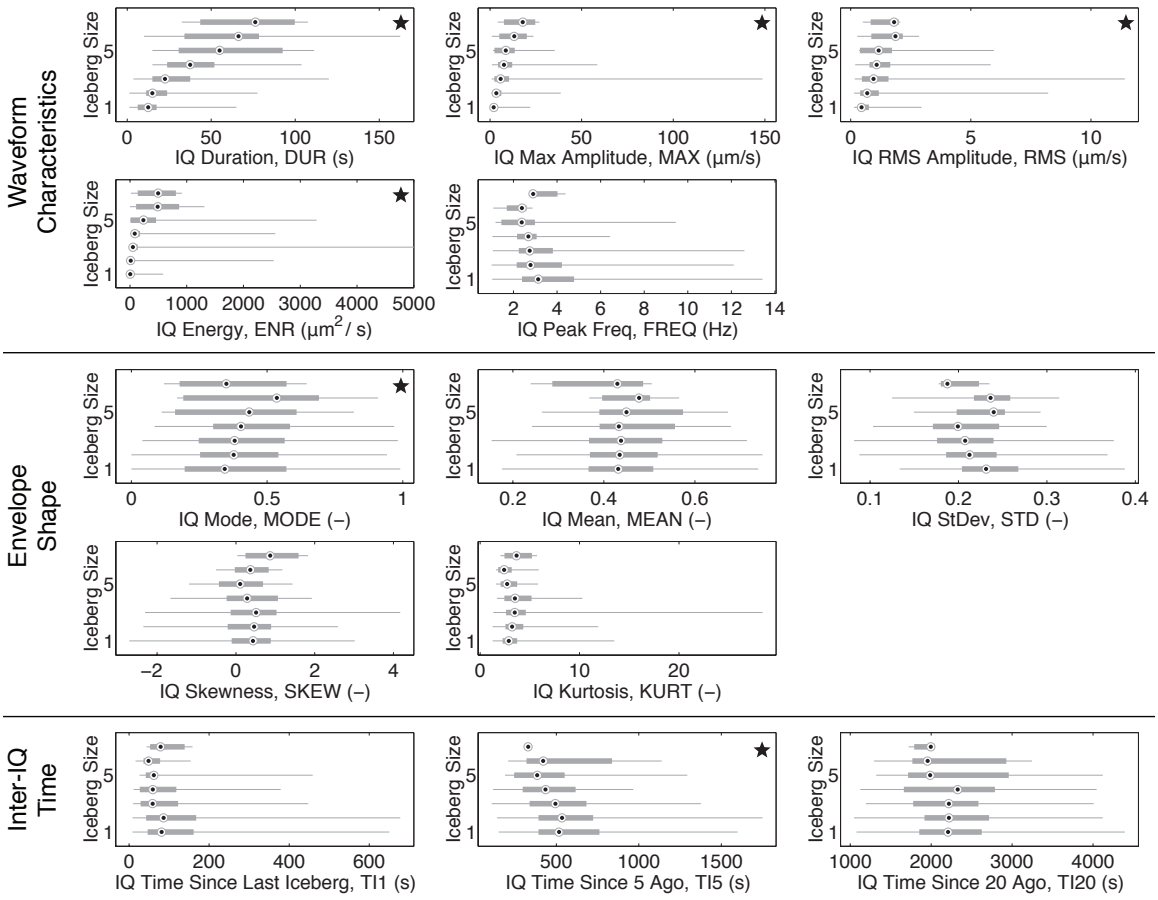

Figure 4.6. Boxplots showing relationships between icequake (IQ) properties and iceberg size for 892 observed calving events. The values for each iceberg size class of each icequake property are represented as horizontal boxes. The median property value for each size class is shown with the small bullseye. Wide gray bars extend across the interquartile range (IQR) from the 25th to the 75th percentile values. Thin lines span the remainder of the data. Stars mark 6 IQ properties included in the model selection process. Non-starred properties exhibit no systematic relationship with iceberg size.

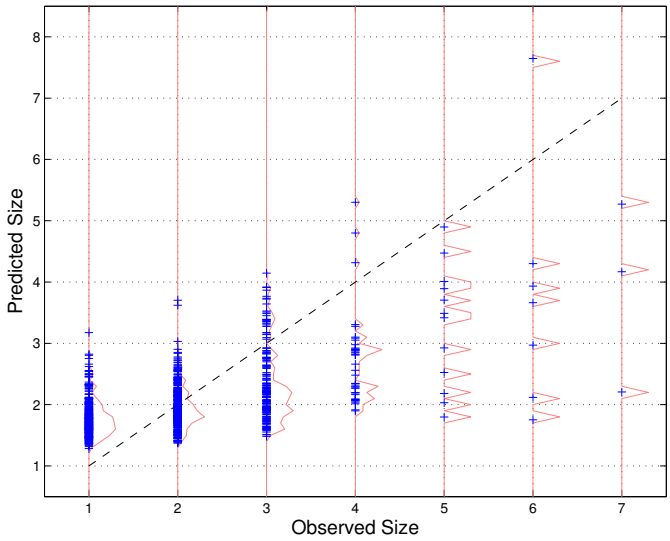

Figure 4.7. Observed and predicted iceberg sizes for each calving event in our training dataset. The difference between these quantities are the model residuals. Red lines represent empirical iceberg size density functions of the predicted sizes, so that the structure of the size distributions can be visualized when the iceberg/icequake observations plot on top of each other. symbols identify individual calving observations. The model overestimates the size of small (size 1) icebergs, and underestimates the size of large icebergs (those greater than size 2). With a perfect model, observed and predicted sizes of each iceberg would be identical and all icebergs would fall on the dashed 1:1 line.

validated RMSE for which all coefficients are significant at the 95% confidence level and have a variance inflation factor < 5).

The selected model includes the square root of icequake duration (DUR), the square root of icequake root mean squared amplitude (RMS), time since 5 icequakes ago (TI5), and the icequake mode (MODE). We present this model in Table 4.1. In addition to other statistics, we report the deviance explained by the model, a goodness-of-fit metric. The proportion of deviance explained is analogous to the R^2 of general linear models and is computed as the difference between the deviance of the null model (i.e., that model consisting only of a constant term) and the deviance of the fitted model, divided by the deviance of the null model. A comparison between the observed and the modeled iceberg sizes is shown in Fig. 4.7. An additional set of figures illustrating model performance are presented in Appendix 4.B.

The p-value for the duration coefficient is the lowest of the coefficients included in our model and the lowest among the 13 potential regressors in univariate regression; visually,

Table 4.1. Statistics for the preferred generalized linear model with a gamma error distribution. SE is standard error of the coefficient estimate. Note that a negative coefficient indicates a positive correlation between the icequake property and iceberg size due to the inverse square root link function.

$$\frac{1}{\text{Size}^{1/2}} = \beta_0 + \beta_1 \text{DUR}^{1/2} + \beta_2 \text{RMS}^{1/2} + \beta_3 \text{MODE} + \beta_4 \text{TI5}$$

Estimated coefficients:

		Estimate	SE	t Statistic	p-Value
β_0	(Intercept)	0.93	0.021	44	0
β_1	($\text{DUR}^{1/2}$)	-0.039	0.0029	-14	$< 10^{-37}$
β_2	($\text{RMS}^{1/2}$)	-0.058	0.013	-4.4	$< 10^{-4}$
β_3	(MODE)	-0.055	0.022	-2.5	0.014
β_5	(TI5)	4.1×10^{-5}	1.8×10^{-5}	2.3	0.023

Root mean squared error of cross-validation: 0.87

Deviance explained by model: 27%

p-value for complete model: $< 1 \times 10^{-58}$

the relationship between duration and iceberg size is more clear than any other relationship (Fig. 4.6). Therefore we also identify the univariate GLM for this most predictive, single-regressor model:

$$\frac{1}{\text{Size}^{1/2}} = 0.91 - 0.045\text{DUR}^{1/2} \tag{4.3}$$

This model has only a slight loss in performance when compared with the preferred, four-regressor model: its cross-validation RMSE is 0.87. Thus, a 5 s icequake is predicted to be generated by a size 1.5 iceberg, a 30 s icequake is produced by a size 2.3 iceberg, and a 90 s icequake is produced by a size 4.4 iceberg.

4.4.5 Converting iceberg size classes to volumes

During our observer period, we qualitatively estimated the sizes of calved icebergs by scaling them against the surveyed, 60-m height of the glacier terminus. In-person observers were trained to promote consistent size delineation; iceberg size classes are likely accurate to within 1 unit. While in the field, we estimated the volume of a typical iceberg for each of the 7 classes. These estimates are well-fit by

$$\text{Volume} \approx 700(\text{Size})^3 \qquad [\text{m}^3]. \tag{4.4}$$

The particular form of the relationship is uncertain, nor are we able to place quantitative confidence intervals on its coefficients. However, we have some satisfaction by the appearance of the third power, consistent with our size estimates being a length scale.

4.4.6 Model application to complete icequake record

With an icequake-iceberg size model selected according to the training dataset, we then apply it to the icequake properties of our complete, 18-month record. Our model predicts a very small number of extremely large icebergs, well beyond the largest calving events observed in person ($< 0.1\%$ of the number of Yahtse calving icequakes result in a predicted size > 9). Extremely large calving events, that involve more than approximately 10% of the width of the glacier terminus, are also not apparent in time lapse photography of the glacier terminus. Spot checking of several of these extremely large size events revealed that they result from long-duration detections in which multiple distinct icequakes occurring over several minutes are identified as a single detection. Thus, we remove these rare, inaccurately-sized calving events from the record. Finally, we apply Eq. 4.4 to each

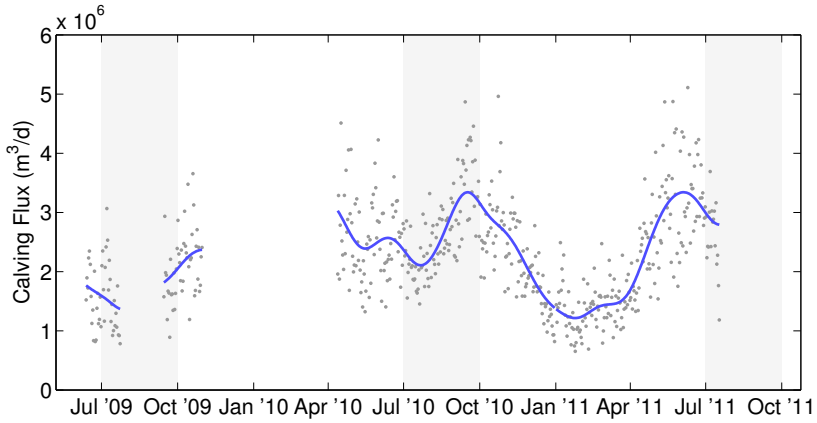

Figure 4.8. Daily calving flux at Yahtse Glacier calculated by applying Eq. 4.4 to the statistical iceberg size predictions (Table 4.1) and summing individual iceberg volumes by day. Blue line is a 2 month low pass filtered version of the calving flux time series. Gaps in the record are the result of station outages. Light gray shading indicates time periods with elevated background seismic noise, during which calving fluxes may be underestimated.

estimated iceberg size, then sum each volume estimate by day to derive a time series of calving fluxes from Yahtse Glacier (Figs. 4.8 and 4.9).

4.5 Discussion of results

4.5.1 Statistical modeling of calving volume with icequake properties

4.5.1.1 Model performance

Our statistical model predicts the span of observed iceberg sizes and with zero mean residuals. Larger observed icebergs are predicted to be larger than smaller observed icebergs (Fig. 4.7). For example, known size 3 icebergs are predicted to be larger, on average, than known size 2 icebergs. The RMSE of predictions for which the observed iceberg size is known, but their associated icequake properties were not used in model fitting (i.e., cross-validation), is 0.87. This is similar to the precision of our qualitative iceberg size scale. The derived calving fluxes during our training period range between 1.4 and 3.0×10^6 m^3 d^{-1}, a significant portion of the 0.7 to 5.3×10^6 m^3 d^{-1} complete range of daily calving fluxes identified during . This increases the likelihood that our model, tuned during 12 days in June 2010, is reliable across the full range of observed calving fluxes. Thus, we are reassured that the preferred model is performing satisfactorily.

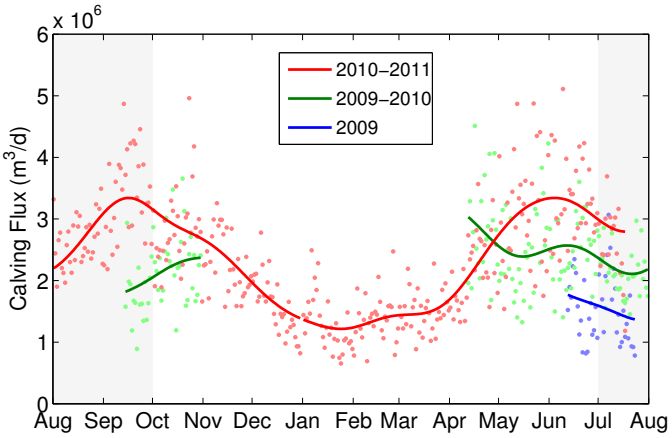

Figure 4.9. Daily calving flux as in Fig. 4.8, wrapped around one year. Time series of calving flux has been wrapped around from August 1 to August 1 to facilitate comparison among years. The choice of the August 1 break point is arbitrary.

However, the relationships between icequake properties and iceberg size are complex (Fig. 4.6), and this complexity is manifest in several model shortcomings. For example, the median duration for each iceberg size class increases with iceberg size, but large icebergs can also generate short icequakes and small icebergs can generate long icequakes. As a result of this data complexity, our preferred model overpredicts the sizes of small icebergs and underpredicts the sizes of large icebergs (Fig. 4.B.3). The number of size 1 icebergs is significantly underestimated. Because this stems from the underlying data used to build our model, these feature were present in all models that we tested.

Duration is the most statistically significant regressor and the scatter present in the relationship between icequake duration and iceberg size cannot be explained by any additional regressor or combination of regressors (Fig. 4.10). The preferred model (Table 4.1) explains 27% of the deviance in observed iceberg sizes; 73% is unexplained. A particular challenge for our modeling is the limited size range of calving events at Yahtse Glacier. No calving events with volumes $> 1 \times 10^6$ m^3 have been observed at Yahtse Glacier. If the size range present within our training data were greater, we might be able to better calibrate our statistical model.

Iceberg calving style (i.e., whether a calving event consists of a loose avalanche of ice debris or a discrete topple, drop, or submarine release) might also be an important source of error in our model. *Bartholomaus et al.* (2012) argued that calving style and the shape

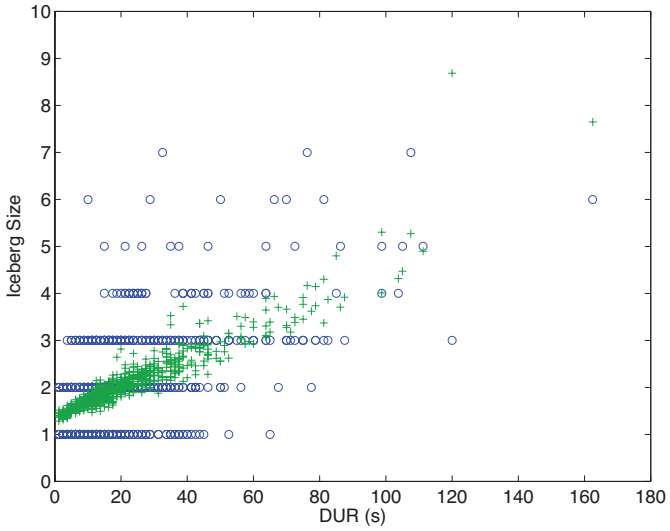

Figure 4.10. Iceberg size as a function of icequake duration DUR, the most significant regressor. Blue circles represent the observed iceberg sizes of the model training period. Green '+'s represent the modeled (Table 4.1) iceberg sizes, generated using the same set of predictive observations as the blue circles.

of the iceberg significantly modulate the character of the icequake produced by a calving event. Calving style was recorded during the observer period. In a future study, calving style could be included as a random effect through a linear mixed effects model (*Montgomery et al.*, 2001), in order to quantitatively assess how important calving style is for the estimation of iceberg size. We hypothesize that a mixed model would significantly increase the amount of variance explained by a statistical model. While a mixed model might improve our understanding of calving seismogenesis, it has limited benefit in terms of automated calving flux estimation because there is not yet any way to identify calving style without visual observations.

Despite these limitations, our application of a statistical model for the estimation of iceberg sizes and calving flux from icequake properties represents a significant improvement in our ability to observe iceberg calving. Not only do seismic methods allow for the consistent identification of calving, our linear model constructed of statistically significant (p-values < 0.05) icequake regressors is able to reliably predict iceberg size (RMSE < 1 size unit).

4.5.1.2 Relationships between icequake properties and iceberg size

Our statistical model provides support for the findings of previous studies that found icequake duration was a significant predictor of iceberg size and calving flux (*Qamar*, 1988; *O'Neel et al.*, 2007). None of the icequake properties included in this study have more explanatory power than duration, although the square root of duration was a better fit to our observations than untransformed duration (Fig. 4.6 and Table 4.1). This result is consistent with our experience in the field. The largest iceberg calving events evolve over long time periods. Smaller calving events tend to conclude quickly.

The icequake predictors that include waveform amplitude (MAX, RMS, and ENR) have moderate explanatory power, and tend to increase with increasing iceberg size. However, their relationship with iceberg size is not nearly as strong as that of icequake duration; the p-value for $\mathrm{RMS}^{1/2}$ in our preferred model is several tens of orders of magnitude greater than that for $\mathrm{DUR}^{1/2}$. This is consistent with our finding that the generation of icequakes is in part controlled by how an iceberg enters the sea (*Bartholomaus et al.*, 2012). Broad-faced icebergs that enter the sea at high speeds produce large splashes and air cavities that subsequently collapse, generating large amplitude icequakes. Large icebergs that detach from the glacier terminus at or below sea level are unlikely to generate cavities and may not necessarily produce large amplitude icequakes. These findings are in line with other studies that found no clear relationship between icequake amplitude and iceberg size (*Qamar*, 1988; *O'Neel et al.*, 2007).

However, we do find some relationship between the three amplitude-based properties and iceberg size. Larger icebergs may generate larger seismogenic cavities. Seismic energy is also produced when icebergs abruptly transfer momentum to the water surface (known as slamming, *Miloh*, 1991). More massive icebergs may slam with greater momentum onto the water, as well as experience greater drag force within the water; these processes could also lead to a positive correlation with iceberg size. None of the three amplitude properties is clearly a stronger predictor than the others; they could be substituted for each other into the preferred model with only a slight loss in predictive ability. Our efforts to reduce multicollinearity during the model selection process generally prevent more than one of these predictors from appearing together in the preferred model (Fig. 4.B.7).

Time since 5 calving events (TI5) and time of icequake mode (MODE) are the last two predictors in our statistical model. Each of the three TI properties is negatively correlated

with iceberg size, indicating that larger calving events are more likely during particularly "active" times at the terminus, when calving events occur frequently. Again, this view of calving occurrence is supported by our field observations. Hours or days would pass with relatively little calving activity, then the calving rate would build to the eventual release of much larger icebergs (Fig. 3 of *Bartholomaus et al.*, 2012). This is consistent with a view of calving in which smaller cracks proliferate and fuse under constant stress gradients, generating smaller calving events. These minor cracks eventually combine to form the runaway fracture that culminates in the calving of a large iceberg (*Faillettaz et al.*, 2011).

There is a positive, but weak, correlation between MODE and iceberg size. The amplitude of size 1 icequakes most frequently peaks 1/3 of the way through the icequake's duration (MODE = 0.33, Fig. 4.6 and Table 4.1). As iceberg size increases, there is a tendency for the peak amplitude to shift toward the mid-point of the icequake (MODE = 0.5). The tendency for MODE < 0.5 with small iceberg sizes may be a product of the simply shaped icequakes produced by these small calving events. These simple icequakes have a single maximum in amplitude early during the icequake and a coda that is relatively long in comparison with the total icequake duration. A consistent picture is revealed in the positive skewness of most icequakes (Fig. 4.6; see Fig. 4.3 for an example). The approach of MODE towards 0.5 with increasing iceberg size may reflect increasingly complex icequakes, with multiple peaks throughout the icequake duration, and a decreasing length of the icequake coda relative to the total icequake duration. However, we note that MODE and DUR are uncorrelated, which increases the value of including both regressors in the model (Fig. 4.B.7).

The relationship between peak icequake frequency (FREQ) and size is weak. Regardless of the iceberg size, the median peak frequency is between 2.4 and 3.1 Hz. The IQR for each size class spans between 1.5 and 4.7 Hz. We had previously suggested that icequake frequency should be negatively correlated with iceberg height and impacting surface area (i.e., iceberg size), and positively correlated with fall height (*Bartholomaus et al.*, 2012). Scatter within the present data prevent us from either supporting or contradicting the proposed relationship between iceberg size and icequake frequency. However, our findings do lend strong support to the use of frequency content for the discrimination of icequake source mechanisms (*O'Neel et al.*, 2007; *West et al.*, 2010; *Köhler et al.*, 2012).

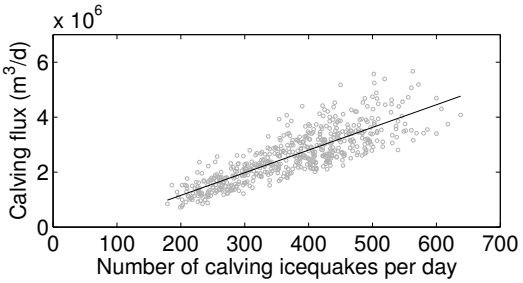

Figure 4.11. Relationship between icequake occurrence rate and calving flux. Estimated calving flux is based on properties of Yahtse Glacier icequakes detected at BOOM (gray circles). The best fit line through these 550 daily estimates (Eq. 4.5) is plotted in black.

4.5.2 Variations in calving flux at Yahtse Glacier

The calving flux varies at a range of time scales, along with the icequake occurrence rate. Calving flux and icequake occurrence are highly correlated ($r = 0.84$) and the calving flux derived through our icequake statistical model can be predicted with the icequake occurrence rate,

$$Q = 8242n - 4.9 \times 10^5 \tag{4.5}$$

in which Q is the calving flux (m^3 d^{-1}) and n is the number of icequakes per day (Fig. 4.11, $R^2 = 0.70$). In the sections that follow, we discuss the mean calving flux and how that calving flux varies with time.

4.5.2.1 Mean flux

Over the 550 days during which we recorded calving icequakes between June 2009 and July 2011, the estimated mean calving flux at Yahtse Glacier is 2.6×10^6 m^3 d^{-1}. We note that this calving estimate draws on only half the number of detected icequakes–those with a maximum amplitude greater than 900 nm s^{-1}. However, we expect that we have included nearly all of the largest volume calving events.

Calving flux $Q = w \times h \times u$, where w is the width of the terminus, h is the thickness of the terminus involved in calving (not submarine melting), and u is the mean ice flow speed at the terminus. The terminus of Yahtse Glacier is 2.5 km wide, thus, the product of h and u is 1030 m^2 d^{-1}. Neither of these terms are well-known, however we have estimated that u is close to 17 m d^{-1} (*Bartholomaus et al.*, 2013). If so, then the glacier thickness involved in iceberg calving is 61 m; comparable to the height of the glacier above sea level. By

this calculation, the remainder of the glacier thickness (that portion below sea level) must be removed by submarine melt; analysis of oceanographic data has similarly concluded that submarine melt is a large component of the total mass loss at the glacier terminus (*Bartholomaus et al.*, 2013).

Burgess et al. (2013) and *McNabb* (2013) offer two independent estimates of the sum of iceberg calving and submarine melt (known as frontal ablation) at Yahtse Glacier. *Burgess et al.* (2013) draw on velocity observations from mid-winter, whereas *McNabb* (2013) uses annual mean speeds. Both studies estimate that the frontal ablation rate is 3.0×10^6 m^3 d^{-1}, slightly larger than our estimate for calving alone. This would imply that the product of u and the terminus averaged ice thickness H is 1200 m^2 d^{-1}. If again $u = 17$ m d^{-1}, then we find $H = 71$ m. The surveyed terminus height is ~ 60 m–this implies that the glacier is grounded in only 10 m of water. By extrapolating bathymetric measurements from 1.5 km distant from the terminus, we estimate that the Yahtse Glacier terminates in water up to 110 m deep, although we have no clear way to place a shallow bound on this depth. If the *Burgess et al.* (2013) and *McNabb* (2013) estimates of frontal ablation are correct, and terminus water depth is 110 m, then $u = 6.5$ m d^{-1}, far below our 17 m d^{-1} measurement of the mid-terminus ice speed. This inconsistency may stem from the location where *Burgess et al.* (2013) and *McNabb* (2013) derive their frontal ablation estimates: > 5 km from the glacier terminus, where there is significant uncertainty in the ice thickness. Therefore, we suggest that they may have underestimated frontal ablation at Yahtse Glacier. However, neither their estimates of frontal ablation rate nor our estimates of calving flux are so well constrained as to warrant complete confidence in any one set of results. The ice thickness at the glacier terminus is uncertain and the absolute magnitude of our calving fluxes are the least constrained part of our results.

The mean size of icebergs calved on a given day is the day's flux divided by the day's total number of calving events (i.e., icequakes). The mean iceberg size over the entire observation period is 6800 m^3, but our calculation reveals substantial deviations from this mean (Fig. 4.12). The clearest pattern present within this record is an approximately two month period in July and August 2010 when the iceberg sizes were estimated to be consistently below average. Our results suggest a similar dip may be present during the summers of 2009 and 2011 as well. Each of these time periods coincides with the summer increase in seismic noise. The onset of seismic noise and the decrease in iceberg size are similarly abrupt. This leads us to suggest that the decrease in mean iceberg size may be related to

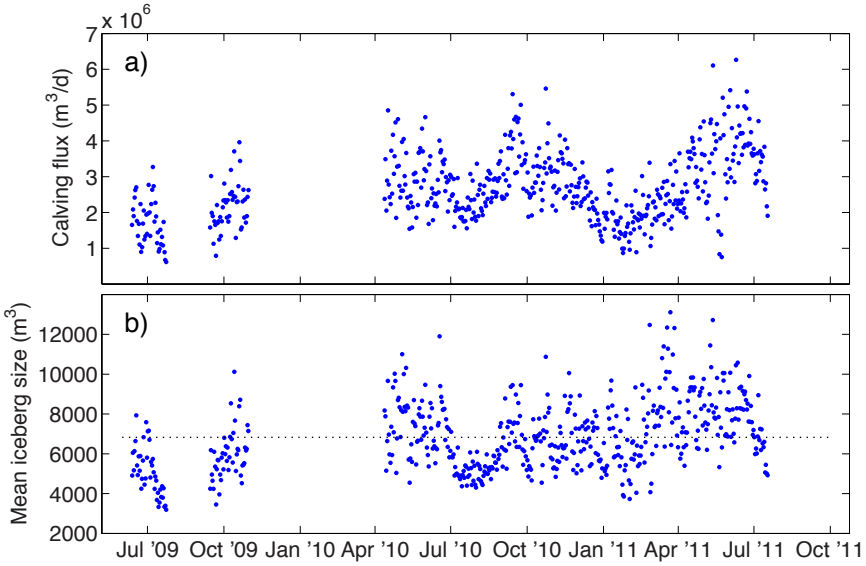

Figure 4.12. Calving fluxes and mean iceberg sizes as a function of time. a) Estimated calving flux as in Fig. 4.8. b) Mean daily iceberg size. The dotted line indicates the mean over the entire experiment.

a decrease in the mean DUR of detected icequakes. While our amplitude threshold (Fig. 4.4) provides some assurance that we are detecting icequakes consistently, elevated background noise may decrease detected durations (i.e., the duration during which the amplitude of the seismic event rises by some factor above the background amplitude). Duration is the most important predictor of iceberg size (Table 4.1), so when the icequake durations decrease, the predicted sizes will follow suite.

We note that the decrease in mean iceberg size coincides with a decrease in calving flux (Fig. 4.12a). Because we are not able to rule out the possibility that these decreases are the result of elevated seismic noise levels and not the result of the iceberg calving process, we place low confidence in the estimated calving flux during these July-September time periods. These times are shaded light gray in Figs. 4.8 and 4.9. Calving flux may potentially remain constant through the May-October period, or even increase; we cannot be certain. We observe only small changes in mean iceberg size during non-summer portions of the year, and place high confidence in the winter decrease in calving flux shown from December 2010 through to April 2011 (Fig. 4.12a).

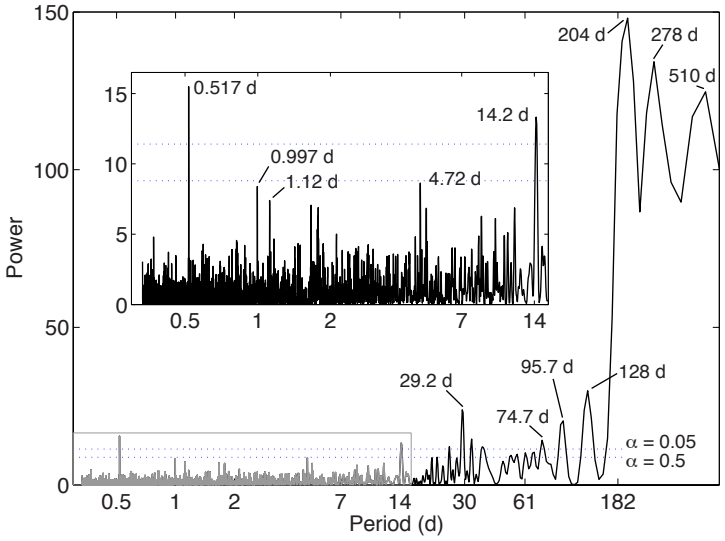

Figure 4.13. Power spectrum of iceberg calving flux calculated by applying the Lomb-Scargle algorithm to the demeaned, detrended calving flux in 4-hr bins. Significance thresholds are shown with dotted lines and labeled with α values. The periods of several prominent peaks are labeled. Inset shows a larger-scaled version of the short-period power from the gray box; axes are the same as larger panel.

4.5.2.2 Tidally driven variations in calving flux

Due to the limitations of our statistical model, we have higher confidence in the variability that we observe, than we do in the absolute magnitudes of the calculated calving flux. Around the mean rate of 2.6×10^6 m^3 d^{-1}, we find variability in the calving flux at a range of time scales. Gaps in the calving flux record prevent application of typical fast Fourier transform algorithms to quantify the strength of periodicity within the calving flux records. The Lomb-Scargle algorithm is an alternative for calculating power spectra that is well-suited to irregularly spaced data (*Press et al.*, 1992). Therefore, we sum our iceberg volume estimates by 4-hr bins, implement the Lomb-Scargle algorithm, and present the results in Fig. 4.13. Larger or smaller bin choices have only a small effect on peaks. The strongest periodicity present within the Lomb-Scargle periodogram is that at very long periods, those > 150 d. However, these periods are affected by the duration of the record, data gaps, and the questionable summer decrease in calving rate. We do not consider them further.

Among the other peaks of the periodogram are 0.52, 1.0, 1.1, 14.2, and 29.2 d periods. These are similar or identical to the periods of the following tidal constituents: principal lunar semidiurnal (M_2, 0.518 d), principal lunisolar diurnal (K_1, 0.997 d), principal lunar

diurnal (O_1, 1.08 d), fortnightly (M_f, 13.7 d) and monthly (M_m, 27.6 d). The power at semidiurnal, fortnightly and monthly periods is significant at $\alpha = 0.05$.

To further explore the role of ocean tides and calving activity, we identified the tidal stage during which 100,000 calving icequakes occurred. For the tides, we used a National Oceanic and Atmospheric Administration tidal model for upper Icy Bay (station 9453431) and identified high and low tide calving as that which occurs within an hour of either tide. Otherwise, calving occurs during rising or falling tides. We find that tidal stage has a large effect on the calving rate for size 2 icebergs (the most frequent predicted size); the effect is smaller or less clear for other iceberg sizes. Calving is slightly more frequent during low and falling tides than it is during high and rising tides. Calving at low tide (17.3 events per hour) is 4% more frequent than the mean rate (16.6 events per hour) for size 2 icebergs.

Previous examinations of the influence of tides on iceberg calving have found mixed results. Fortnightly variability in calving has been found in some cases (*O'Neel et al.*, 2003), but not others (*O'Neel et al.*, 2010). None of the studies reviewed have identified either semidiurnal or monthly calving variability (*Qamar*, 1988; *O'Neel et al.*, 2003, 2007, 2010). *Warren et al.* (1995) described "weak" connections between tides and calving. In Greenland, studies to date have focused on the largest, approximately weekly, calving events that generate glacial earthquakes, to the exclusion of the more common, smaller calving events that we describe in this study. Observation of significant power at the periods of multiple harmonic constituents appears to be unique to this study. However, we cannot rule out the possibility that calving periodicity was present at these other sites, but unidentified. Several of the studies cited lack a seismic record with which to make these quantitative, high temporal resolution analyses. It is also possible that tidal variability is restricted only to small calving events that are unidentified by regional seismic networks. For example, *O'Neel et al.* (2010), working in the same Icy Bay region, identified an average of one icequake at Yahtse per 40 minutes, compared with the roughly one per 2 minutes of the present study.

If the contrasts in tidal sensitivity are true and not the result of differences in resolving power among studies, we propose the following explanation. Yahtse terminates in water that is significantly more shallow than that at Columbia or LeConte Glaciers, although the height of the terminus above sea level is comparable to that of the other two glaciers (*O'Neel et al.*, 2003, 2007). Thus, the normal stress at the bed of Yahtse Glacier is greater than in the other two cases. The process by which tides modulate calving at Yahtse Glacier

is unlikely to be through flotation, at least not to the same degree as elsewhere. Instead, we propose that the normal stress applied back against the glacier terminus is the essential factor that sets the calving sensitivity to tides.

While both LeConte Glacier and Yahtse Glacier are similarly crevassed as they flow steeply down from high elevation accumulation areas, retreating LeConte Glacier terminates in a 250 m deep fjord, more than twice as deep as the estimated water depth at advancing Yahtse Glacier (*Bartholomaus et al.*, 2013; *Motyka et al.*, 2013). Throughout most of Columbia Glacier's multi-decade retreat, it also terminated in several hundred meter deep water (*McNabb et al.*, 2012). Thus the relative variation in normal stress applied by tidal fluctuations are greater at Yahtse Glacier than they are at either LeConte or Columbia Glaciers. We suggest that this greater relative size of tidal fluctuation may result in greater sensitivity to tidal stage. This contrast might also control the occurrence rate and size distribution of calving events at Yahtse Glacier. The 3 m tidal range may control relatively large amplitude variation in the force balance at the glacier terminus (at multiple tidal periods), leading to frequent, smaller-sized calving events. This hypothesis is consistent with field observations that calving at Yahtse Glacier is both more rapid, and smaller-sized than calving at either LeConte or Columbia Glaciers.

4.5.2.3 Calving variability at periods > 1 month

Outside of the July-September period, the clearest pattern in calving flux is the 50% decrease in calving flux from December through March, during a time period with minimal seismic noise and excellent seismic station performace. Seasonal variations in terminus position are commonly observed (e.g. *Krimmel and Vaughn*, 1987; *Ritchie et al.*, 2008; *Schild and Hamilton*, 2013), with termini advancing through the winter and retreating during the summer. In Greenland, these variations have been attributed to decreased calving as a result of a backstress applied to the terminus by rigid ice mélange (*Amundson et al.*, 2010). However, mélange formation is very rare at the termini of Alaskan tidewater glaciers. It is not yet clear as to whether winter advance of the terminus is the result of a decrease in calving or an increase in ice flow speed; winter observations of tidewater glacier termini are rare. The winter minimum in iceberg calving that we observe suggests that, at Yahtse, the decrease in calving flux is likely to be a major factor in the annual, 200-300 m winter advances of Yahtse Glacier (*McNabb*, 2013).

Previous studies of calving seismicity, including of the area surrounding Yahtse Glacier, have observed maxima during late August through October (*O'Neel et al.*, 2010; *Köhler et al.*, 2012). The present results support these findings, particularly if we adopt a view of calving variability with an even longer-period low-pass cutoff than that used in Fig. 4.8 and 4.9, and smooth over the summer drops in calving flux (gray shading of Fig. 4.8). We propose that the fall increase in calving is driven in large part by rapid undercutting of the grounded terminus by submarine melt. Submarine melt is facilitated by both warm seawater and vigorous subglacial discharge (*Jenkins*, 2011; *Xu et al.*, 2012; *Motyka et al.*, 2013). Both of these conditions are met during the fall (*Bartholomaus et al.*, 2013). Furthermore, the terminus is at an extended, summer position, perhaps somewhat beyond the submarine moraine against which Yahtse Glacier presently terminates (*Bartholomaus et al.*, 2012).

In light of rapid submarine melt and an exposed terminus position, we suggest that the fall increase in iceberg calving that we and previous authors report is largely governed by undercutting of the terminus and collapse of unstable, subaerial seracs, rather than by some internal dynamic process. Following on the late summer/fall condition, we suggest that the winter minimum in calving results from minimum rates of submarine melt (*Bartholomaus et al.*, 2013) and a retracted terminus position, perhaps protected by a submarine terminal moraine.

4.5.2.4 Non-tidal, multi-day variability

In addition to tidally-forced and longer period variations in calving flux, we also observe weak 4.7 day periodicity and other high-frequency variability. Several-day periodicity was also described by *O'Neel et al.* (2007) and *O'Neel et al.* (2010). These authors proposed that several-day periodicity was the result either of the regular passing of storms or of an internal, self-regulating forcing, likely also related to glacier hydrology. We are unable to offer a better explanation for this pattern and note that this peak in power may be spurious, as it has low significance ($\alpha \sim 0.5$).

We explore higher frequency variability by high-pass filtering the daily calving flux time series with a 0.083 d^{-1} cutoff frequency (12 day period) to remove the longer-period signals from the record. The resulting high-frequency component is approximately normally distributed with a standard deviation of 5.4×10^5 m^3 d^{-1}, 20% of the mean calving flux over the period of our observations.

We compared this high-pass record to several environmental variables in an effort to gain additional insight into the patterns of iceberg calving. We explored daily rainfall, daily mean windspeed, and day-over-day mean temperature change, all recorded adjacent to the Yahtse Glacier terminus, as well as daily tidal range. These comparisons revealed a weak, negative relationship between rainfall and calving rate, however, the relationship weakens when the high-pass cutoff frequency is increased (for example to a 4 day cutoff period). None of the other environmental variables correlate with the high-pass calving flux. Day to day variations in calving appear to be random at Yahtse Glacier, although they may be connected to variations in ice flow speed if these are independent of, or lag, the environmental variables we have investigated.

4.6 Conclusions

Passive seismology is being increasingly applied in glaciology, particularly to the study of iceberg calving. However, previous attempts to tie calving seismicity to glacier dynamics have been stymied by an inability to quantitatively tie icequakes to iceberg volumes (*O'Neel et al.*, 2010; *Walter et al.*, 2012). These authors have noted the potential value in knowing this relationship. In this study, we have identified an empirical relationship between icequake properties and calving flux, and used it to derive an 18-month time series of calving fluxes. Our method reproduces a number of patterns previously identified, namely a mean calving flux in line with previous estimates as well as particularly rapid calving during the fall. It also reveals several patterns previously unknown, that evolve our understanding of iceberg calving, including a mid-winter minimum in iceberg calving and a strong calving response to semidiurnal tides. We observe interannual variability of calving fluxes of up to a factor of 2.

Our method began with the application and validation of an icequake locating algorithm to a several-hundred thousand event dataset that allowed us to focus our study on the icequakes generated by calving at Yahtse Glacier alone. After non-Yahtse calving icequakes were discarded, our final data set included 215,150 calving icequakes with sufficient amplitudes that we could be confident in our ability to detect them consistently throughout the year. In developing our generalized linear model for iceberg size, we explored the relationships between 13 different icequake properties and iceberg size. We found that duration (or its square root) is the single best predictor of iceberg size. Waveform amplitude-based metrics (MAX, RMS and ENR) provided some explanatory power.

Peak frequency and most icequake shape properties did not vary with iceberg size. Finally, we found a weak relationship between inter-event time and iceberg size.

Perhaps most critically, our study points to the tremendous utility of in-person observations of iceberg calving. Without our observer record, the link between icequakes and known calving events that serves as the foundation of our study could not have been made. We expect that the general features of our statistical model may well be universal–for example, our study lends more support to the previously identified relationship between icequake duration and iceberg size (*Qamar*, 1988; *O'Neel et al.*, 2007). However, the coefficients within our model (Table 4.1) may vary from site to site as the terminus-station distance and the iceberg calving style changes. Glaciers calving into deeper water, or with less pervasively fractured termini than Yahtse Glacier, could potentially have a different icequake signature. Furthermore, if the icequake occurrence rate/calving flux relationship (Fig. 4.11) persists at different sites, the need to develop more sophisticated statistical relationships between icequake properties and calving size may be obviated. Networks of relatively inexpensive short-period seismometers or geophones may be sufficient for the counting of icequakes and estimation of iceberg calving fluxes.

In this study, we have demonstrated how icequakes can be used to remotely, automatically track rates of iceberg calving at a single glacier. Provided that our method is tuned for a broad suite of glaciers, our hope and expectation is that pre-existing networks of seismometers can be used to track the temporal evolution of iceberg calving across entire mountain ranges and ice sheet margins. As we have found through application at Yahtse Glacier, such methods are likely to reveal an array of unanticipated patterns that will motivate continued improvement in our understanding of the rapidly changing dynamics of ocean-terminating glaciers.

4.7 Acknowledgments

This study was made possible by the National Science Foundation, through grant EAR-0810313. Additional funding is from USGS Climate and Land Use Change Program and Dept. of the Interior Climate Science Center. We gratefully acknowledge the dedication of our expert pilots, Tony Oney and Paul Claus, who significantly contributed to the success of this project. We acknowledge the loan of seismic equipment and field assistance from PASSCAL Polar Programs. UNAVCO provided geodetic instruments for our experiment. We thank David Conner and Jared Steyaert for their meticulous help with the calving ob-

server record. The Wrangell Mountains Center, McCarthy, AK, provided logistical assistance. Waveform figures and analyses were prepared with the GISMO (*Reyes and West*, 2011).

References

Amundson, J. M., M. Truffer, M. P. Lüthi, M. Fahnestock, M. West, and R. J. Motyka (2008), Glacier, fjord, and seismic response to recent large calving events, Jakobshavn Isbræ, Greenland, *Geophys. Res. Lett.*, *35*(22), 1–5, doi: 10.1029/2008GL035281.

Amundson, J. M., M. Fahnestock, M. Truffer, J. Brown, M. P. Lüthi, and R. J. Motyka (2010), Ice mélange dynamics and implications for terminus stability, Jakobshavn Isbræ, Greenland, *J. Geophys. Res.*, *115*(F1), 1–12, doi: 10.1029/2009JF001405.

Bartholomaus, T. C., C. F. Larsen, S. O'Neel, and M. E. West (2012), Calving seismicity from iceberg-sea surface interactions, *J. Geophys. Res.*, *117*(F4), 1–16, doi: 10.1029/2012JF002513.

Bartholomaus, T. C., C. F. Larsen, and S. O'Neel (2013), Does calving matter? Evidence for significant submarine melt, *Earth Planet. Sci. Lett.*, *380*, 21–30.

Battaglia, J., and K. Aki (2003), Location of seismic events and eruptive fissures on the Piton de la Fournaise volcano using seismic amplitudes, *J. Geophys. Res.*, *108*(B8), 1–14, doi: 10.1029/2002JB002193.

Burgess, E. W., R. R. Forster, and C. F. Larsen (2013), Flow velocities of Alaskan glaciers, *Nat. Commun.*, *4*(2146), 1–8, doi: 10.1038/ncomms3146.

Crawley, M. J. (2009), *The R Book*, 1st ed., 942 pp., John Wiley and Sons, West Sussex.

D'Alessandro, A., and N. A. Ruppert (2012), Evaluation of Location Performance and Magnitude of Completeness of the Alaska Regional Seismic Network by the SNES Method, *Bull. Seismol. Soc. Am.*, *102*(5), 2098–2115, doi: 10.1785/0120110199.

Ekström, G., M. Nettles, and G. A. Abers (2003), Glacial earthquakes, *Science*, *302*(5645), 622–4, doi: 10.1126/science.1088057.

Faillettaz, J., M. Funk, and D. Sornette (2011), Icequakes coupled with surface displacements for predicting glacier break-off, *J. Glaciol.*, *57*(203), 453–460, doi: 10.3189/002214311796905668.

Gutenberg, B., and C. F. Richter (1944), Frequency of earthquakes in California, *Bull. Seismol. Soc. Am.*, *34*(4), 185–188.

Jenkins, A. (2011), Convection-driven melting near the grounding lines of ice shelves and tidewater glaciers, *J. Phys. Oceanogr.*, *41*(12), 2279–2294.

Jones, G., B. Kulessa, S. Doyle, C. Dow, and A. Hubbard (2013), An automated approach to the location of icequakes using seismic waveform amplitudes, *Ann. Glaciol.*, *54*(64), 1–9, doi: 10.3189/2013AoG64A074.

Köhler, A., A. Chapuis, C. Nuth, J. Kohler, and C. Weidle (2012), Autonomous detection of calving-related seismicity at Kronebreen, Svalbard, *The Cryosphere*, *6*(2), 393–406, doi: 10.5194/tc-6-393-2012.

Krimmel, R. M., and B. H. Vaughn (1987), Columbia Glacier, Alaska: changes in velocity 1977âĂŞ1986, *J. Geophys. Res.*, *92*(B9), 8961–8968, doi: 10.1029/JB092iB09p08961.

McNabb, R. (2013), On the frontal ablation of Alaska tidewater glaciers, Ph.D. Dissertation, University of Alaska Fairbanks.

McNabb, R., et al. (2012), Using surface velocities to calculate ice thickness and bed topography: a case study at Columbia Glacier, Alaska, USA, *J. Glaciol.*, *58*(212), 1151–1164, doi: 10.3189/2012JoG11J249.

Miloh, T. (1991), On the initial-stage slamming of a rigid sphere in a vertical water entry, *Appl. Ocean Res.*, *13*(1), 43–48.

Montgomery, D. C., E. A. Peck, and G. G. Vining (2001), *Introduction to Linear Regression Analysis*, 3rd ed., 641 pp., John Wiley and Sons, New York.

Motyka, R. J., W. P. Dryer, J. Amundson, M. Truffer, and M. Fahnestock (2013), Rapid submarine melting driven by subglacial discharge, LeConte Glacier, Alaska, *Geophys. Res. Lett.*, *40*, 1–6.

O'Neel, S., K. A. Echelmeyer, and R. J. Motyka (2003), Short-term variations in calving of a tidewater glacier: LeConte Glacier, Alaska, U.S.A., *J. Glaciol.*, *49*(167), 587–598, doi: 10.3189/172756503781830430.

O'Neel, S., H. Marshall, D. McNamara, and W. T. Pfeffer (2007), Seismic detection and analysis of icequakes at Columbia Glacier, Alaska, *J. Geophys. Res.*, *112*(F3), 1–14, doi: 10.1029/2006JF000595.

O'Neel, S., C. F. Larsen, N. Rupert, and R. Hansen (2010), Iceberg calving as a primary source of regional-scale glacier-generated seismicity in the St. Elias Mountains, Alaska, *J. Geophys. Res.*, *115*(F4), 1–12, doi: 10.1029/2009JF001598.

Press, W. H., B. P. Flannery, S. A. Teukolsky, and W. T. Vetterling (1992), *Numerical Recipes in C. The Art of Scientific Computing*, 2nd ed., 994 pp., Cambridge Univ. Press, New York.

Qamar, A. (1988), Calving icebergs: a source of low-frequency seismic signals from Columbia Glacier, Alaska, *J. Geophys. Res.*, *93*(B6), 6615–6623.

Reyes, C. G., and M. E. West (2011), The Waveform Suite: A Robust Platform for Manipulating Waveforms in MATLAB, *Seismological Research Letters*, *82*(1), 104–110, doi: 10.1785/gssrl.

Richardson, J., G. Waite, K. FitzGerald, and W. Pennington (2010), Characteristics of seismic and acoustic signals produced by calving, Bering Glacier, Alaska, *Geophys. Res. Lett.*, *37*(L03503), 1–6, doi: 10.1029/2009GL041113.

Ritchie, J. B., C. S. Lingle, R. J. Motyka, and M. Truffer (2008), Seasonal fluctuations in the advance of a tidewater glacier and potential causes: Hubbard Glacier, Alaska, USA, *J. Glaciol.*, *54*(186), 401–411.

Schild, K. M., and G. S. Hamilton (2013), Seasonal variations of outlet glacier terminus position in Greenland, *J. Glaciol.*, *59*(216), 759–770, doi: 10.3189/2013JoG12J238.

Stein, S., and M. Wysession (2003), *An Introduction to Seismology, Earthquakes, and Earth Structure*, 498 pp., Blackwell Publishing, Malden, MA, USA.

Tsai, V., and G. Ekström (2007), Analysis of glacial earthquakes, *J. Geophys. Res.*, *112*(F3), 1–13, doi: 10.1029/2006JF000596.

Tsai, V., J. Rice, and M. Fahnestock (2008), Possible mechanisms for glacial earthquakes, *J. Geophys. Res.*, *113*(F03014), 1–17, doi: 10.1029/2007JF000944.

Veitch, S. A., and M. Nettles (2012), Spatial and temporal variations in Greenland glacial-earthquake activity, 1993 âĂŞ 2010, *J. Geophys. Res.*, *117*(October), 1–20, doi: 10.1029/2012JF002412.

Walter, F., J. M. Amundson, S. O'Neel, M. Truffer, M. Fahnestock, and H. a. Fricker (2012), Analysis of low-frequency seismic signals generated during a multiple-iceberg calving event at Jakobshavn Isbræ, Greenland, *J. Geophys. Res.*, *117*(F1), 1–11, doi: 10.1029/2011JF002132.

Warren, C. R., N. F. Glasser, S. Harrison, V. Winchester, A. R. Kerr, and A. Rivera (1995), Characteristics of tide-water calving at Glaciar San Rafael, Chile, *J. Glaciol.*, *41*(138), 273–289.

West, M., C. Larsen, M. Truffer, S. O'Neel, and L. LeBlanc (2010), Glacier microseismicity, *Geology*, *38*(4), 319–322, doi: 10.1130/G30606.1.

Wolf, L. W., and J. N. Davies (1986), Glacier-generated earthquakes from Prince William Sound, Alaska, *Bull. Seismol. Soc. Am.*, *76*(2), 367–379.

Xu, Y., E. Rignot, D. Menemenlis, and M. Koppes (2012), Numerical experiments on subaqueous melting of Greenland tidewater glaciers in response to ocean warming and enhanced subglacial discharge, *Ann. Glaciol.*, *53*(60), 229–234, doi: 10.3189/2012AoG60A139.

Zimmer, V. L., B. D. Collins, G. M. Stock, and N. Sitar (2012), Rock fall dynamics and deposition: an integrated analysis of the 2009 Ahwiyah Point rock fall, Yosemite National Park, USA, *Earth Surf. Process. Landforms*, *37*(6), 680–691, doi: 10.1002/esp.3206.

Appendix 4.A Additional figures

This appendix contains a number of figures pertinent to the time series of icequakes recorded at station BOOM and the influence of background noise on icequake detection.

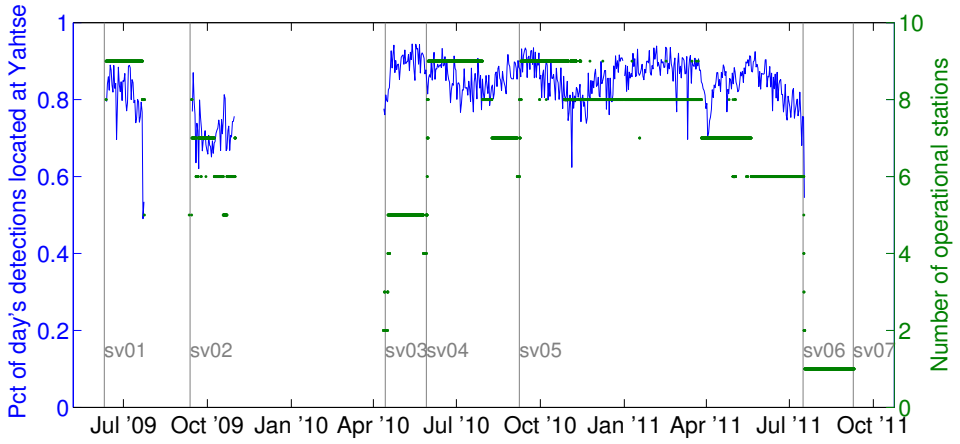

Figure 4.A.1. Proportion of icequakes located at the terminus of Yahtse Glacier and the number of operational stations. This plot serves as an assessment of location sensitivity to station outages. The times of 7 service runs are indicated.

The background noise level varies seasonally (Fig. 4.A.2), and increases rapidly during the beginning of July, plateaus through August, then falls off towards background levels through September and October. Noise levels are very low from November through to June. This pattern is very similar to the annual pattern of subglacial discharge.

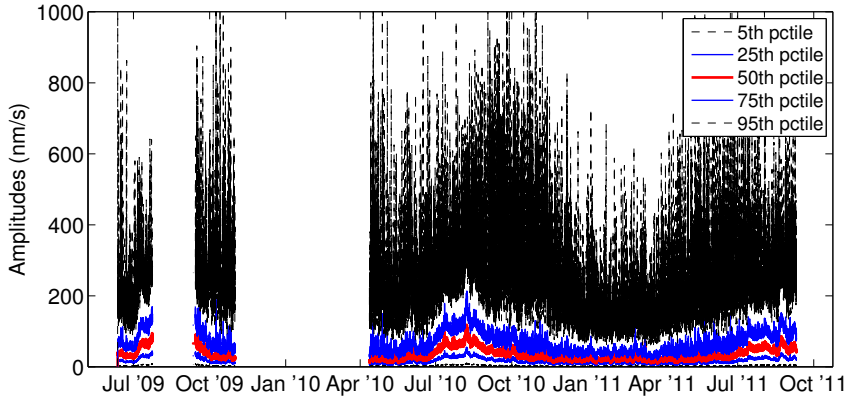

Figure 4.A.2. Noise levels recorded at BOOM at five different percentile levels. Waveform was recorded on the vertical channel of BOOM, filtered between 1 and 5 Hz. Percentile amplitudes are calculated from 1-hr, non-overlapping, portions of the absolute value of the waveform. Thus, the higher percentiles (such as the 95th) include individual seismic events, such as icequakes. Lower percentiles represent background noise levels. In other plots, we define noise to be the median (50th percentile) amplitude.

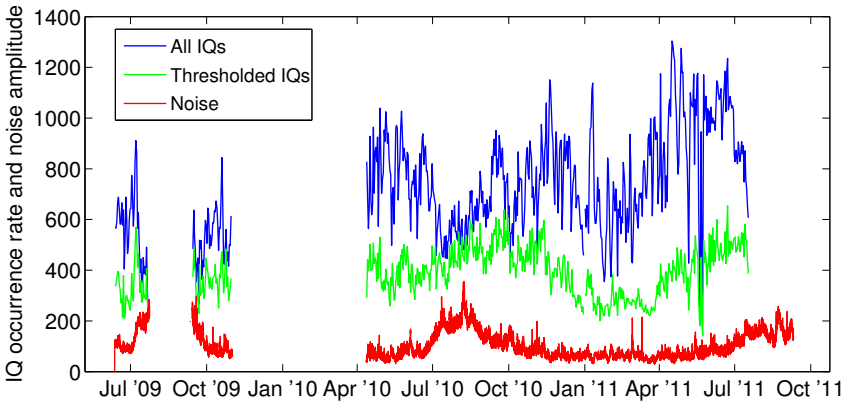

Figure 4.A.3. Impact of seismic noise on icequake detection rate. Background noise level (in nm/s $\times 3$) is compared with two daily icequake occurrence rates: all Yahtse calving icequakes, and just those icequakes whose maximum amplitude exceeds some threshold. We take the maximum amplitude (MAX) threshold to be 900 nm/s, selected as the "amplitude of completeness." The complete icequake occurrence rate (All IQs, in blue) seems to be affected by the noise level. Detections decrease when the noise increases. The thresholded icequake occurrence rate does not appear to be affected by the noise level. Thus, we proceed with the thresholded icequakes for the analyses and all other figures of this paper.

Appendix 4.B Model performance

This appendix includes a number of figures that demonstrate the quality of the preferred model (Table 4.1).

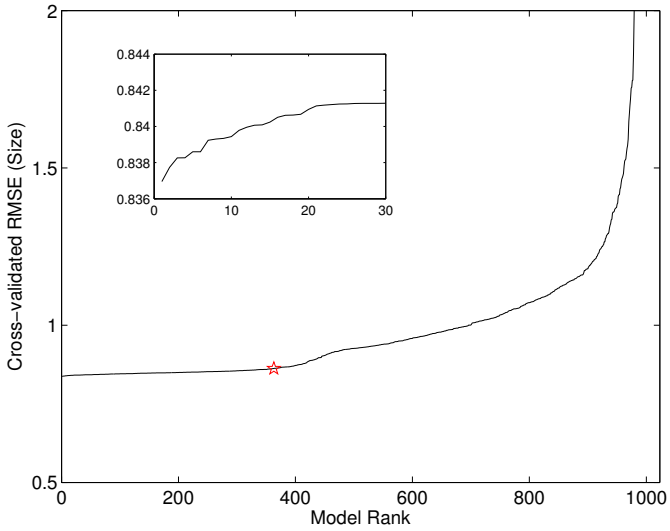

Figure 4.B.1. The cross-validated RMSE of all 1023 evaluated models. The red star represents the rank and cross-validated RMSE of the preferred model (Table 4.1).

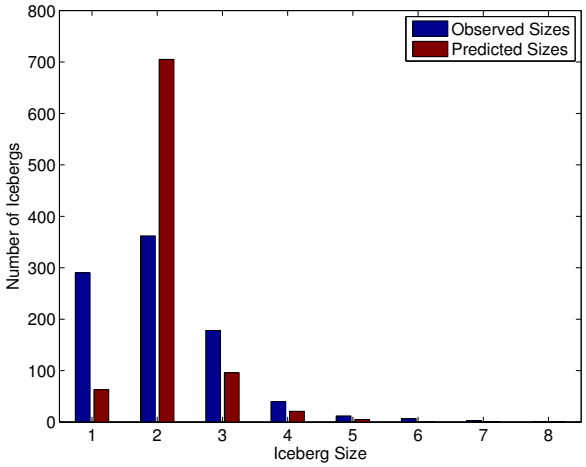

Figure 4.B.2. Size distributions of observed and predicted icebergs for the 892 training icequakes/icebergs. Predicted sizes are those predicted by the preferred model rounded to the nearest integer, in order to make them directly comparable with the integer values of the observed sizes.

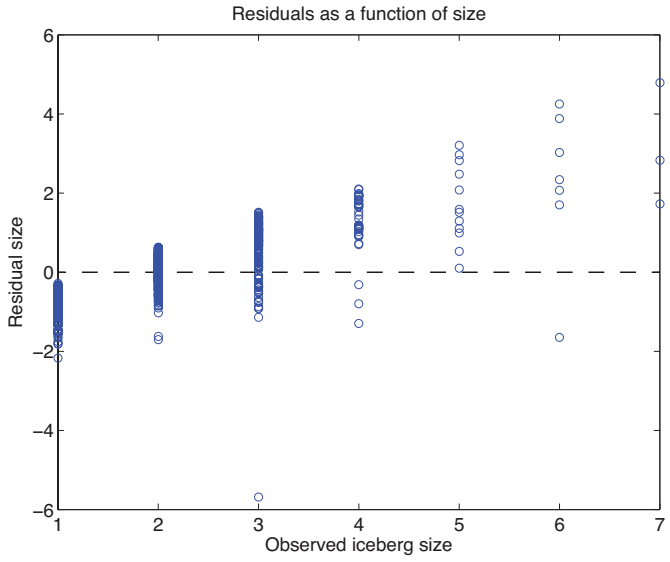

Figure 4.B.3. Model residuals as a function of observed iceberg size. Residuals are the observed size minus the predicted size.

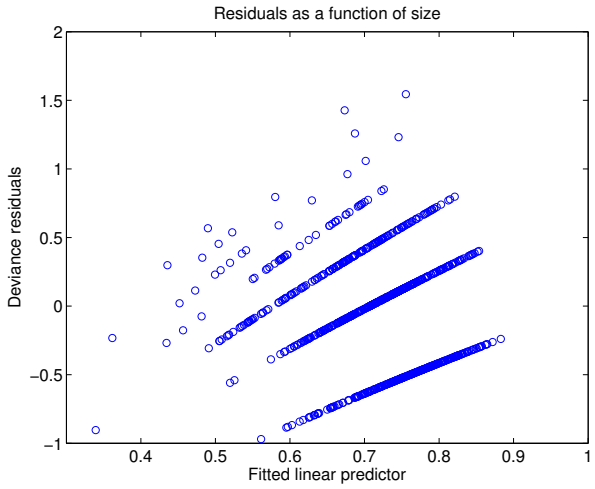

Figure 4.B.4. Model residuals as a function of linear predictor. The linear predictor in the fitted generalized linear model is the right-hand-side of the equation in Table 4.1: the linear sum of the the regressors with their coefficients. Due to the different error structure of generalized linear models, the linear predictor is more useful for evaluating model performance than the fitted response variable. Deviance residuals are a standardized form of residuals appropriate for generalized linear models. This plot is evaluate in much the same way that similar plots are evaluated for general linear models: good models have no trend in the mean or variance of the residuals.

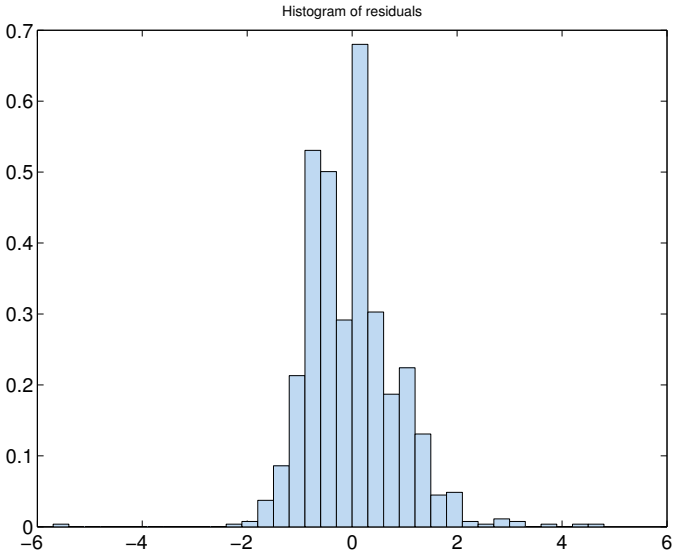

Figure 4.B.5. Histogram of model residuals.

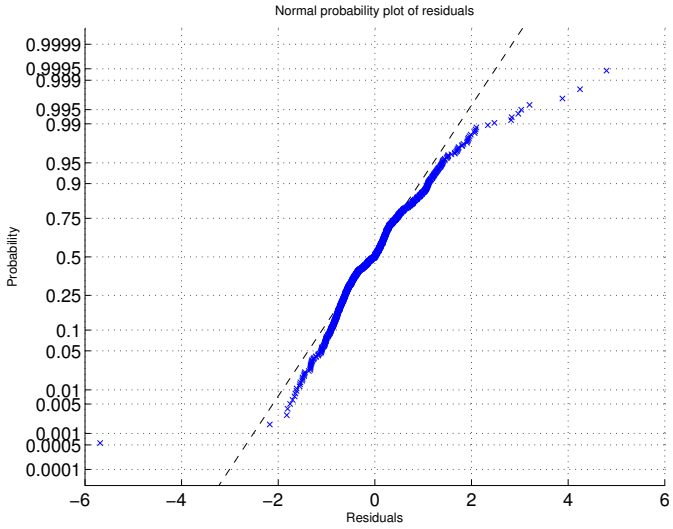

Figure 4.B.6. Probability plot of model residuals.

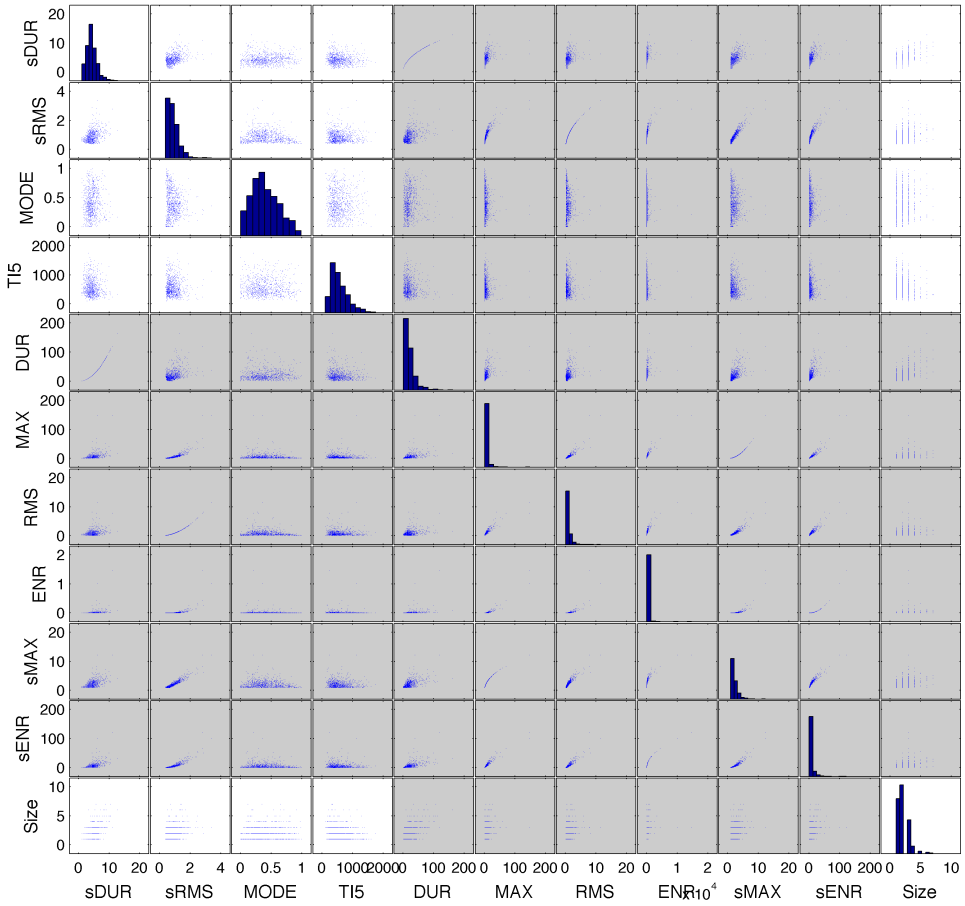

Figure 4.B.7. Correlation diagram of regressors included in the model evaluation. Off-diagonal panels are scatter plots showing the relationships between each pair of variables. Panels along the diagonal are histograms showing the structure of values for each variable. Lower-case 's' in front of a regressor indicates a square root. White background plots are for regressors included in the preferred model. Gray shaded plots are excluded from the model. "Size" is the response variable, iceberg size. Each regressor included in the preferred model has a variance inflation factor < 5.

Chapter 5
Conclusions

Icebergs calve off of the terminus at Yahtse Glacier nearly every minute. Each significant calving event produces an icequake that is recordable at the glacier terminus and sometimes hundreds of kilometers from the calving front. However, the amplitude of those icequakes, and therefore their detectability at distance, is not a clearly definable function of the volume of calved ice. We have found that most of the seismic energy present within an icequake is produced after the iceberg has fully detached from the terminus cliff. Strong seismic energy is produced first as the iceberg enters the water, and then more powerfully if the iceberg descends fully beneath the water surface. If the momentum of falling icebergs is sufficient to carry them beneath the surface of the fjord, the descending icebergs will generate air cavities in their lee. When the seawater rushes in to slam those cavities closed, they generate Worthington jets powerful enough to launch water and ice debris to heights greater than the glacier terminus. This cavitation generates abrupt, large-amplitude peaks in ground motion. Our finding contrasts with previous studies of calving icequakes that suggested either basal slip or vibrating water-filled cracks may be the seismogenic sources (*Wolf and Davies*, 1986; *O'Neel and Pfeffer*, 2007). We conclude that *how* icebergs calve may be as important for the generation of seismicity as the size of the iceberg that breaks off of the terminus.

At some glaciers, nearly equal proportions of icebergs detach from the glacier terminus above and below sea level (i.e., subaerial and submarine calving; *Motyka*, 1997; *O'Neel et al.*, 2003, 2007). On trips to the advancing terminus of Yahtse Glacier during months between April and October, we rarely saw submarine iceberg calving. Careful, focused observation and documentation of iceberg calving events bore out this qualitative observation. Thus, inspired in part by earlier observations at LeConte Glacier (*Motyka et al.*, 2003), we investigated the possibility of submarine melt of the glacier terminus. Icy Bay hydrography revealed that water even within 2 km of the Yahtse Glacier terminus was efficiently connected with the Alaska Coastal Current. During July 2010, when especially warm water was present along the Gulf of Alaska coast, water at the head of the Yahtse fjord reached 10.4 °C. In an abnormally cool July 2011, we found that water up to 7 °C was associated with an 18 m deep layer of glacially-modified water that contained 1-2% melted ice from the front of Yahtse Glacier. When we estimated the mean current within that shallow, glacially-modified water, we found that the submarine portion of the glacier

terminus was melting at over 9 m d^{-1}, and could easily balance the speed with which ice was flowing towards the glacier terminus. The calving of millions of cubic meters of icebergs each day is likely paced by the rate at which their submarine support is melted out from beneath them. Submarine melt may be far more important for iceberg calving than longitudinal strain rates or the tensile strength of ice (cf. *Nick et al.*, 2010).

The lower half of Yahtse Glacier's terminus, that part below sea level, may melt and drift away without any seismically detectable sign. However, we have shown that variations in the rate of iceberg calving can be used as a proxy for variations in the rate of frontal ablation. In the final chapter of this dissertation, we catalogued all of the calving icequakes produced at Yahtse Glacier over 18 months of observations. To generate a time series of calving fluxes from this icequake catalog, we developed a statistical model that can predict an iceberg's volume by the properties of its icequake. We find that icequake duration has a significant relationship with iceberg volume. The calving fluxes we derive are far from steady. Calving flux varies from year to year, is higher during the summer and fall than it is during the winter, and is sensitive to the raise and fall of ocean tides. While our oceanographic results were focused on data from the summer only, our study of calving icequakes spans the seasons. The results of this study remain consistent with our view that the ocean plays a major role in controlling the rates of frontal ablation at Yahtse Glacier.

In our introduction, we posed a number of questions that we are now equipped to answer:

- What part or parts of the iceberg calving process (e.g., vibrating serac blocks, ice fracturing, iceberg impact on the water) generate the iceberg calving signals detected over 100s of km from the glacier front?

  The largest amplitude seismic signals are generated by icebergs that fall from substantial heights above the sea surface and create air cavities within the seawater. These signals are likely to be detected over the greatest distances. Additional seismicity is associated with the impact of the iceberg on the water. These two sources, cavitation and slamming, demonstrate that significant seismic energy can travel through the water before coupling to land and being recorded at a terrestrial seismometer. A third seismogenic process is ice fracture, which is recorded as lower amplitude seismic waves at higher frequencies.

- What information about a particular calving event is contained within the icequake signal it produces?

  The clearest association between a calving event and its icequake is that the durations tend to be comparable. Calving events that evolve over long timespans are generating seismic energy over those same time spans. The relationship between icequake amplitude and iceberg size is much weaker. Strong peaks in seismic waveforms may be caused by icebergs that fall from high on the terminus, regardless of the size of the iceberg. More complicated icequakes, with multiple peaks and a waveform envelope that expands and contracts in amplitude are likely to be generated by multi-part, complicated calving events.

- Can we predict the mass or volume of an iceberg by examining its icequakes?

  Yes. These predictions have substantial uncertainty and absolute volume estimates are imprecise. However, relative volumes are substantially better and icebergs that are predicted to be large are typically truly larger than those icebergs that are predicted to be smaller. When examining our results, some large icebergs are misidentified as small icebergs. But if an iceberg is predicted to be large, then it is almost certainly quite large. The duration of the icequake is the most valuable tool for identifying the size of the iceberg.

- What role does the ocean play in iceberg calving?

  The ocean plays a central role in controlling the rate of iceberg calving. We have found that submarine melt may be so rapid that calving occurs simply in response to the melting of the base on which subaerial seracs stand. Subglacial discharge is responsible for drawing in and mixing warm ocean water against the glacier terminus. When the ocean cools and subglacial discharge decreases in the winter, the rate of calving decreases and the terminus advances.

- How much of the ice that reaches the terminus melts vs. breaks off and floats away as icebergs?

  We estimate that between 3 and 5 $\times 10^6$ m^3 of ice reaches the terminus each day[1]. From July through October, all of the ice that comes into contact with the sea at the

[1] 2700 m wide $\times$ 115 m average thickness $\times$ an average velocity equal to the centerline surface velocity, 17 m d^{-1}, or a mid-range portion of that maximum velocity, 10 m d $^{-1}$. See also *Bartholomaus et al.* (2013).

glacier terminus has the potential to melt and drift away, approximately 2/3 of the total frontal ablation. The remaining third, above sea level, must calve. In February and March, the submarine melt rate is likely substantially less, and nearly all of the frontal ablation might be due to calving. We are unable, with the information at hand, to derive an annually-averaged proportion.

- To what extent is water from the Gulf of Alaska exchanged with the water at the distal, glacierized heads of fjords?

  The water within Icy Bay appears to be efficiently connected with the Alaska Coastal Current, along the Gulf of Alaska coast. Water properties within the Alaska Coastal Current go through a number of step changes during the spring and summer. In 2010, the water temperature of the Alaska Coastal Current stepped from 9 to 11 °C 18 days prior to our measurements for that year, making the coastal water > 1 °C warmer than it was during either 2009 or 2011. Our CTD casts from near the head of Icy Bay appear to reflect these changes.

- Do tidal variations in sea level affect rates of iceberg calving?

  Yes. Iceberg calving at Yahtse Glacier is sensitive to variations in tidal stage at semidiurnal, fortnightly and monthly periods. Even small perturbations to the stresses at the front of Yahtse Glacier modulate the flux of ice falling from the terminus of Yahtse Glacier. The response to small stress perturbations suggests that the seracs at glacier terminus are fragile.

5.1 Opportunities for future research

The results of this dissertation point the way towards several new questions and research frontiers.

With respect to the generation of calving icequakes (Chapter 2):

Yahtse Glacier is a temperate glacier with a thin terminus advancing into shallow water. To what extent do different terminus geometries effect the generation of calving icequakes? The icequakes observed at Yahtse Glacier share a number of features with those produced by other glaciers across Alaska, including their durations, frequency content, amplitudes, and emergent onsets. Thus we expect that all glaciers across Alaska may share a common

source. However, focused studies of smaller icequakes, of the kind that we have documented here, are absent from the ice sheets. Small, subaerial drop-style calving events (*Bartholomaus et al.*, 2012) have been observed at Rink Isbræ, a major outlet of the Greenland Ice Sheet. How similar are its icequakes to those at Yahtse? A seismometer we installed at its terminus in August 2013 offers us an opportunity to answer this question.

Amundson et al. (2010) described a number of icequakes recorded near Jakobshavn Isbræ that are similar in appearance to those identified at Yahtse Glacier. Their icequakes originated both from the fjord, and from the terminus. Are these events potentially generated by the same mechanisms that we have proposed here?

Can focal mechanisms be obtained for the icequakes observed at Yahtse Glacier? If so, are they consistent with an implosion source as we expect given the importance of cavitation in icequake seismogenesis (rather than a single force or double couple)? Do different parts of Yahtse Glacier's icequakes match different types of sources better or worse? For example, we might expect the early part of some waveforms, generated by iceberg impact, to fit a single force source. Later in the icequake, an implosion source might work better.

To what extent do path effects or geologic structure alter the appearance of the icequakes as they move through the network? The earth structure is exceedingly complex in the area surrounding Yahtse Glacier, as it is in many mountainous regions. The vertical relief over short distances is large and the impedance contrasts between low-density sedimentary rock, glaciomarine seafloor mud, ice, and water are large, potentially leading to complex reflections and trapped waves. What is the effect of this structure on icequake waveforms?

Does a more sophisticated hydrodynamic model of iceberg impact result in a view of iceberg impact forces that are substantially different than those that we find?

With respect to submarine melt (Chapter 3):

How important is the presence of a putative submarine terminal moraine at the terminus of Yahtse Glacier in controlling submarine melt rates? The submarine shoals at the former termini of tidewater glaciers in Alaska frequently rise to within 10-20 m of the sea surface (*Muench and Heggie*, 1978). Does the submarine moraine at the front of Yahtse Glacier, pushed forward by the advancing terminus, approach these shallow depths or is it restricted to depths greater than 100 m as we have argued in several places within this

dissertation (*Bartholomaus et al.*, 2013)? How does the presence or absence of a submarine moraine alter seawater circulation within a proglacial fjord?

We have proposed a general time series of submarine melt rates for Gulf of Alaska tidewater glaciers (Fig. 3.7). Do observations over multiple seasons bear out our conjecture? Surface mass balance is linked to submarine melt by the control if exerts on meltwater runoff/subglacial discharge (*Bartholomaus et al.*, 2013; *Motyka et al.*, 2013). How important is this link to submarine melt?

We observed that water from the Gulf of Alaska is present near the terminus of Yahtse Glacier, but are unable to identify the process or processes that control the rate of water exchange between Icy Bay and the Gulf of Alaska. Is estuarine exchange steady in these glacierized fjords, or episodic? What controls the rate of exchange?

What effect does Yahtse Glacier's advancing status have on submarine melt? Yahtse Glacier presently goes through 200-300 m seasonal swings in terminus position. If it advances over its submarine terminal moraine, what effect does this have on the submarine melt rate?

With respect to estimating calving flux with icequake properties (Chapter 4):

How universal, or different, are models of calving flux developed for different glaciers and among different glacierized regions? To what extent can we apply the model we have developed at Yahtse Glacier to calving at Columbia Glacier, or in Greenland?

What controls the size distribution of icebergs calved from different glaciers? We have suggested that the icebergs calved at Yahtse are smaller than the icebergs calved at other glaciers because Yahtse is grounded in shallow water, and is particularly sensitive to perturbations to its terminus normal stress? Can we test this? Do other glaciers grounded in shallow water calve relatively smaller, more frequent icebergs?

Can we use regional seismic networks to identify time series of iceberg calving across a mountain range? Is the Alaska Earthquake Information Center's existing network sufficient for this purpose? And after the NSF Earthscope Transportable Array is installed?

Do annual and sub-annual variations in iceberg calving differ between advancing glaciers and retreating glaciers?

I believe that the results of this dissertation have improved our understanding of iceberg calving: how and why it occurs, and the tools that we can employ to study it. My hope is that future efforts to understand processes at the terminus of tidewater glaciers

will be able to build on the results of this dissertation to address some of the questions outlined above.

References

Amundson, J. M., M. Fahnestock, M. Truffer, J. Brown, M. P. Lüthi, and R. J. Motyka (2010), Ice mélange dynamics and implications for terminus stability, Jakobshavn Isbræ, Greenland, *J. Geophys. Res.*, *115*(F1), 1–12, doi: 10.1029/2009JF001405.

Bartholomaus, T. C., C. F. Larsen, S. O'Neel, and M. E. West (2012), Calving seismicity from iceberg-sea surface interactions, *J. Geophys. Res.*, *117*(F4), 1–16, doi: 10.1029/2012JF002513.

Bartholomaus, T. C., C. F. Larsen, and S. O'Neel (2013), Does calving matter? Evidence for significant submarine melt, *Earth Planet. Sci. Lett.*, *380*, 21–30.

Motyka, R. J. (1997), Deep-water calving at LeConte Glacier, southeast Alaska, *Byrd Polar Res. Center Rep.*, *15*, 115–118.

Motyka, R. J., L. Hunter, K. A. Echelmeyer, and C. Connor (2003), Submarine melting at the terminus of a temperate tidewater glacier, LeConte Glacier, Alaska, U.S.A., *Ann. Glaciol.*, *36*(1), 57–65, doi: 10.3189/172756403781816374.

Motyka, R. J., W. P. Dryer, J. Amundson, M. Truffer, and M. Fahnestock (2013), Rapid submarine melting driven by subglacial discharge, LeConte Glacier, Alaska, *Geophys. Res. Lett.*, *40*, 1–6.

Muench, R. D., and D. T. Heggie (1978), Deep water exchange in Alaskan subarctic fjords, in *Estuarine Transport Processes*, edited by B. Kjerfve, pp. 239–267, University of South Carolina Press, Columbia, South Carolina.

Nick, F. M., C. J. van der Veen, A. Vieli, and D. I. Benn (2010), A physically based calving model applied to marine outlet glaciers and implications for the glacier dynamics, *J. Glaciol.*, *56*(199), 781–794.

O'Neel, S., and W. T. Pfeffer (2007), Source mechanics for monochromatic icequakes produced during iceberg calving at Columbia Glacier, AK, *Geophys. Res. Lett.*, *34*(22), 1–5, doi: 10.1029/2007GL031370.

O'Neel, S., K. A. Echelmeyer, and R. J. Motyka (2003), Short-term variations in calving of a tidewater glacier: LeConte Glacier, Alaska, U.S.A., *J. Glaciol.*, *49*(167), 587–598, doi: 10.3189/172756503781830430.

O'Neel, S., H. Marshall, D. McNamara, and W. T. Pfeffer (2007), Seismic detection and analysis of icequakes at Columbia Glacier, Alaska, *J. Geophys. Res.*, *112*(F3), 1–14, doi: 10.1029/2006JF000595.

Wolf, L. W., and J. N. Davies (1986), Glacier-generated earthquakes from Prince William Sound, Alaska, *Bull. Seismol. Soc. Am.*, *76*(2), 367–379.